MODELING, EVALUATION, AND ASYMPTOTIC ANALYSIS OF ATTENUATION ANISOTROPY

by

Bharath Chandra Shekar

A thesis submitted to the Faculty and the Board of Trustees of the Colorado School of Mines in partial fulfillment of the requirements for the degree of Doctor of Philosophy (Geophysics).

Golden, Colorado

Date _____

Signed: _____
Bharath Chandra Shekar

Approved: _____
Dr. Ilya Tsvankin
Thesis Advisor

Golden, Colorado

Date _____

_____
Dr. Terence K. Young
Professor and Head
Department of Geophysics

ABSTRACT

Seismic attenuation is sensitive to the physical properties of the subsurface, which makes attenuation analysis a useful tool for reservoir characterization. In this thesis, I present algorithms for estimating directionally dependent attenuation coefficients and perform asymptotic and numerical analysis of wave propagation in attenuative anisotropic media.

First, I introduce a methodology to estimate the S-wave interval attenuation coefficient by extending the layer-stripping method of Behura and Tsvankin (2009) to mode-converted (PS) waves. Kinematic reconstruction of pure shear (SS) events in the target layer and the overburden is performed by combining velocity-independent layer stripping with the PP+PS=SS method. Then, application of the spectral-ratio method and the dynamic version of velocity-independent layer stripping to the constructed SS reflections yields the S-wave interval attenuation coefficient in the target layer. The attenuation coefficient estimated for a range of source-receiver offsets can be inverted for the interval attenuation-anisotropy parameters. The method is tested on synthetic data generated with the anisotropic reflectivity method for layered VTI (transversely isotropic with a vertical symmetry axis) media and vertical symmetry planes of orthorhombic media.

Then, I analyze a cross-hole data set generated by perforation shots set off in a horizontal borehole to induce hydraulic fracturing in a tight gas reservoir. The spectral-ratio method is applied to pairs of traces to set up a system of equations for directionally-dependent effective attenuation. Although the inversion provides clear evidence of attenuation anisotropy, the narrow range of propagation directions impairs the accuracy of anisotropy analysis. The observed variations of the attenuation coefficient between different perforation stages appear to be related to changes in the medium due to hydraulic fracturing and stimulation.

Important insights into point-source radiation in attenuative anisotropic media can be gained by applying asymptotic methods. I derive the asymptotic Green's function in homo-

geneous, attenuative, arbitrarily anisotropic media using the steepest-descent method. The saddle-point condition helps describe the behavior of the far field slowness and group-velocity vectors and evaluate the inhomogeneity angle (the angle between the real and imaginary parts of the slowness vector). The results from the asymptotic analysis are compared with those from the ray-perturbation method for P-waves in TI media.

Finally, I address the problem of efficient viscoelastic modeling in heterogeneous anisotropic media. The Kirchhoff scattering integral is employed to generate reflected P-waves, with the required Green's functions computed by summation of Gaussian beams. The influence of attenuation on the Gaussian beams is incorporated using ray-perturbation theory. The method is applied to generate synthetic data from a highly attenuative VTI medium above a horizontal reflector and a structurally complex acoustic model with a salt body.

To my parents, Smt. Chandrika and Shri. Chandrashekar.

TABLE OF CONTENTS

LIST OF FIGURES

LIST OF TABLES

ACKNOWLEDGMENTS

My years at the Colorado School of Mines have been a very satisfying personal and intellectual experience. The interaction with the leaders and peers at the Center for Wave Phenomena has been invaluable. Ilya Tsvankin has been an excellent advisor. I am very grateful for his patience and confidence in me. The notes from his seismology classes are something that I will always use as a reference. Roel Snieder and Mike Batzle gave me excellent and constant feedback on my research. I am very lucky to have attended classes by Paul Martin and Luis Tenorio. They made Mathematics fun and thanks to them, I no longer fear the subject. Ivan Psencik has been patient to answer my nagging queries.

As a new graduate student in a group with excellent scientists, I was a bundle of nerves. Special thanks should go to Barbara and Diane for their orientation sessions and for listening to my often irrational rants. Diane and Ilya have been a great resource for polishing my writing. Thanks also to Michelle and Pam for all their help.

Mathias and Clement have been great friends and partners in crime. Steve, Jyoti, and Sribharath always found time to help me with my research. The outdoor lunch conversations with Shingo were fun. Nishant, Filippo, and Franceso were wonderful room mates and it was an enriching experience to live in the "geophysics/party house." Danilo, Mariana, and Julio hosted me in Brazil where I had a great adventure. Thank you Sarah D'Adamo and Francesca for conferring me a honorary Italian citizenship. Thanks to Sarah Khalid for the "Desi nights" and the beautiful painting you gave me. I had a great time in Houston with Dip and Paritosh. Katoch has always been a great friend and guide.

I will always fondly remember my years in Golden as a PhD student. I have been fortunate to make great friends and learn from great teachers. The mountains and valleys of Colorado have given me much joy, filled me with awe and inspired me over the last five years. I will have a special place in my heart for Golden.

Chapter 1

INTRODUCTION

Seismic amplitude can provide high-resolution information about the subsurface and has the potential to constrain important physical parameters. Attenuation in general and the angular variation of attenuation coefficients (attenuation anisotropy) represent a critical component in understanding the amplitude and dispersion of seismic waves.

The primary application of attenuation measurements is in reservoir characterization (Lynn, 2004). Accounting for attenuation is also important in imaging the subsurface using depth migration (Cavalca et al., 2013), performing robust amplitude-variation-with-offset (AVO) analysis (Behura and Tsvankin, 2009b), and minimizing data misfit in waveform tomography (Pratt et al., 2004). Measurements of P- and S-wave attenuation and attenuation anisotropy have been used to evaluate lithology and the properties of fluids (Das and Batzle, 2010; Chichinina et al., 2009), characterize fractures (Liu et al., 2007), identify "sweet" spots in porous gas reservoirs (Behura et al., 2012), and perform time-lapse monitoring (Blanchard et al., 2010; Hofmann, 2006). A detailed review of the literature on the application of attenuation measurements to reservoir characterization can be found in chapters 2 and 3.

Attenuation estimation from reflection seismic data is a challenging problem because the amplitudes of seismic waves are also determined by the source characteristics and a variety of propagation phenomena including reflection, transmission, geometrical spreading, caustics, scattering by heterogeneities, etc. In surface seismic surveys, the source and receiver coupling and near-surface effects can further distort the amplitudes. Such techniques as the spectral-ratio method (Johnston and Toksöz, 1981), peak instantaneous frequency method (Matheney and Nowack, 1995), and centroid frequency shift method (Quan and Harris, 1997a) have been employed to estimate P-wave attenuation from reflection seismic and VSP (vertical seismic profiling) data (Dasios et al., 2001; Maultzsch et al., 2007; Behura and Tsvankin, 2009a).

Chapters 2 and 3 review the literature on attenuation estimation in greater detail.

Analysis of point-source radiation in homogeneous attenuative anisotropic media can provide valuable insights into wave propagation and potentially improve AVO inversion. Whereas radiation from point sources in purely elastic anisotropic media has been extensively studied in the literature using both asymptotic and numerical techniques (Červený, 2001; Tsvankin, 2012), few papers have examined this problem for attenuative media (Vavryčuk, 2007; Zhu, 2006). Chapter 4 reviews the existing results on point-source radiation in elastic and attenuative media.

Efficient and accurate modeling of wave propagation in attenuative anisotropic media is crucial in generating synthetic seismograms for realistic subsurface models. The reflectivity method is a semi-analytic technique to compute exact synthetic seismograms from horizontally layered media (Schmidt and Tango, 1986). Models with lateral variations in material properties and curved interfaces can be handled using ray-based methods (Červený, 1985), finite-difference techniques that operate in the frequency (Kamei and Pratt, 2013) or time domain (Hestholm, 2002), pseudospectral methods (Carcione, 2011), etc. Publications on seismic modeling in attenuative media are reviewed in chapter 5.

In this thesis, I develop algorithms for estimating anisotropic attenuation coefficients and present asymptotic and numerical methods for analyzing and modeling wave propagation in attenuative anisotropic media.

In Chapter 2, I extend the attenuation layer-stripping method of Behura and Tsvankin (2009a) to mode-converted PS data in order to estimate interval shear-wave attenuation. Pure shear reflection events are first constructed in a kinematic sense in both the overburden and target layer using the PP+PS=SS method. I then combine the modified spectral-ratio method with the dynamic version of velocity-independent layer stripping (VILS) to compute the interval shear-wave attenuation in the target horizon. The algorithm is tested on multicomponent synthetic data generated with the reflectivity method for layered VTI media and symmetry planes of orthorhombic media.

Chapter 3 presents the results of a case study of cross-hole data generated by perfo-

ration shots set off in a horizontal borehole to induce hydraulic fracturing in a tight-gas reservoir. I introduce a methodology to measure attenuation anisotropy from data acquired in a vertical monitoring borehole over a narrow range of propagation angles. The attenuation coefficient varies systematically between different perforation stages, which may be related to the diffusion of stimulant fluids in the induced fractures.

The asymptotic Green's function in homogeneous, attenuative, arbitrarily anisotropic media is derived in Chapter 4. The saddle-point condition yields the plane wave that makes the most significant contribution to wavefield, which helps evaluate the inhomogeneity angle and complex-valued group-velocity vector. P-wave signatures obtained from the asymptotic analysis for TI media are compared with the same quantities computed by ray-perturbation theory.

In Chapter 5, I present a ray-based 2.5D modeling algorithm to generate reflection seismic data from heterogenous, attenuative, anisotropic media. The Kirchhoff scattering integral is employed to compute P-wave reflections with the relevant Green's functions obtained from Gaussian beam summation. The contribution of attenuation to the Green's function is included using perturbation ray theory. The algorithm is tested on layered elastic TI media and on a structurally complicated acoustic model containing a salt body.

Chapter 2

ESTIMATION OF SHEAR-WAVE INTERVAL ATTENUATION FROM MODE-CONVERTED DATA

Interval attenuation measurements provide valuable information for reservoir characterization and lithology discrimination. Here, we extend the attenuation layer-stripping method of Behura and Tsvankin to mode-converted (PS) waves with the goal of estimating the interval S-wave attenuation coefficient. By identifying PP and PS events with shared ray segments and applying the PP+PS=SS method, we first perform kinematic construction of pure shear (SS) events in the target layer and overburden. Then, the modified spectral-ratio method is used to compute the effective shear-wave attenuation coefficient for the target reflection. Finally, application of the dynamic version of velocity-independent layer stripping to the constructed SS reflections yields the interval S-wave attenuation coefficient in the target layer. The attenuation coefficient estimated for a range of source-receiver offsets can be inverted for the interval attenuation parameters. The method is tested on multicomponent synthetic data generated with the anisotropic reflectivity method for layered VTI and orthorhombic media.

2.1 Introduction

Attenuation analysis provides seismic attributes sensitive to the physical properties of the subsurface. Reliable attenuation measurements have become feasible with acquisition of high-quality reflection and borehole data. Attenuation is often found to be anisotropic (directionally dependent) due to a variety of factors such as the intrinsic anisotropy of the material (Prasad and Nur, 2003), the presence of aligned fluid-fractures (Batzle et al., 2005; Chapman, 2003), or interbedding of thin layers with different properties (Carcione, 1992;

Zhu et al., 2007b). The magnitude of attenuation anisotropy can be much higher than that of velocity anisotropy, and the symmetry of the attenuation coefficient can be different than that of the velocity function (Liu et al., 2007; Zhu et al., 2007b).

The quality factors Q_P and Q_S are widely used as measures of P- and S-wave intrinsic attenuation, respectively. Klimentos (1995) measures compressional and shear attenuation from sonic logs in sandstone formations with variable oil, water and gas saturation and observes that Q_P and Q_S can be used for pore-fluid discrimination. According to the results of Adam et al. (2009), the substitution of light hydrocarbons with brine in carbonate rocks leads to a large increase in P-wave attenuation. Chichinina et al. (2009) conduct ultrasonic laboratory experiments for models with VTI symmetry. Their results show that the symmetry-axis attenuation of P-waves is much greater than that of S-waves in dry samples, while for oil-saturated samples the two modes have comparable attenuation. Blanchard et al. (2010) correlate the time-lapse changes in P-wave attenuation measured over a carbon-sequestration site to the changes in CO_2 concentration. Shear-wave attenuation in heavy oils is closely linked to temperature, and hence could be useful in seismic monitoring of thermal recovery processes (Behura et al., 2007). Attenuation due to the presence of gas in the near-surface layers causes distortions in the amplitudes of migrated events, which necessitates application of offset-dependent attenuation correction (Xin et al., 2008).

De et al. (1994) report measurements of the S-wave quality factor from vertical seismic profiling (VSP) surveys and sonic logs. Shear-wave attenuation is more difficult to evaluate from reflection data due to such problems as a low signal-to-noise ratio and statics errors. Behura and Tsvankin (2009a) combine the velocity-independent layer stripping (VILS) method of Dewangan and Tsvankin (2006) with the spectral-ratio method (Johnston and Toksöz, 1981) to estimate the interval attenuation of pure PP or SS reflected waves. Their method assumes the overburden layers to be laterally homogeneous with a horizontal symmetry plane, while the target layer can be arbitrarily anisotropic and heterogeneous. They identify the overburden and target events that share ray segments in the overburden to compute the interval traveltime and then the interval attenuation coefficient in the target. The algorithm

of Behura and Tsvankin (2009a) is data-driven, and does not require information about the velocity or attenuation in the overburden. Reine et al. (2009a) introduce a similar algorithm for evaluating the interval P-wave attenuation. Their method operates in the $\tau - p$ domain and, therefore, it is limited to laterally homogeneous target layers.

Shear waves, however, cannot be excited offshore, and shear-wave sources are seldom used on land. Therefore, here we extend the technique of Behura and Tsvankin (2009a) to mode-converted data by supplementing it with the PP+PS=SS method of Grechka and Tsvankin (2002). First, we discuss how the PP+PS=SS method can be combined with VILS to construct SS-wave moveout in the target layer and overburden from PP and PS data. Then the interval S-wave attenuation coefficient is obtained by extending the kinematic construction procedure to frequency-domain amplitudes processed using the spectral-ratio method. Finally, we apply the algorithm to synthetic data from layered VTI and orthorhombic media to assess the accuracy of the inversion for the SV-wave attenuation-anisotropy parameters.

2.2 Methodology

Our method operates with pure (PP) and mode-converted (PS) reflections for a medium with an arbitrarily anisotropic, heterogeneous target layer overlaid by a laterally homogeneous overburden with a horizontal symmetry plane in each layer. For simplicity, the method is described for 2D models, in which the vertical incidence plane containing sources and receivers is supposed to be a plane of mirror symmetry. Therefore, both rays and the corresponding phase-velocity vectors are confined to the incidence plane, and converted waves represent in-plane polarized PSV modes. The P-to-S conversion for all reflection events is assumed to occur only at the reflector. For wide-azimuth data, the split mode-converted waves have to be separated for each offset and azimuth, which in general requires application of Alford-type rotation (Simmons, 2009; Dellinger et al., 2002; Gaiser, 1997). We begin by introducing the kinematic algorithm designed to compute the interval shear-wave traveltimes and then describe estimation of the interval shear-wave attenuation coefficient in the target layer.

2.2.1 Kinematic layer stripping for interval shear-wave traveltimes

To estimate the interval shear-wave traveltimes, the PP+PS=SS method can be combined with velocity-independent layer stripping developed by Dewangan and Tsvankin (2006). Suppose P-wave sources and receivers of both P- and S-waves are continuously distributed along the acquisition line. As discussed by Grechka and Tsvankin (2002), matching time slopes on common-receiver gathers at the source location A allows me to identify the PP (ARB) and PS (ARC) target events that share the downgoing segment AR and the reflection point R at the bottom of the target layer (Figure 2.1). Likewise, for a P-wave source at B, we find PP (BRA) and PS (BRD) target events that share the downgoing segment BR. This procedure makes it possible to construct the SS reflection DRC, where C and D are the coordinates of S-wave receivers. For brevity, we denote the PP (ARB) and PS (ARC and BRD) events by $\mathrm{PP_E}$, $\mathrm{PS_{E1}}$, and $\mathrm{PS_{E2}}$ (respectively) and the constructed SS event DRC by $\mathrm{SS_E}$ ("E" refers to "effective" reflections from the bottom of the target layer). The exact traveltime of the reflection $\mathrm{SS_E}$ is (Grechka and Tsvankin, 2002)

$$t_{SS_E} = t_{PS_{E1}} + t_{PS_{E2}} - t_{PP_E}. \tag{2.1}$$

The constructed event $\mathrm{SS_E}$ can be treated (in a kinematic sense) as a pure reflection mode excited by a shear-wave source.

Next, we find the interval SS-wave traveltime in the target layer, which requires knowledge of the shear traveltimes in the overburden. Since the data are assumed to be generated with a P-wave source, it is necessary to apply the PP+PS=SS method repeatedly to construct SS reflections in the overburden (Figure 2.2). To layer-strip the segment DR of the SS-wave, we need to obtain the coordinate of point I and the traveltime along the overburden segment ID. Note that the horizontal slowness along any ray in the laterally homogeneous overburden is preserved.

First, we form a common-receiver gather of the PS-wave at location D and identify the point E (i.e., the location of P-wave source) where the time slope (horizontal slowness) coincides with that at D. The obtained overburden PS event EID shares the segment ID

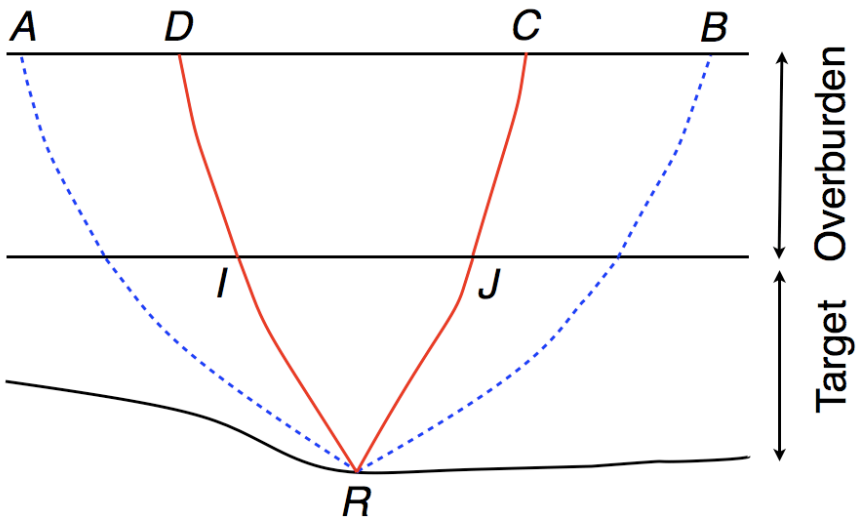

Figure 2.1. 2D ray diagram illustrating the PP+PS=SS method for PP and PS reflections from the bottom of the target layer. The wavefield is excited in split-spread geometry by P-wave sources located at points A and B. Target PP (ARB) and PS (ARC) events share the downgoing segment AR and, therefore, the reflection point R at the bottom of the target layer. Another pair of PP (BRA) and PS (BRD) target events share the downgoing segment BR. The constructed SS target event corresponds to DRC. P-wave ray segments are marked by dashed blue lines, and S-wave ray segments by solid red curves.

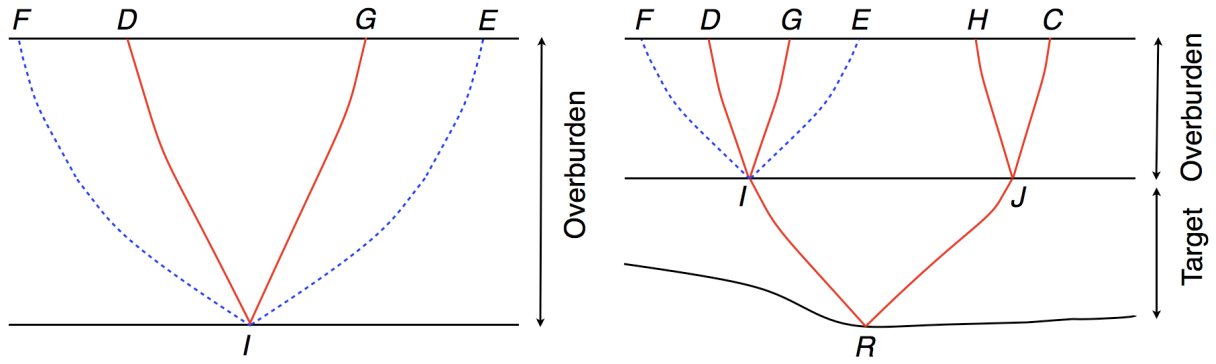

(a) (b)

Figure 2.2. Layer stripping of the constructed SS events. (a) The PP+PS=SS method is applied to kinematically construct pure SS-waves in the overburden. PP (EIF) and PS (EID) events share the downgoing segment EI and the reflection point I at the bottom of the overburden. Another pair of PP (FIE) and PS (FIG) overburden events share the downgoing segment FI. The overburden events that share the reflection point I are labeled O_1. (b) The constructed overburden SS event DIG shares the segment DI with the target SS reflection. The overburden events that share the reflection point J are labeled O_2.

with the target SS event $CJRID$ (Figure 2.2b). Then I form a common-source PP gather at location E and identify the receiver location F where the time slope (horizontal slowness) coincides with that at E (and hence at D). Since the horizontal slowness does not change along each ray in the overburden, the PP reflection recorded at F shares the downgoing segment EI with the PS event EID (Figure 2.2a).

Under our assumptions, the moveout function of the overburden PS event is symmetric with respect to zero offset, so the PS-wave traveltime and ray parameter remain the same when the source and receiver are interchanged. Therefore, the offset of the PS event FIG, which has the same reflection point and ray parameter as events EIF and EID, should coincide with that of the "reciprocal" PS reflection EID. The horizontal coordinate of the receiver at point G can then be found from

$$x_G = x_E + x_F - x_D. \tag{2.2}$$

The constructed event DIG (denoted by $\mathrm{SS}_{\mathrm{O1}}$, where "O" refers to the overburden and "1" to the left segment of the target SS event in Figure 2.2b) shares the segment DI with the

target SS event DRC (Figure 2.2b). The PP event EIF will be denoted by $\mathrm{PP_{O1}}$ and the PS events EID and FIG by $\mathrm{PS_{O1}}$. The traveltime of the event $\mathrm{SS_{O1}}$ is then given by

$$t_{SS_{O1}} = 2\,t_{PS_{O1}} - t_{PP_{O1}}, \tag{2.3}$$

and the lateral coordinate of point I is

$$x_{_I} = \frac{x_{_D} + x_{_G}}{2}. \tag{2.4}$$

Likewise, the PP+PS=SS method can be applied to construct the overburden SS event HJC ($\mathrm{SS_{O2}}$) that shares the segment JC with the target event $\mathrm{SS_E}$ (Figure 2.3). The corresponding traveltime $t_{SS_{O2}}$ and the lateral coordinate of point J are obtained using the algorithm discussed above. Hence, we can find the interval shear-wave traveltime in the target layer as

$$t_{SS_{_T}} = t_{SS_{_E}} - \frac{1}{2}\Big(t_{SS_{O1}} + t_{SS_{O2}}\Big). \tag{2.5}$$

The traveltime $t_{SS_{_T}}$ corresponds to the raypath IRJ of the target event $\mathrm{SS_T}$. Note that the depth of the bottom of the overburden remains unknown prior to velocity analysis.

For horizontal, laterally homogeneous target layers, the ray parameter is preserved along the entire raypath of the reflection $\mathrm{SS_E}$. If the target layer also has a horizontal symmetry plane, the raypaths of the downgoing and upgoing overburden events are symmetric with respect to the vertical. Then $t_{SS_{O1}} = t_{SS_{O2}}$, and it is sufficient to apply the layer-stripping procedure just to one of the overburden segments of the target event $\mathrm{SS_E}$.

2.2.2 Layer stripping for interval shear-wave attenuation

Behura and Tsvankin (2009a) combine VILS with the spectral-ratio method and apply their attenuation layer-stripping algorithm to frequency-domain amplitudes of pure-mode reflections. Our goal is to extend this technique to the combination of PP- and PS-waves analyzed above. The ray-theoretic frequency-domain amplitudes of the waves $\mathrm{PP_E}$, $\mathrm{PS_{E1}}$ and $\mathrm{PS_{E2}}$ (Figure 2.1) can be written as

$$|U_{PP_{_E}}| = S(\omega)\,\mathcal{G}_{\,PP_{_E}}\; e^{-k^I_{P,AR}\,l_{AR} - k^I_{P,BR}\,l_{BR}}, \tag{2.6}$$

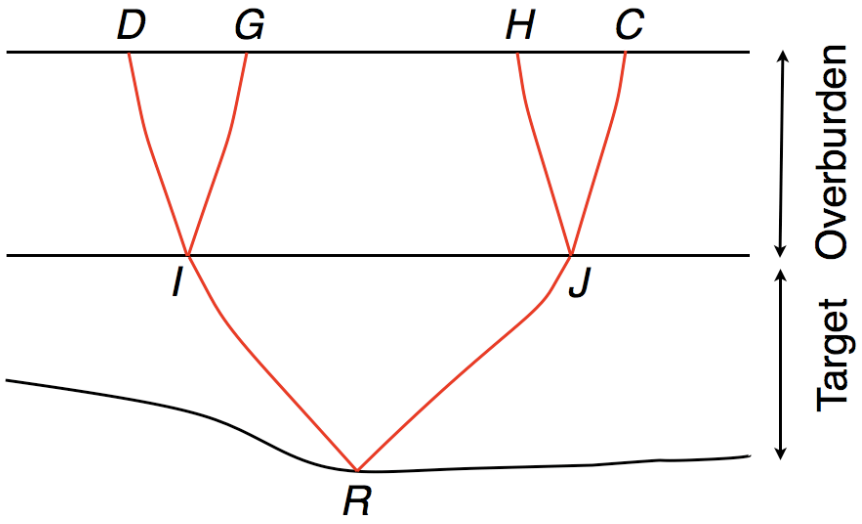

Figure 2.3. Raypaths of the constructed SS events. The target SS event DRC shares the segments ID and JC with the overburden events DIG and HJC, respectively. The method produces the interval traveltime along the raypath IRJ.

$$|U_{PS_{E1}}| = S(\omega)\, \mathcal{G}_{PS_{E1}}\; e^{-k^I_{P,AR}\, l_{AR}}\; e^{-k^I_{S,RC}\, l_{RC}}, \tag{2.7}$$

$$|U_{PS_{E2}}| = S(\omega)\, \mathcal{G}_{PS_{E2}}\; e^{-k^I_{P,BR}\, l_{BR}}\; e^{-k^I_{S,RD}\, l_{RD}}, \tag{2.8}$$

where $S(\omega)$ is the spectrum of the source wavelet, and $k^I_{P,XY}$ and $k^I_{S,XY}$ are the average P- and S-wave group attenuation coefficients (respectively) along the raypath XY with the length l_{XY}. The coefficients $\mathcal{G}_{PP_E}$, $\mathcal{G}_{PS_{E1}}$, and $\mathcal{G}_{PS_{E2}}$ include the source radiation pattern and receiver directivity, the reflection/transmission coefficients along the raypath, and the geometrical spreading of the corresponding event. Equations 2.6, 2.7, and 2.8 can be combined in the following way to compute the attenuation coefficient of the reflection $\mathrm{SS_E}$ constructed by the PP+PS=SS method:

$$|U_{SS_E}| = \frac{|U_{PS_{E1}}|\,|U_{PS_{E2}}|}{|U_{PP_E}|} = \mathcal{G}_E\, S(\omega)\, e^{-k^I_{S,RD}\, l_{RD} - k^I_{S,RC}\, l_{RC}}, \tag{2.9}$$

where the ratio $\mathcal{G}_E = (\mathcal{G}_{PS1_E}\, \mathcal{G}_{PS2_E})/\mathcal{G}_{PP_E}$ is assumed to be independent of frequency. It should be noted that $|U_{SS_E}|$ in equation 2.9 does not represent the actual amplitude of the primary SS reflection. Whereas the PP+PS=SS method reproduces the kinematics of

shear-wave primaries, it cannot yield the true amplitudes without knowledge of the velocity model (Grechka and Tsvankin, 2002; Grechka and Dewangan, 2003). Equation 2.9 can be used to evaluate effective S-wave attenuation by computing the slope of $\ln|U_{SS_E}|$ expressed as a function of ω. This operation, however, is hampered by the need to estimate the source spectrum $S(\omega)$, which is often difficult to do in practice.

However, as shown below, $S(\omega)$ is eliminated in the computation of the interval S-wave attenuation coefficient. The ray-theoretic frequency-domain amplitudes of the waves $\mathrm{PP}_{\mathrm{O1}}$ and $\mathrm{PS}_{\mathrm{O1}}$ (Figure 2.2) can be written as

$$|U_{PP_{O1}}| = S(\omega)\,\mathcal{G}_{PP_{O1}}\,e^{-k^I_{P,O1}\,(l_{EI}+l_{IF})} = S(\omega)\,\mathcal{G}_{PP_{O1}}\,e^{-2\,k^I_{P,O1}\,l_{EI}}, \tag{2.10}$$

$$|U_{PS_{O1}}| = S(\omega)\,\mathcal{G}_{PS_{O1}}\,e^{-k^I_{P,O1}\,l_{EI}}\,e^{-k^I_{S,O1}\,l_{ID}}, \tag{2.11}$$

where $k^I_{P,O1}$ and $k^I_{S,O1}$ are the average P-wave and S-wave group attenuation coefficients along the corresponding raypaths. Equations 2.10 and 2.11 can be combined to find the attenuation of the constructed shear-wave $\mathrm{SS}_{\mathrm{O1}}$ in the overburden:

$$|U_{SS_{O1}}| = \frac{|U_{PS_{O1}}|^2}{|U_{PP_{O1}}|} = \mathcal{G}_{O1}\,S(\omega)\,e^{-2\,k^I_{S,O1}\,l_{ID}}, \tag{2.12}$$

where $\mathcal{G}_{O1} = \mathcal{G}^2_{PS_{O1}}/\mathcal{G}_{PP_{O1}}$. Likewise, the attenuation coefficient for the overburden event $\mathrm{SS}_{\mathrm{O2}}$ can be found from

$$|U_{SS_{O2}}| = \frac{|U_{PS_{O2}}|^2}{|U_{PP_{O2}}|} = \mathcal{G}_{O2}\,S(\omega)\,e^{-2\,k^I_{S,O2}\,l_{JC}}, \tag{2.13}$$

The problem of estimating the interval shear-wave attenuation in the target layer (see Figure 2.3) is now reduced to the attenuation analysis of pure modes considered by Behura and Tsvankin (2009a). Equations 2.9, 2.12 and 2.13 can be combined as follows:

$$|U_{SS_T}| = \frac{|U_{SS_E}|^2}{|U_{SS_{O1}}|\,|U_{SS_{O2}}|} = \mathcal{G}_T\,e^{-2(\,k^I_{S,DR}\,l_{DR}+k^I_{S,RC}\,l_{RC})+2\,(k^I_{S,O1}\,l_{ID}+k^I_{S,O2}\,l_{JC})}, \tag{2.14}$$

where $\mathcal{G}_T = \mathcal{G}^2_E/\,(\mathcal{G}_{O1}\,\mathcal{G}_{O2})$. Since $k^I_{S,DR}\,l_{DR} = k^I_{S,IR}\,l_{IR} + k^I_{S,O1}\,l_{ID}$ and $k^I_{S,RC}\,l_{RC} = k^I_{S,RJ}\,l_{RJ} + k^I_{S,O2}\,l_{JC}$, equation 2.14 reduces to:

$$|U_{SS_T}| = \mathcal{G}_T\,e^{-2\,k^I_{S,IR}\,l_{IR}\,-2\,k^I_{S,RJ}\,l_{RJ}}. \tag{2.15}$$

Taking the logarithm of equation 2.15 yields:

$$\ln|U_{SS_T}| = \ln \mathcal{G}_T - 2\,k^I_{S,IR}\,l_{IR} - 2\,k^I_{S,RJ}\,l_{RJ} = \ln \mathcal{G}_T - 2\,k^I_{S,T}\,(l_{IR} + l_{RJ}), \tag{2.16}$$

where the coefficient $k^I_{S,T}$ represents the average group attenuation coefficient along the SS-wave raypath in the target layer.

2.2.3 Interval attenuation for a homogeneous target layer

If the target layer is heterogeneous, equation 2.16 can yield only the offset-dependent average interval S-wave attenuation coefficient, provided the length of the shear-wave raypath ($l_{IR} + l_{RJ}$) is known. Interpretation of attenuation measurements, however, can be significantly simplified for horizontal, homogeneous layers with a horizontal symmetry plane. Then

$l_{IR} + l_{RJ} = V_g\,t_{SS_T}$, where V_g is the shear-wave group velocity along the rays IR and RJ (Figure 2.3), and t_{SS_T} is the SS-wave interval traveltime in the target layer. As a result, equation 2.16 reduces to

$$\ln|U_{SS_T}| = \ln \mathcal{G}_T - 2\,k^I_{S,T}\,V_g\,t_{SS_T}. \tag{2.17}$$

Behura and Tsvankin (2009c) show that equation 2.17 can be used to obtain the *phase* attenuation coefficient. According to their results,

$$\ln|U_{SS_T}| = \ln \mathcal{G}_T - 2\,\omega\,\mathcal{A}_S\,t_{SS_T}, \tag{2.18}$$

where ω is the angular frequency and $\mathcal{A}_S = k^{I,Ph}/k^{R,Ph}$ is the S-wave phase attenuation coefficient (Zhu, 2006); $k^{R,Ph}$ and $k^{I,Ph}$ are the magnitudes of the real and imaginary parts of the wave vector $\mathbf{k}$. The angle dependent quality factor Q_S in anisotropic media is usually defined as $Q_S = 1/(2\mathcal{A}_S)$. As proved by Behura and Tsvankin (2009c), the coefficient $\mathcal{A}_S$ in equation 2.18 has to be evaluated for a zero inhomogeneity angle ξ (the angle between the real and imaginary parts of $\mathbf{k}$), irrespective of the actual value of ξ for the ray direction IR. In other words, $\mathcal{A}_S$ is found for the imaginary part of $\mathbf{k}$ aligned with the phase (slowness) direction. This result does not hold only for uncommonly large values of the angle ξ.

The shear-wave interval traveltime in the target layer (t_{SS_T}) is computed from equation 2.5 using the kinematic layer stripping. Hence, the slope of the logarithmic spectral ratio in equation 2.18 yields the phase attenuation coefficient $\mathcal{A}_S$ for the phase angle corresponding to the group direction IR in Figure 2.3. If the slope is constant, the coefficient $\mathcal{A}_S$ and the quality factor $Q_S \approx 1/(2\,\mathcal{A}_S)$ are independent of frequency. If the slope varies with frequency, $\mathcal{A}_S$ has to be computed from the instantaneous slope, which yields a frequency-dependent quality factor.

Below we apply the method to estimation of shear-wave interval attenuation coefficients in VTI media and symmetry planes of orthorhombic media. For vertical transverse isotropy, the coefficient $\mathcal{A}_S$ can be inverted for the attenuation-anisotropy parameters introduced by Zhu and Tsvankin (2006, 2007). Under the assumptions of weak attenuation and weak velocity and attenuation anisotropy, the SV-wave phase attenuation coefficient is given by (Zhu and Tsvankin, 2006):

$$\mathcal{A}_{SV}(\theta) = \mathcal{A}_{S0}\,(1 + \sigma_{_Q}\,\sin^2\theta\,\cos^2\theta), \tag{2.19}$$

$$\sigma_{_Q} = \frac{1}{g_{_Q}}\left[2\,(1 - g_{_Q})\,\sigma + \frac{\epsilon_{_Q} - \delta_{_Q}}{g}\right], \tag{2.20}$$

where $\mathcal{A}_{S0} \approx 1/(2Q_{S0})$ is the shear-wave symmetry-direction attenuation coefficient (it is the same for SV- and SH-waves), $g_{_Q} = Q_{_{P0}}/Q_{_{S0}}$, $Q_{_{P0}}$ and $Q_{_{S0}}$ are the vertical quality factors for P- and S-waves, respectively, and $\epsilon_{_Q}$ and $\delta_{_Q}$ are the attenuation anisotropy parameters, $g = V_{P0}^2/V_{S0}^2$, where V_{P0} and V_{S0} are the vertical velocities of P- and S-waves, respectively, $\sigma = (\epsilon - \delta)/g$, and ϵ and δ are the velocity anisotropy parameters. The parameter $\sigma_{_Q}$ determines the variation of $\mathcal{A}_{SV}$ away from the symmetry direction.

If the model is orthorhombic and the symmetry of the real and imaginary parts of the stiffness matrix is the same, the VTI equations for the attenuation coefficients can be adapted for the mutually orthogonal symmetry planes (Zhu and Tsvankin, 2007). Here, the symmetry planes of orthorhombic media are taken to coincide with the Cartesian coordinate planes. It should be noted that in-plane polarized SV-waves in the vertical symmetry planes represent two different shear modes, fast S_1 and slow S_2 (Tsvankin, 1997, 2005). Suppose

the fast wave S_1 at vertical incidence is polarized in the x_1-direction (i.e., it represents an SV mode in the [x_1, x_3]-plane), and the slow wave S_2 in the x_2-direction. Then P-waves are coupled to to S_1-waves in the [x_1, x_3]-plane and to S_2-waves in the [x_2, x_3]-plane.

The linearized SV-wave phase attenuation coefficient in the [x_1, x_3]-plane, adapted from equations 2.19-2.20, has the form:

$$\mathcal{A}_S^{(2)} = \mathcal{A}_{S0}\,(1 + \sigma_Q^{(2)}\,\sin^2\theta\,\cos^2\theta), \tag{2.21}$$

where θ is the phase angle with the vertical, $\mathcal{A}_{S0}$ is the vertical attenuation coefficient of the S_1-wave, and $\sigma_Q^{(2)}$ is the SV-wave attenuation-anisotropy parameter in the [x_1, x_3]-plane defined by Zhu and Tsvankin (2007). (The superscript "(2)" denotes the x_2-axis orthogonal to the [x_1, x_3]-plane.) Similarly, the SV-wave attenuation coefficient in the [x_2, x_3] symmetry plane is given by

$$\mathcal{A}_S^{(1)} = \bar{\mathcal{A}}_{S0}(1 + \sigma_Q^{(1)}\,\sin^2\theta\,\cos^2\theta), \tag{2.22}$$

where $\bar{\mathcal{A}}_{S0}$ is the vertical attenuation coefficient of the S_2-wave and $\sigma_Q^{(1)}$ is the corresponding attenuation-anisotropy parameter.

Zhu and Tsvankin (2007) define the *attenuation splitting parameter* $\gamma_Q^{(S)}$ by analogy with the S-wave velocity splitting parameter $\gamma^{(S)}$ as the fractional difference between the attenuation coefficients of the vertically traveling split shear waves:

$$\gamma_Q^{(S)} \equiv \left|\frac{\bar{\mathcal{A}}_{S0} - \mathcal{A}_{S0}}{\mathcal{A}_{S0}}\right|. \tag{2.23}$$

The coefficient $\gamma_Q^{(S)}$ is expected to play an important role in characterization of fractured reservoirs using shear-wave attenuation measurements.

Inversion of equations 2.19, 2.21, and 2.22 requires knowledge of the phase angle θ corresponding to each source-receiver offset (e.g., to IJ in Figure 2.3) at the top of the target layer. However, since equations 2.19, 2.21, and 2.22 were derived in the linearized weak-anisotropy approximation, the phase and group angles in the anisotropic terms are interchangeable. Therefore, the angle θ can be replaced with the corresponding group angle computed from the known offset using an approximate thickness of the target layer.

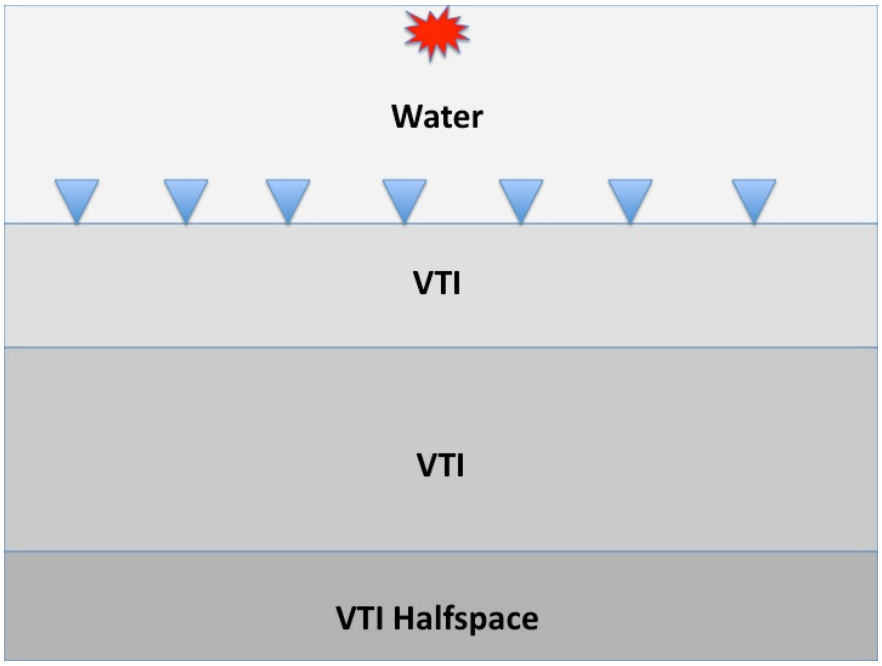

Figure 2.4. Synthetic model used to test the algorithm. The source is at the surface and the receivers are at the water bottom. The model parameters are listed in Table 1.

2.3 Synthetic examples

The method was tested on synthetic multicomponent data from horizontally layered VTI and orthorhombic models (Figure 2.4). The source was placed at the top of the model, while the receivers were at the water bottom. Our method is applicable to this source-receiver geometry because it utilizes events with shared ray segments in the overburden.

2.3.1 Layered VTI media

Synthetic reflection data were generated using an anisotropic reflectivity code (Schmidt and Tango, 1986). The interval parameters for the model (Table 2.1) were chosen so as to simulate significant P- and S-wave attenuation and attenuation anisotropy. A broadband (0.1 – 150 Hz) source wavelet employed in the reflectivity method ensured that the spectral-ratio method could operate with a sufficient number of frequencies. PP and PS events from the top and bottom of the third (target) layer were identified on the vertical and radial

Table 2.1. Synthetic model used to estimate SV-wave interval attenuation in VTI media.

	Layer 1	Layer 2	Layer 3	Halfspace
Symmetry	Isotropic	VTI	VTI	VTI
d (km)	2.00	0.60	1.00	–
V_{P0} (km/s)	1.50	1.60	1.70	2.00
V_{S0} (km/s)	–	0.80	0.90	1.20
ϵ	–	0.30	0.25	0.40
δ	–	0.10	0.10	0.20
σ	–	0.80	0.54	0.56
Q_{P0}	–	50	100	60
Q_{S0}	–	50	20	70
$\epsilon_{_Q}$	–	0.30	0.20	0.40
$\delta_{_Q}$	–	0.20	0.10	0.30
$\sigma_{_Q}$	–	0.40	-0.78	0.08

displacement components of the shot gather (Figure 2.5). Kinematic layer stripping of the shear-wave traveltimes (equation 2.5) produced the interval moveout in the target layer shown in Figure 2.6. The layer-stripped interval traveltimes practically coincide with the exact values computed by ray tracing. It should be noted that the maximum offset for the constructed shear-wave in the target layer is limited by the critical angle for SP mode conversions, which is equal to 32°. The critical angle, however, is reached only for infinitely large offsets of the acquired PP- and PS-waves.

The input amplitudes were obtained by computing the vector sum of the radial and vertical displacement components. Frequency-domain amplitudes were found by putting a tapered cosine window (with a length of 128 time samples) around the arrivals and applying the Fourier transform. The target layer is horizontal, homogeneous, and (as any VTI medium) has a horizontal plane of symmetry. Therefore, the interval shear-wave phase attenuation coefficient in the target was computed from equation 2.18 using the algorithm discussed above. Attenuation coefficients for offsets corresponding to spectral contamination by multiples were removed. The SV-wave phase angles were obtained from the corresponding group angles using the known velocity function in the target layer. The parameters

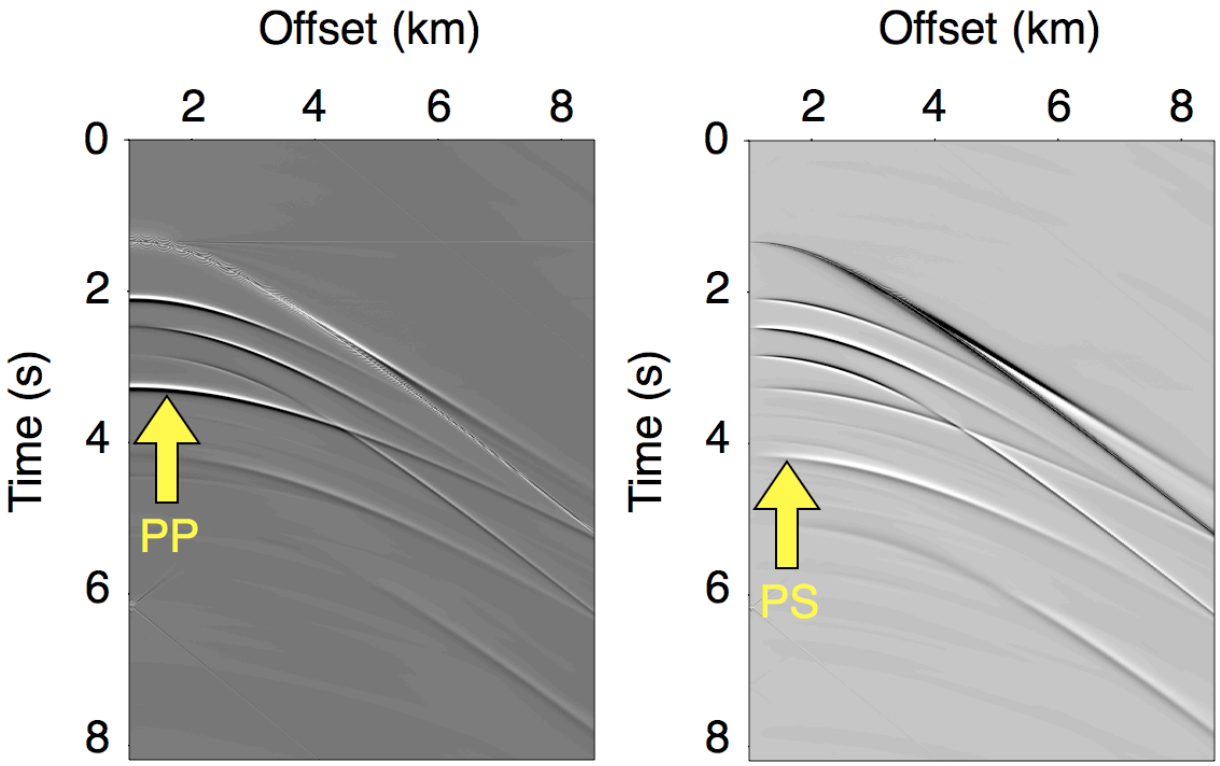

Figure 2.5. (a) Vertical and (b) horizontal displacement components of a shot gather for the model from Figure 2.4. The PP (plot a) and PS (b) reflections from the bottom of the target (third) layer are marked by arrows.

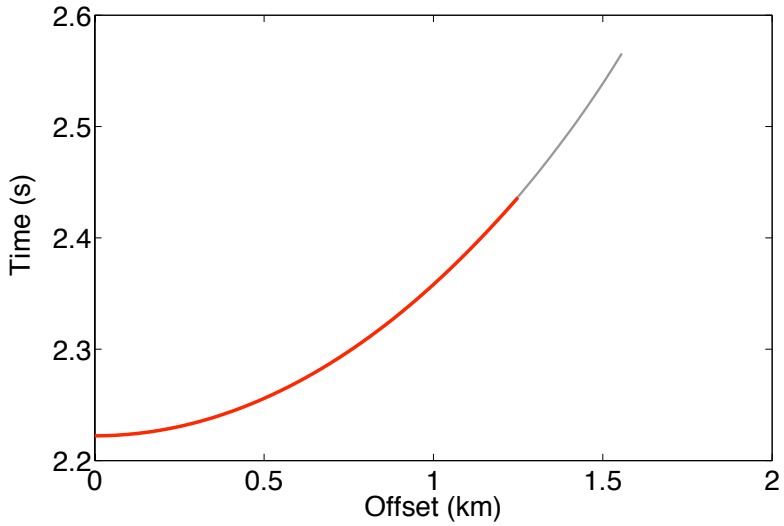

Figure 2.6. Interval shear-wave traveltime (red dots) in the target layer computed using the PP+PS=SS method and velocity-independent layer-stripping. The gray curve marks the exact traveltime.

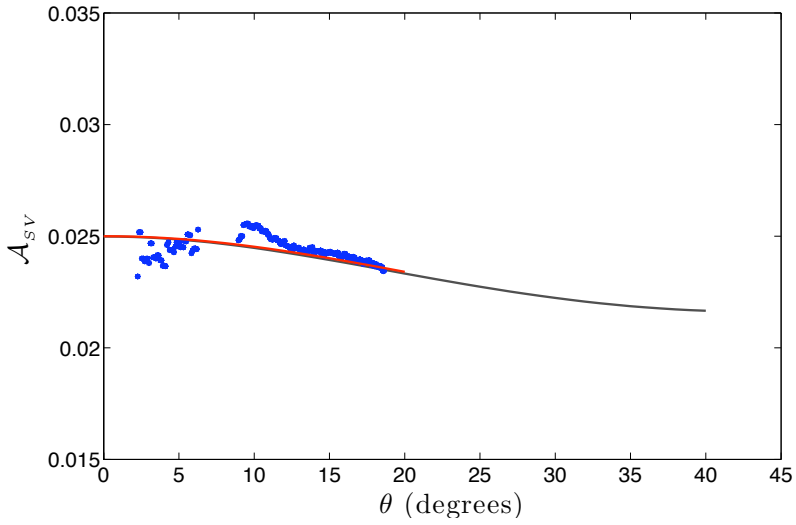

Figure 2.7. Estimated SV-wave interval phase attenuation coefficient $\mathcal{A}_{SV}$ in the target layer (blue dots) as a function of the phase angle θ. Attenuation coefficients corresponding to spectral contamination by multiples have been removed. The red and gray lines are the best-fit and exact coefficients $\mathcal{A}_{SV}$, respectively.

$\mathcal{A}_{S0} = 0.025 \pm 10^{-4}$ and $\sigma_{_Q} = -0.72 \pm 0.20$ were found by least-squares fitting of equation 2.19 to the estimated shear-wave phase attenuation coefficient $\mathcal{A}_{SV}$ (Figure 2.7), with the error bars corresponding to the standard deviations from the best-fit function. The inverted parameter $\mathcal{A}_{S0}$ practically coincides with its actual value, but there is a significant uncertainty in the estimate of $\sigma_{_Q}$ (the actual value is -0.78) due to the limited range of phase angles for the reflected S-leg of the PS-wave and the small PS-wave reflection coefficient at near-vertical incidence. For this model, equation 2.19 provides a close approximation to the exact attenuation coefficient. Then, we added Gaussian noise to the radial and vertical displacement components of the PP- and PS-events, which resulted in a signal-to-noise ratio of 2.5. The inversion of the noise-contaminated data yielded an accurate coefficient $\mathcal{A}_{S0} = 0.0246 \pm 2 \times 10^{-4}$, while the estimate of $\sigma_{_Q} = -0.60 \pm 0.30$ is somewhat biased. The bandwidth used in the spectral-ratio method has to be chosen in a frequency range where the signal-to-noise ratio is sufficiently high. To obtain a robust estimate of the slope from the logarithmic spectral ratio, we employed the iteratively reweighted least-squares method (Scales and Gersztenkorn, 1988; Aster et al., 2005). The inversion for the attenuation coefficients was performed for 100 realizations of Gaussian noise. The hence obtained mean values and pooled standard deviations of the coefficients are $\mathcal{A}_{S0} = 0.0246 \pm 2 \times 10^{-4}$ and $\sigma_{_Q} = -0.60 \pm 0.30$.

2.3.2 Symmetry planes of layered orthorhombic media

Next, we consider a model that includes two horizontal orthorhombic layers with aligned vertical symmetry planes (Table 2.2). The acquisition geometry shown in Figure 2.4 was used to generate synthetic data in the vertical symmetry planes [x_1, x_3] and [x_2, x_3] with the same anisotropic reflectivity code. The 2D version of our method for estimating interval attenuation is entirely valid in both vertical symmetry planes, if the symmetry-plane azimuths do not vary with depth. In contrast to VTI media, geometric spreading in orthorhombic media is influenced by azimuthal velocity variations even within the symmetry planes (Tsvankin, 2005, Chapter 2). The geometric-spreading factor, however, is treated as

Table 2.2. Synthetic model used to estimate shear-wave interval attenuation in symmetry planes of orthorhombic media. The vertical symmetry planes in layers 2 – 4 are aligned.

	Layer 1	Layer 2	Layer 3	Halfspace
Symmetry	Isotropic	Orthorhombic	Orthorhombic	Orthorhombic
d (km)	2.00	0.60	1.00	–
V_{P0} (km/s)	1.50	1.60	1.70	2.50
V_{S0} (km/s)	–	0.80	1.00	1.40
$\epsilon^{(2)}$	–	0.25	0.40	0.30
$\delta^{(2)}$	–	0.10	0.30	0.10
$\sigma^{(2)}$	–	0.60	0.29	0.64
$\epsilon^{(1)}$	–	0.30	0.20	0.40
$\delta^{(1)}$	–	0.15	0.10	0.30
$\sigma^{(1)}$	–	0.65	0.43	0.38
$\gamma^{(S)}$	–	0.04	0.25	0.10
Q_{P0}	–	40	50	60
Q_{S0}	–	40	30	50
$\epsilon_Q^{(2)}$	–	-0.20	0.30	0.40
$\delta_Q^{(2)}$	–	-0.10	-0.20	0.30
$\sigma_Q^{(2)}$	–	-0.32	0.64	0.05
$\epsilon_Q^{(1)}$	–	-0.30	0.25	0.40
$\delta_Q^{(1)}$	–	-0.20	-0.15	0.30
$\sigma_Q^{(1)}$	–	-0.58	1.22	0.38
$\gamma_Q^{(S)}$	–	0.12	0.34	0.17

part of the frequency-independent term of the amplitude function and does not influence inverted attenuation coefficients.

The synthetic data in the planes $[x_1,\, x_3]$ and $[x_2,\, x_3]$ (Figures 2.8 and 2.9) were processed separately. As discussed above, for symmetry-plane propagation the P-wave is coupled only to the in-plane polarized SV-wave (either S_1 or S_2). Therefore, only one mode conversion (PS_1 or PS_2) is recorded in each vertical symmetry plane. Due to shear-wave splitting at vertical incidence, the near-offset PS_1 and PS_2 reflections are shifted with respect to each other in time. The interval SS-wave moveout functions in the symmetry planes computed for the third (target) layer by kinematic layer stripping are close to the exact traveltimes (Figure 2.10). The critical angle for SP mode conversions, which restricts the offset range of

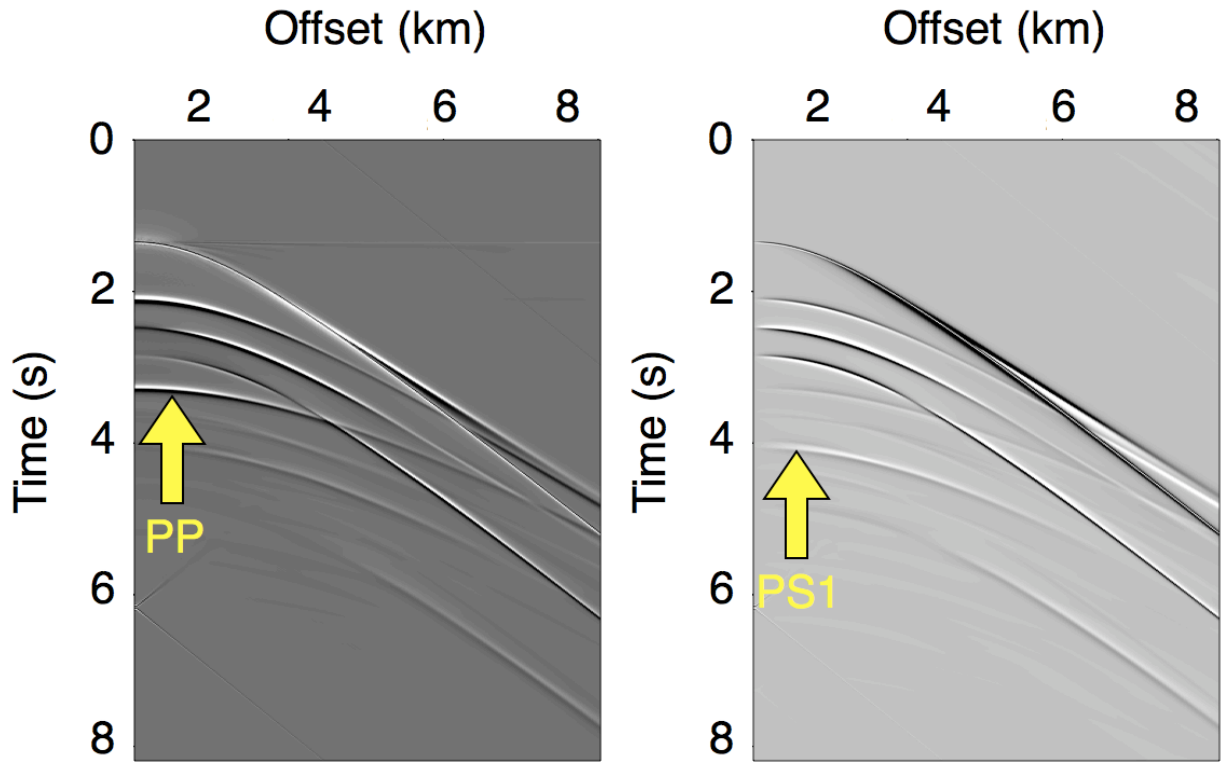

(a) (b)

Figure 2.8. (a) Vertical and (b) horizontal displacement components of a shot gather in the $[x_1, x_3]$-plane of the model from Table 2.2. The PP and PS reflections from the bottom of the target (third) layer are marked by arrows.

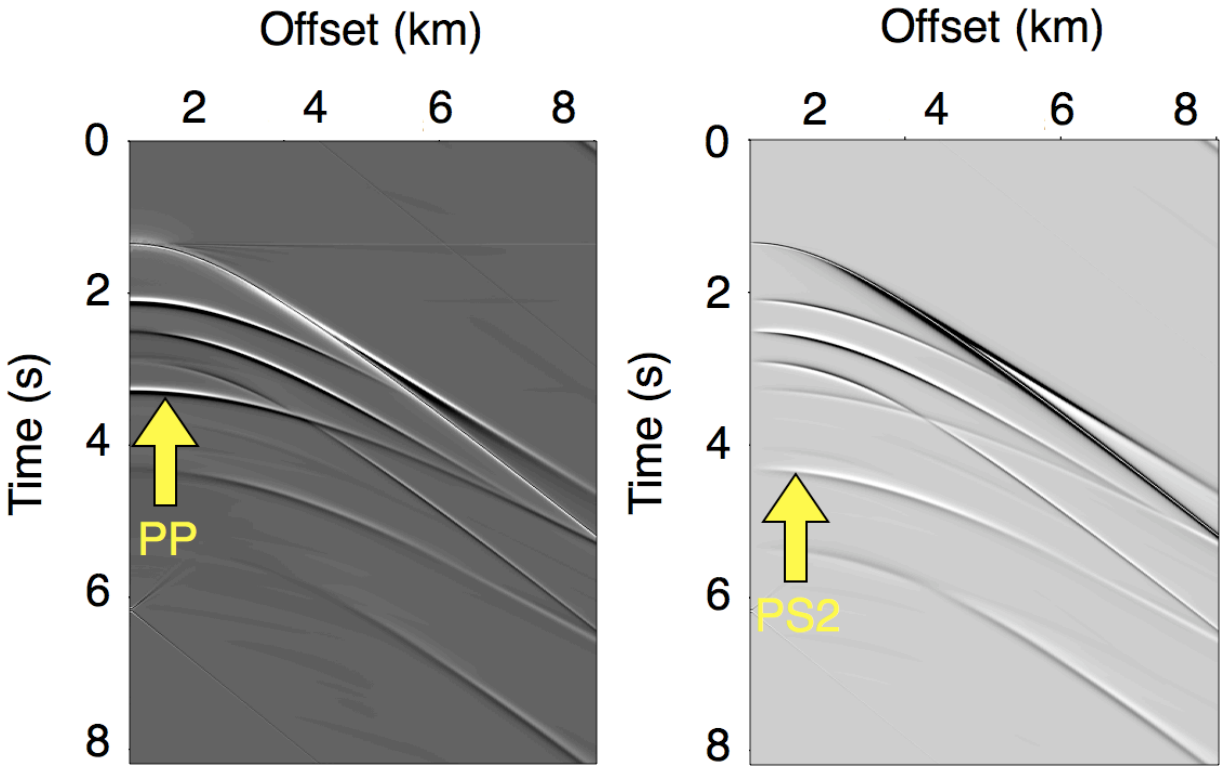

Figure 2.9. (a) Vertical and (b) horizontal displacement components of a shot gather in the $[x_2, x_3]$-plane of the model from Table 2.2. The PP and PS reflections from the bottom of the target layer are marked by arrows.

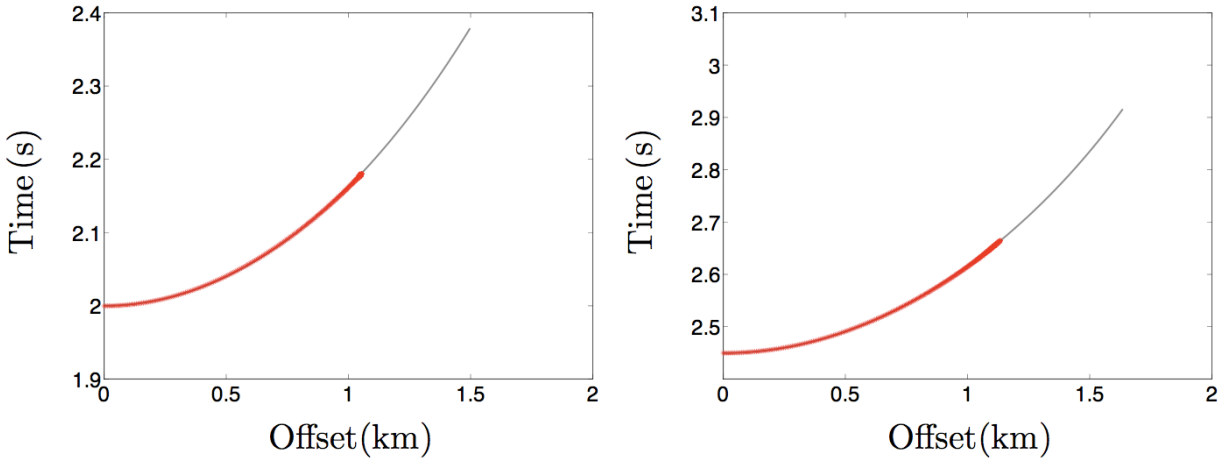

(a) (b)

Figure 2.10. Interval traveltimes (red dots) of the in-plane polarized S-wave in the target (third) layer computed using the PP+PS=SS method and velocity-independent layer-stripping for (a) $[x_1, x_3]$-plane and (b) $[x_2, x_3]$-plane. The gray curves mark the exact traveltimes.

the constructed SS-waves, is equal to 26° in the $[x_1, x_3]$-plane and 24° in the $[x_2, x_3]$-plane.

To estimate the attenuation parameters, we performed least-squares fitting of equations 2.21 and 2.22 to the computed symmetry-plane shear-wave interval attenuation coefficients (Figure 2.11). The obtained vertical attenuation coefficients $\mathcal{A}_{S0} = 0.0165 \pm 10^{-4}$ and $\bar{\mathcal{A}}_{S0} = 0.0124 \pm 3 \times 10^{-4}$ barely deviate from the actual parameters ($\mathcal{A}_{S0} = 0.0167$, $\bar{\mathcal{A}}_{S0} = 0.0125$) coincide with their actual values. Consequently, the method yields a highly accurate attenuation splitting parameter ($\gamma_Q^{(S)} = -0.33$). As is the case for the VTI model, the attenuation-anisotropy parameters $\sigma_Q^{(2)}$ and $\sigma_Q^{(1)}$ are more distorted and have larger standard deviations.

2.4 Discussion

Despite the generally successful test results, the proposed method has several limitations. First, the range of phase angles for the constructed SS-wave is restricted due to two factors: the small amplitudes of PS-waves at near offsets and the critical angle for converted

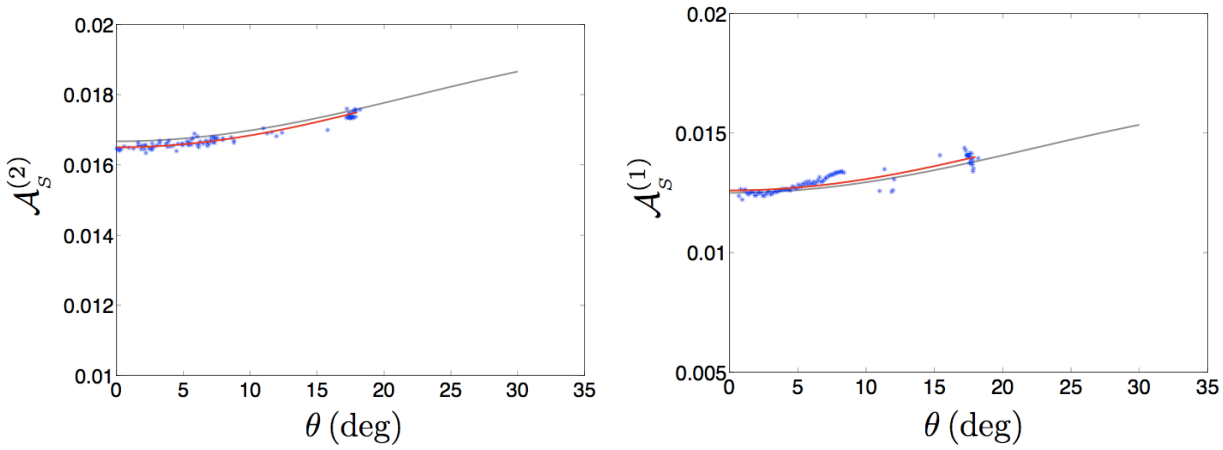

(a) (b)

Figure 2.11. Estimated S-wave interval phase attenuation coefficient $\mathcal{A}_{SV}$ (blue dots) in the third layer as a function of the phase angle θ for (a) $[x_1, x_3]$-plane and (b) $[x_2, x_3]$-plane. Attenuation coefficients corresponding to spectral contamination by multiples have been removed. The red and gray lines are the best-fit and exact attenuation coefficients. The best fit parameters are $\mathcal{A}_{S0} = 0.0165 \pm 10^{-4}$, $\bar{\mathcal{A}}_{S0} = 0.0124 \pm 3 \times 10^{-4}$, $\sigma_Q^{(2)} = 0.70 \pm 0.25$ and $\sigma_Q^{(1)} = 1.30 \pm 0.40$. The actual values are $\mathcal{A}_{S0} = 0.0167$, $\bar{\mathcal{A}}_{S0} = 0.0125$, $\sigma_Q^{(2)} = 0.64$ and $\sigma_Q^{(1)} = 1.22$.

waves. The critical angle seldom exceeds 30° – 35°, which may cause instability in the inversion for the attenuation-anisotropy parameter $\sigma_{_Q}$ in VTI media and parameters $\sigma_{_Q}^{(1,2)}$ in orthorhombic media. Estimation of $\sigma_{_Q}$ should be more accurate for hard rocks with high V_S/V_P ratios, for which the critical angle for SP mode conversions is larger. However, the algorithm should provide tight constraints on the vertical attenuation coefficients and, therefore, on the attenuation splitting parameter for orthorhombic media. Second, because the data are generated by a P-wave source, it is necessary to repeatedly apply the PP+PS=SS method to construct SS events, which could lead to error accumulation in the attenuation analysis. Third, the algorithm assumes that the source radiation pattern and the receiver directivity function are frequency independent (equation 2.9). This assumption is valid for point sources in weakly heterogeneous anisotropic media, if attenuation-related velocity dispersion in the seismic frequency band can be ignored. However, source and receiver arrays in particular acquisition geometries can produce a frequency-dependent directivity function, which may distort attenuation coefficients measured by the spectral-ratio method (Hustedt and Clark, 1999) or produce "artificial" attenuation-anisotropy signatures (Vasconcelos and Jenner, 2005).

Application of the algorithm to field data requires registration (correlation) of PP and PS data sets to identify reflections from the same interfaces. Then the traveltimes of the overburden and target PP and PS events can be found by nonhyperbolic semblance analysis (Vasconcelos and Tsvankin, 2006; Xu and Tsvankin, 2008). Kinematic layer stripping for both 2D data and 3D wide-azimuth surveys can be implemented using the methodology of Wang and Tsvankin (2009). As in the above synthetic example, the input amplitudes have to be found in a suitable time window around reflection arrivals. Since the algorithm is supposed to operate with isolated reflection events, amplitude distortions due to interference (e.g., with multiples) would hinder S-wave attenuation estimates. The impact of such interference may be mitigated by employing variable-window time-frequency transforms (Reine et al., 2009b). Appropriate smoothing filters in the frequency domain should help reduce errors in spectral-ratio estimates produced by notches in amplitude spectra. If lateral heterogeneity

is relatively weak, the algorithm can benefit from data redundancy because the attenuation coefficients for fixed offset and azimuth can be estimated from multiple traces.

Expressing $\mathcal{A}_{SV}$ as a function of the phase angle (equation 2.19) requires knowledge of the velocity function. However, as discussed by Behura and Tsvankin (2009a), the difference between the phase and group angles for moderately anisotropic models does not substantially distort attenuation coefficients. It should be mentioned, however, that even the group angle for a given source-receiver pair cannot be computed without depth information, which can be approximately obtained from hyperbolic moveout analysis of the interval shear-wave traveltimes.

2.5 Conclusions

We extended the algorithm of Behura and Tsvankin (2009a), originally introduced for pure modes, to the combination of PP- and PS-waves with the goal of estimating the shear-wave interval attenuation coefficient. The technique involves repeated application of the PP+PS=SS method followed by velocity-independent layer stripping (VILS), for both traveltime and frequency-domain amplitudes. In the 2D implementation of the method discussed here, the vertical incidence plane has to be a plane of mirror symmetry in all layers including the target horizon. VILS is designed for a laterally homogeneous (although possibly vertically heterogeneous) overburden with a horizontal symmetry plane in each layer. If this assumption is satisfied, our method does not require knowledge of the overburden velocity and attenuation parameters.

For heterogeneous target layers, the algorithm estimates the average S-wave interval group attenuation coefficient for a range of source-receiver offsets. If the target is horizontal, homogeneous, and has a horizontal symmetry plane, it is possible to obtain the offset-dependent interval phase attenuation coefficient for the constructed SS events.

Synthetic modeling for layered VTI and orthorhombic media confirmed the accuracy of the method in estimating the interval SV-wave phase attenuation coefficient $\mathcal{A}_{SV}$. The range of phase angles for the constructed SS reflection is limited by the small amplitudes of

PS-waves at near offsets and the critical angle for the reflected S-leg. The coefficient $\mathcal{A}_{SV}$ can be inverted for the symmetry-direction coefficient $\mathcal{A}_{S0}$ for VTI media and the vertical attenuation coefficients of the split S-waves for orthorhombic media. Therefore, application of the method to azimuthally anisotropic media helps evaluate the attenuation splitting parameter $\gamma_Q^{(S)}$, which may carry important information about fracturing. Under favorable circumstances (i.e., for long-offset data and layers with a relatively large V_S/V_P ratio) it may be possible to constrain the anisotropy parameters responsible for the variation of the SS-wave attenuation coefficient away from the vertical.

Joint analysis of the P- and S-wave attenuation coefficients can be used to detect the presence of fluids in a reservoir. In combination with the shear-wave velocity splitting parameter $\gamma^{(S)}$, its attenuation counterpart $\gamma_Q^{(S)}$ could serve as a potentially valuable fracture-detection attribute.

Chapter 3

ANISOTROPIC ATTENUATION ANALYSIS OF CROSS-HOLE DATA GENERATED DURING HYDRAULIC FRACTURING

Measurements of attenuation anisotropy can provide valuable information for reservoir characterization and monitoring. Here, we analyze a cross-hole data set generated by perforation shots fired in a horizontal borehole to induce hydraulic fracturing in a tight gas reservoir. The spectral-ratio method is applied to pairs of traces to set up a system of equations for directionally-dependent effective attenuation. The anisotropic attenuation coefficient is expanded in a quadratic function of the polar and azimuthal angles of the source-receiver line. The coefficients of this polynomial are found separately for each stage of perforation shots. Although the inversion provides clear evidence of attenuation anisotropy, the narrow range of propagation directions impairs the accuracy of anisotropy analysis. The observed variations of the attenuation coefficient between different perforation stages may be related to changes in the medium due to hydraulic fracturing and stimulation.

3.1 Introduction

Attenuation of seismic waves is sensitive to the physical properties of the subsurface and has been observed in vertical seismic profiling (VSP) and reflection data. De et al. (1994) report measurements of the P- and S-wave quality factors from VSP surveys and sonic logs. Maultzsch et al. (2007) evaluate P-wave azimuthal attenuation anisotropy from 3D VSP data acquired over a fractured hydrocarbon reservoir and infer fracture directions from attenuation analysis. Barnes (2010) estimates shear-wave attenuation using anisotropic full-waveform inversion of offshore VSP data acquired over a gas reservoir. Attenuation anisotropy has also been observed in P-wave reflection data (Clark et al., 2009; Vasconcelos

and Jenner, 2005).

Seismic attenuation is most commonly measured using the spectral-ratio method. Zhu et al. (2007a) extend the spectral-ratio method to anisotropic media and apply it to physical-modeling data acquired for a transversely isotropic (TI) sample. Other techniques proposed to measure attenuation include the instantaneous-frequency (Dasios et al., 2001), and frequency-shift methods (Quan and Harris, 1997b). These algorithms, however, require a broad range of frequencies and knowledge of the source spectrum, which is difficult to estimate in practice. In contrast, computing spectral ratios helps eliminate the source spectrum and can be used to obtain accurate effective and interval attenuation coefficients in layered anisotropic media (Behura and Tsvankin, 2009a; Shekar and Tsvankin, 2011).

Here, we present a case study with cross-hole data generated by perforation shots in a horizontal borehole and recorded in a vertical borehole. The spectral-ratio method applied to all pairs of traces yields a system of equations for the anisotropic attenuation coefficient. Since the acquisition aperture is narrow, we represent the directional dependence of the attenuation coefficient as a quadratic polynomial of the polar and azimuthal angles. The inversion results show that taking attenuation anisotropy into account reduces the data misfit and reveals changes in the attenuation coefficient between perforation stages. Interpretation of the attenuation measurements is not straightforward, but it provides indications of temporal changes related to hydraulic fracturing.

3.2 Methodology

The data used in this study were generated in a tight-gas reservoir by perforation shots fired at regular intervals in a horizontal borehole. The wavefield was recorded by 10 multicomponent receivers placed at different depths in a vertical (monitor) borehole (Figure 3.1). The perforation shots were grouped into successive "stages," as borehole perforations at each stage were followed by hydraulic stimulation of the perforation-induced fractures.

Multicomponent shot gathers were rotated to maximize the energy of the direct P-waves (Figure 3.2). After picking the P-wave arrivals, we applied a tapered cosine window around

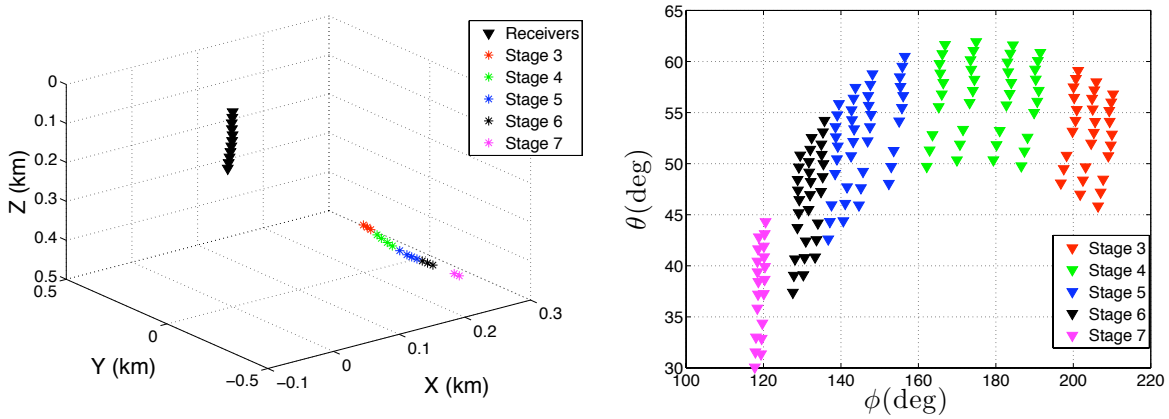

(a) (b)

Figure 3.1. Acquisition geometry of the experiment; the x-axis points east. The shots in a horizontal borehole are denoted by stars, with different colors corresponding to different stages. The receivers in a vertical borehole are denoted by black triangles. The shot and receiver positions are plotted (a) in the Cartesian coordinates, and (b) as functions of the polar (θ) and azimuthal (ϕ) angles of the source-receiver line.

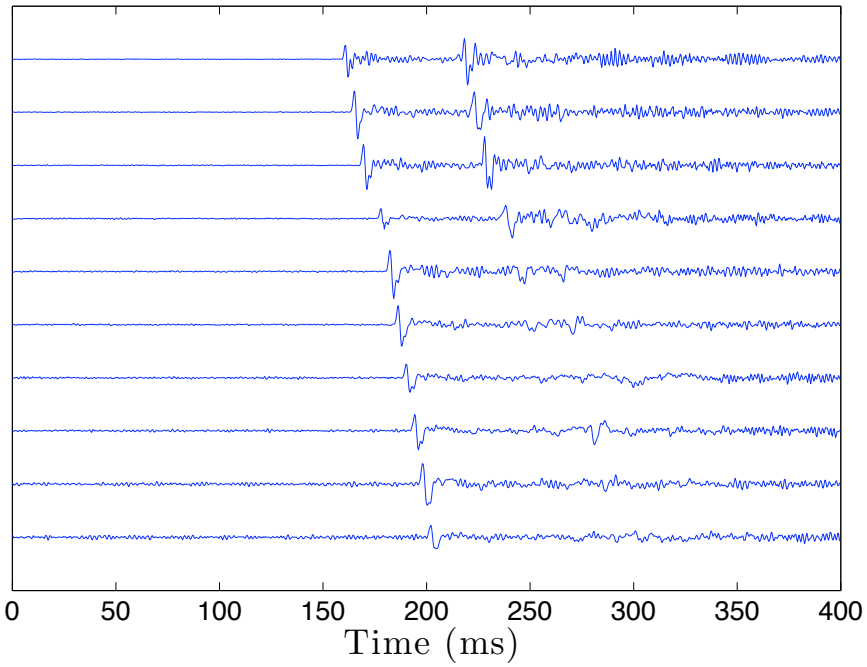

Figure 3.2. Typical shot gather from the data set. The first arrivals with a linear moveout are the direct P-waves. The recorded displacement components were rotated to enhance P-wave energy.

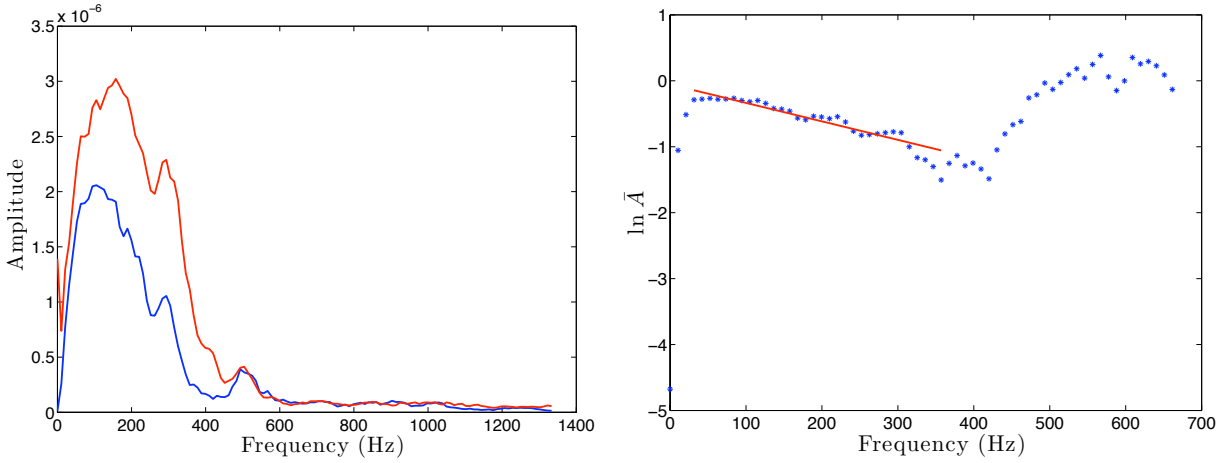

(a) (b)

Figure 3.3. (a) Amplitude spectra of two P-wave arrivals excited by one of the shots in stage 3 and recorded by the shallowest (red curve) and deepest (blue curve) geophones. (b) The logarithmic spectral ratio of the amplitude spectra (blue stars) and the best-fit straight line (red) in the selected frequency band.

the signal. The amplitude spectra of P-waves excited by one of the perforation shots and recorded at two geophones are shown in Figure 3.3. The spectrum of the event with the longer raypath is shifted towards lower frequencies, which indicates the influence of attenuation.

The ray-theoretical frequency-domain amplitude of the P-wave propagating between the ith source and the jth receiver in a homogeneous, anisotropic, attenuative medium can be written as

$$|A_{ij}| = S_i(\omega)\, \mathcal{G}_{ij}\, e^{-k^I_{ij}\, x_{ij}}, \tag{3.1}$$

where $S_i(\omega)$ represents the source spectrum and $\mathcal{G}_{ij}$ (assumed to be frequency-independent) incorporates the geometrical spreading and transmission coefficients along the raypath and the source/receiver directivity function. The coefficient k^I_{ij} is the imaginary part of the P-wave *group* wavenumber along the raypath for the source-receiver pair ij, and x_{ij} is the raypath length. According to the results of Behura and Tsvankin (2009c), equation 3.1 can be rewritten in terms of the normalized *phase* attenuation coefficient $\mathcal{A}_{ij}$ in the following

way:

$$|A_{ij}| = S_i(\omega)\, \mathcal{G}_{ij}\, e^{-\omega\, \mathcal{A}_{ij}\, t_{ij}}, \tag{3.2}$$

where ω is the angular frequency and t_{ij} is the traveltime. The coefficient $\mathcal{A}_{ij}$ should be obtained for the phase direction corresponding to the source-receiver line.

Since the perforation shots were not timed, the times picked on the shot gathers (e.g., in Figure 3.2) do not correspond to the actual traveltimes t_{ij} between the sources and receivers. Grechka and Duchkov (2011) estimate the origin times of the perforation shots by building homogeneous anisotropic velocity models. However, they show that the origin times can be obtained with reasonable accuracy for a homogeneous isotropic medium. Hence, we estimate the velocity of the direct P-waves from the slope of the vertical moveout observed in the receiver array under the assumption that the medium is isotropic and homogeneous (see Figure 3.2).

The logarithmic spectral ratio for two P-wave arrivals excited by the ith source and recorded by receivers j and k has the form:

$$\ln \bar{A} = \ln \left| \frac{A_{ij}}{A_{ik}} \right| = \ln \mathcal{G} - \omega\, s_{ijk}, \tag{3.3}$$

$$s_{ijk} = \mathcal{A}_{ij}\, t_{ij} - \mathcal{A}_{ik}\, t_{ik}, \tag{3.4}$$

where $\mathcal{G} = \mathcal{G}_{ij}/\mathcal{G}_{ik}$ is assumed to be frequency-independent. Note that the source spectrum in equation 3.3 is eliminated. Hence, the slope of the logarithmic spectral ratio for two source-receiver pairs yields the quantity s_{ijk}, which depends on the corresponding phase attenuation coefficients.

The spectral ratio computed for the two amplitude spectra from Figure 3.3a is displayed in Figure 3.3b. The bandwidth used in the spectral-ratio method has to be chosen in a frequency range where the signal-to-noise ratio is sufficiently high (e.g., $30 - 350$ Hz in Figure 3.3a). To obtain a robust estimate of s_{ijk}, we employ the iteratively reweighted least-squares method (Scales and Gersztenkorn, 1988; Aster et al., 2005).

In homogeneous isotropic media, the attenuation coefficient $\mathcal{A}$ is constant for all source-receiver pairs. If the medium is anisotropic, the coefficient $\mathcal{A}$ varies with the orientation of

the source-receiver line. By treating all attenuation coefficients as independent quantities, we can set up a system of linear equations for each stage. For example, the third stage includes three shots and 10 receivers, and the system of linear equations that includes the results for all source-receiver pairs is

$$s_{ijk} = \mathcal{A}_{ij}\, t_{ij} - \mathcal{A}_{ik}\, t_{ik};\ 1 \le i \le 3,\ 1 \le j < k \le 10, \tag{3.5}$$

where, as before, the index i denotes the source, while j and k denote the receivers.

Linear system 3.5 is overdetermined (there are 135 equations for 30 unknowns), but ill-conditioned due to closely spaced receivers and small differences between the arrival times. Hence, the attenuation coefficient along each raypath cannot be resolved individually. Note that the above analysis assumes that the medium is homogeneous. In the presence of heterogeneity, the recovered attenuation coefficients represent effective quantities for each source-receiver pair.

To reduce the number of unknowns but still honor attenuation anisotropy, we express attenuation coefficients as functions of angle. Zhu and Tsvankin (2006, 2007) obtain approximate phase attenuation coefficients of P- and S-waves in homogeneous TI and orthorhombic media in terms of Thomsen-style attenuation-anisotropy parameters. Their expression for the P-wave phase attenuation coefficient in orthorhombic media with the symmetry planes aligned with the Cartesian coordinate planes is

$$\mathcal{A}_P(\theta,\phi) = \mathcal{A}_{P0}[1 + \delta_{_Q}(\phi)\, \sin^2\theta \cos^2\theta + \epsilon_{_Q}(\phi) \sin^4\theta], \tag{3.6}$$

where $\mathcal{A}_{P0}$ is the vertical attenuation coefficient, θ is the polar angle, ϕ is the azimuth with respect to the x_1-axis, and

$$\delta_{_Q}(\phi) = \delta_{_Q}^{(1)} \sin^2\phi + \delta_{_Q}^{(2)} \cos^2\phi, \tag{3.7}$$

$$\epsilon_{_Q}(\phi) = \epsilon_{_Q}^{(1)} \sin^4\phi + \epsilon_{_Q}^{(2)} \cos^4\phi + (2\epsilon_{_Q}^{(2)} + \delta_{_Q}^{(3)}) \sin^2\phi \cos^2\phi. \tag{3.8}$$

The attenuation-anisotropy parameters $\delta_{_Q}^{(1,2,3)}$ and $\epsilon_{_Q}^{(1,2)}$ are defined in Zhu and Tsvankin (2007).

Since equations 3.6–3.8 are derived in the linearized weak-anisotropy approximation, the phase angle can be replaced with the group angle of the source-receiver direction (see Figure 3.1b). However, due to the limited angular coverage and absence of near-vertical raypaths, the attenuation-anisotropy parameters cannot be resolved with sufficient accuracy. Therefore, we represent $\mathcal{A}_{ij}$ by a second-order polynomial of the polar (θ_{ij}) and azimuthal (ϕ_{ij}) angles of the corresponding source-receiver direction (Figure 3.1b):

$$\mathcal{A}_{ij} = A + B\,\tilde{\theta}_{ij} + C\,\tilde{\theta}_{ij}^2 + D\,\tilde{\phi}_{ij} + E\,\tilde{\phi}_{ij}^2 + F\,\tilde{\theta}_{ij}\,\tilde{\phi}_{ij}, \tag{3.9}$$

$$\tilde{\theta}_{ij} = \theta_{ij} - \theta_c,\ \tilde{\phi}_{ij} = \phi_{ij} - \phi_c, \tag{3.10}$$

where the mean values of the polar and azimuthal angles for a given stage (corresponding to the "central ray") are denoted by θ_c and ϕ_c, respectively. Substituting equation 3.9 into equation 3.5, we obtain the following system of linear equations:

$$\begin{aligned} s_{ijk} &= A\,(t_{ij} - t_{ik}) + B\,(t_{ij}\,\tilde{\theta}_{ij} - t_{ik}\,\tilde{\theta}_{ik}) + C\,(t_{ij}\,\tilde{\theta}_{ij}^2 - t_{ik}\,\tilde{\theta}_{ik}^2) + D\,(t_{ij}\,\tilde{\phi}_{ij} - t_{ik}\,\tilde{\phi}_{ik}) \\ &+ E\,(t_{ij}\,\tilde{\phi}_{ij}^2 - t_{ik}\,\tilde{\phi}_{ik}^2) + F\,(t_{ij}\,\tilde{\theta}_{ij}\,\tilde{\phi}_{ij} - t_{ik}\,\tilde{\theta}_{ik}\,\tilde{\phi}_{ik}). \end{aligned} \tag{3.11}$$

System of equations 3.11 can be represented in matrix form,

$$\mathbf{S} = \mathbf{G}\mathbf{m}, \tag{3.12}$$

$$\mathbf{m} = [A\ B\ C\ D\ E\ F]^{\mathrm{T}}, \tag{3.13}$$

where $\mathbf{S}$ is the vector formed by the elements s_{ijk} and $\mathbf{G}$ is the matrix formed by the terms multiplied with elements of $\mathbf{m}$. The vector $\mathbf{m}$, which quantifies attenuation anisotropy, is estimated for each stage separately. Note that $\mathbf{m}$ could vary from stage to stage due to hydraulic stimulation and the fact that source-receiver raypaths for each stage probe different volumes of rock.

Table 3.1. Inverted elements of the model vector and their standard deviations for all stages. The dashes indicate the coefficients rejected by the best-subset regression.

	A $\times 10^{-3}$	B $\times 10^{-3}$	C $\times 10^{-3}$	D $\times 10^{-3}$	E $\times 10^{-3}$	F $\times 10^{-3}$
Stage 3	26.7 ± 2.0	–	-117.6 ± 21.9	-40.8 ± 8.6	–	49.4 ± 13.9
Stage 4	24.2 ± 1.2	–	-72.0 ± 14.4	-20.8 ± 4.4	–	24.9 ± 7.1
Stage 5	22.1 ± 1.6	–	–	-21.6 ± 6.7	–	27.5 ± 10.2
Stage 6	7.3 ± 0.9	–	-106.2 ± 14.9	–	–	163.6 ± 25.7
Stage 7	15.8 ± 0.7	–	107.5 ± 15.9	40.7 ± 21.5	–	-354.9 ± 60.8

By expressing the attenuation coefficient as a polynomial function of angle, the number of unknown parameters for each stage reduces to six. The vector $\mathbf{m}$ is found as the least-squares solution that minimizes the data misfit,

$$\psi = ||\mathbf{Gm} - \mathbf{S}||^2. \tag{3.14}$$

Because not all elements of $\mathbf{m}$ are well constrained by the data, we perform best-subset regression (Draper and Smith, 1981). We consider models with all possible combinations of the elements of $\mathbf{m}$ (equation 3.13), and compute the root-mean-square (rms) error and the p-values for the coefficients from Student's t-distribution. The p-value is a measure of the probability that the estimated coefficient is zero. We reject models with coefficients whose p-values are greater than 0.10 and select the model with the least value of the rms error as the solution. Assuming isotropic (angle-independent) attenuation results in a higher rms error, so taking anisotropy into account is essential to fit the data.

3.3 Inversion results

The best-fit inverted coefficients and their standard deviations are listed in Table 3.1. Directional dependence of attenuation is non-negligible, with polar anisotropy more pronounced than azimuthal anisotropy. The only exception is stage 5, which exhibits relatively weak attenuation anisotropy. The attenuation coefficient for stage 6 is substantially lower than that for the other stages, most likely due to the influence of heterogeneity and/or

Table 3.2. Sensitivity of the inversion results to errors in the origin times. The standard deviations are computed by contaminating the origin times with 100 realizations of Gaussian noise that has a standard deviation of 20 time samples.

	A $\times 10^{-3}$	B $\times 10^{-3}$	C $\times 10^{-3}$	D $\times 10^{-3}$	E $\times 10^{-3}$	F $\times 10^{-3}$
Stage 3	26.5 ± 0.6	–	-116.4 ± 6.0	-40.0 ± 3.0	–	49.6 ± 6.7
Stage 4	24.1 ± 0.3	–	-70.2 ± 2.7	-20.3 ± 1.2	–	24.3 ± 2.6
Stage 5	22.0 ± 0.2	–	–	-21.5 ± 1.3	–	28.0 ± 2.6
Stage 6	7.3 ± 0.1	–	-106.2 ± 3.6	–	–	163.7 ± 6.1
Stage 7	15.8 ± 0.1	–	107.7 ± 2.7	40.7 ± 0.9	–	-355.3 ± 9.8

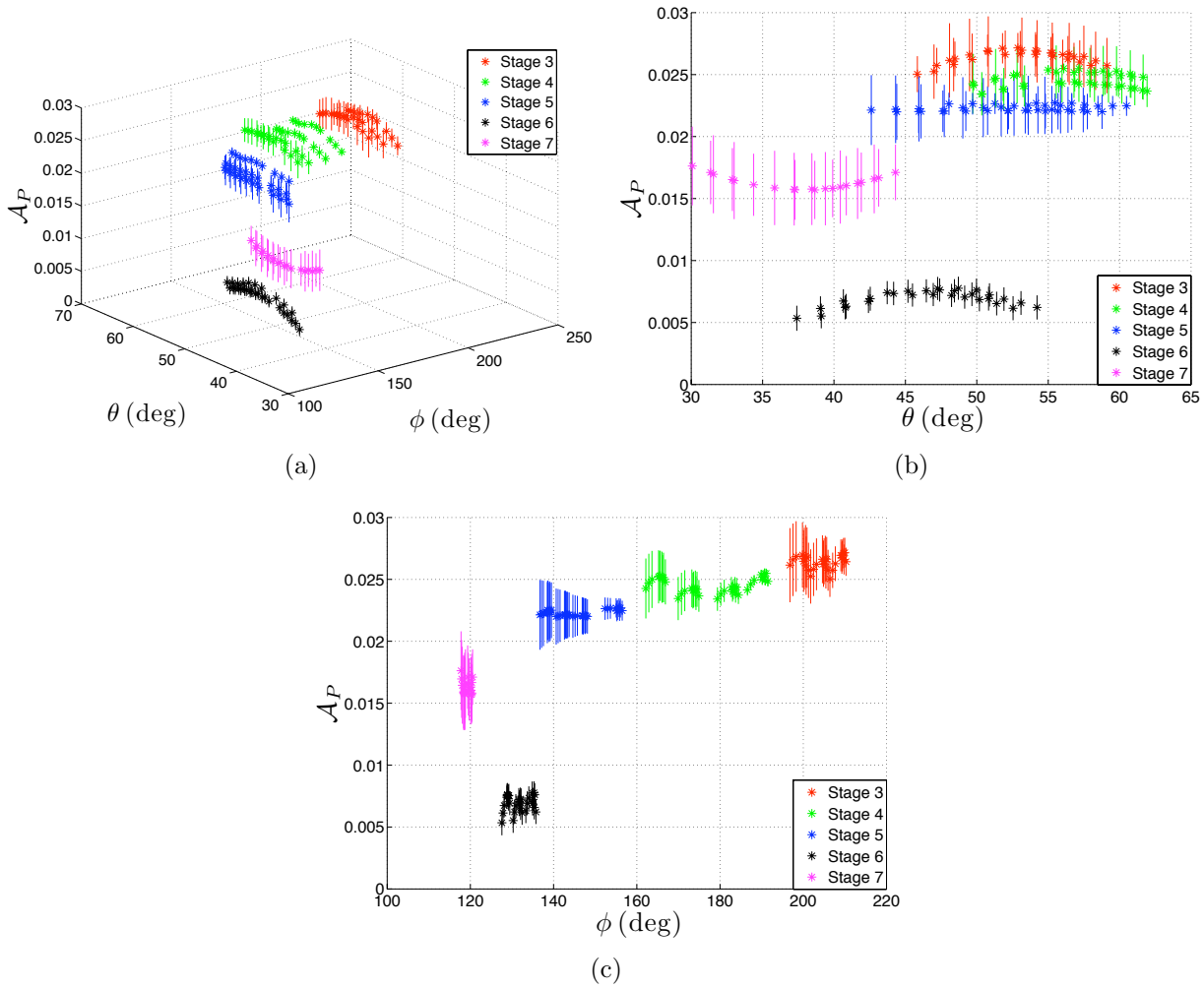

Figure 3.4. (a) P-wave attenuation coefficient (stars of different color) for all source-receiver pairs in spherical coordinates. (b) Variation of $\mathcal{A}_P$ with the polar angle obtained as the projection of plot (a) onto the $[\mathcal{A}_P, \theta]$-plane. (c) Variation of $\mathcal{A}_P$ with the azimuthal angle.

measurement errors.

The analytic attenuation coefficient in equation 6 can be expanded in a Taylor series around the mean values of the polar (θ) and azimuthal (ϕ) angles for each stage. If the orientation of the symmetry planes is known, the six polynomial coefficients in equation 3.7 can be used to uniquely determine all six Thomsen-style parameters. However, due to the trade-offs between the coefficients of the polynomial, the attenuation-anisotropy parameters cannot be resolved individually. Physically, the range of the polar and azimuthal angles in the experiment is too narrow to constrain $\mathcal{A}_{P0}$, $\delta_Q^{(1,2,3)}$, and $\epsilon_Q^{(1,2)}$.

It is essential to evaluate the sensitivity of the inversion results to uncertainties in the origin times. We added 100 realizations of Gaussian noise with a standard deviation of 20 time samples to the origin times and estimated the coefficients in equation 9 for each of these realizations. The mean values and standard deviations of the elements of the vector $\mathbf{m}$ are listed in Table 3.2. Clearly, the inversion results are weakly influenced by errors in the origin times. In fact, comparison of Tables 3.1 and 3.2 shows that the inverted attenuation coefficient is more sensitive to noise in the spectral-ratio estimates.

The mean values and standard deviations of the attenuation coefficients $\mathcal{A}_P$ for all source-receiver pairs are shown in spherical coordinates in Figure 3.4. The mean value of the attenuation coefficient decreases with the stage number. This variation in attenuation is likely related to the changes in the medium due to hydraulic fracturing and pumping of fluids through the rock volume.

3.4 Conclusions

We introduced a methodology for estimating the directionally dependent P-wave attenuation coefficient from cross-hole data acquired for a relatively narrow range of propagation directions. A string of receivers in a vertical borehole was used to record the wavefield excited by perforation shots set off in a horizontal hole to induce hydraulic fracturing. The attenuation coefficient was represented as a quadratic polynomial of the polar and azimuthal angles, and the polynomial coefficients were estimated by applying the spectral-ratio method

to pairs of traces. The data for each stage of perforation shots were processed separately, with the attenuation coefficient expanded around the corresponding "central ray." The inversion results show that taking anisotropy into account substantially improves fitting of the attenuation measurements. The angular variation of the attenuation coefficient is more pronounced in the vertical plane, so polar attenuation anisotropy is stronger than azimuthal anisotropy.

The mean value of the attenuation coefficient decreases with successive stages of hydraulic fracturing and stimulation. This could be due to the diffusion of stimulant fluids in the induced fractures, which stiffens the medium and makes it less attenuative. Microseismic monitoring can delineate the extent of the zones of fluid diffusion, which should help verify this hypothesis. Because the reservoir formation is made up mostly of shale, it is likely to exhibit intrinsic attenuation anisotropy, whose contribution may complicate analysis of the attenuation signature of hydraulic fracturing.

3.5 Acknowledgments

We thank Shell E&P Company and EnCana for providing the data. We are grateful to Vladimir Grechka (Shell), Serge Shapiro (Free University of Berlin), and the members of the A(nisotropy)-Team of the Center for Wave Phenomena (CWP), Colorado School of Mines, for fruitful discussions.

Chapter 4

POINT-SOURCE RADIATION IN ATTENUATIVE ANISOTROPIC MEDIA

Important insights into point-source radiation in attenuative anisotropic media can be gained by applying asymptotic methods. Here, we derive the asymptotic Green's function in homogeneous, attenuative, arbitrarily anisotropic media using the steepest-descent method. The saddle-point condition helps describe the behavior of the slowness and group-velocity vectors of the P-, S_1-, and S_2-waves in the far field. We test the accuracy of the asymptotic analysis by comparing it with the ray-perturbation method for P-waves in transversely isotropic media.

4.1 Introduction

Velocity and attenuation anisotropy significantly influence the radiation pattern of seismic waves excited by a point source. A proper correction for the source directivity can help improve the robustness of AVO (amplitude variation with offset) and attenuation analysis. Point-source radiation in homogeneous anisotropic media has been mostly studied for nonattenuative materials using both asymptotic and numerical methods (e.g. Červený, 2001; Tsvankin and Chesnokov, 1990 a; Gajewski 1993; Wang and Achenbach, 1994). Zhu (2006) presents an analytic and numerical study of point-source radiation in 2D homogeneous attenuative transversely isotropic (TI) media. Vavryčuk (2007) derives the asymptotic Green's function for arbitrarily anisotropic, homogeneous, attenuative media by formally extending the results of Wang and Achenbach (1994) obtained for elastic media.

In attenuative media, the Christoffel matrix becomes complex-valued because the stiffnesses acqure an imaginary part (Borcherdt, 2009; Carcione, 2007). Although many results derived for elastic models can be generalized for attenuative media, there are several impor-

tant differences. In particular, the saddle-point condition involves complex-valued slowness and group-velocity vectors whose real and imaginary parts can have different directions; hence, the properties of these vectors have to be clearly defined. Here, we present a rigorous derivation of the saddle-point condition and the Green's function in attenuative anisotropic media.

We start by reviewing the definitions of the attenuation coefficient, group velocity, and other key signatures in attenuative media. Then the integral expression for the Green's function in homogeneous attenuative anisotropic media is evaluated by the steepest-descent method. The saddle-point condition is used to study the influence of attenuation on the properties of the far-field P-wave. Finally, we compare the P-wave group-velocity, polarization, and slowness vectors obtained from our asymptotic analysis for TI media with those found from ray perturbation theory (Červený and Pšenčik, 2009).

4.2 Basic Definitions

In attenuative media the density-normalized stiffness tensor $\tilde{a}_{ijkl}$ is complex-valued (complex quantities are denoted by the tilde sign on top):

$$\tilde{a}_{ijkl} = a^R_{ijkl} - i\, a^I_{ijkl}, \tag{4.1}$$

and the wave vector defined for plane waves is given by

$$\tilde{\mathbf{k}} = \mathbf{k}^R + i\, \mathbf{k}^I\,, \tag{4.2}$$

where $\mathbf{k}^R$ and $\mathbf{k}^I$ represent the real and imaginary parts of the wave vector, respectively. The slowness vector $\tilde{\mathbf{p}} = \tilde{\mathbf{k}}/\omega = \mathbf{p}^R + i\,\mathbf{p}^I$ consists of the real-valued propagation ($\mathbf{p}^R$) and attenuation ($\mathbf{p}^I$) vectors. The orientations of $\mathbf{p}^R$ and $\mathbf{p}^I$ can be different, and the angle between $\mathbf{p}^R$ and $\mathbf{p}^I$ is called the "inhomogeneity (or attenuation) angle" ξ (Červený and Pšenčik, 2005; Behura and Tsvankin, 2009c; Tsvankin and Grechka, 2011). Plane waves can satisfy the wave equation for a range of values of ξ, except for those corresponding to certain "forbidden directions" of $\mathbf{p}^I$ (Krebes and Le, 1994; Červený and Pšenčik, 2005; Carcione, 2007).

For waves excited by point sources, however, the inhomogeneity angle is determined by medium properties and boundary conditions (Vavryčuk, 2007; Zhu, 2006). In reflection/transmission problems for plane waves, the inhomogeneity angle for reflected and transmitted modes is constrained by Snell's law (Hearn and Krebes, 1990; Behura and Tsvankin, 2009c).

Zhu and Tsvankin (2006) define the phase attenuation coefficient $\mathcal{A}$ as

$$\mathcal{A} = \frac{|\mathbf{k}^I|}{|\mathbf{k}^R|}\,. \tag{4.3}$$

The angle-dependent quality factor Q is related to $\mathcal{A}$ by

$$Q = \frac{1}{2\mathcal{A}}\,. \tag{4.4}$$

Červený and Pšenčik (2008) show that the group attenuation coefficient responsible for attenuation-related amplitude decay along seismic rays can be written as:

$$\mathcal{A}^{\mathrm{gr}} = \frac{\mathbf{p}^I \cdot \mathbf{F}^R}{\mathbf{p}^R \cdot \mathbf{F}^R}, \tag{4.5}$$

where $\mathbf{F}^R$ denotes the real part of the Poynting vector. The real part of the complex-valued Poynting vector is parallel to the group-velocity vector. The time-averaged energy flux is given by:

$$F_i^R = \kappa\,\mathrm{Re}\big[\tilde{a}_{ijkl}\,\tilde{p}_l\,\tilde{g}_j^*\,\tilde{g}_k\big], \tag{4.6}$$

where the asterisk denotes the complex conjugate, κ is a constant, and $\tilde{g}_j$ are the components of the complex-valued polarization vector $\tilde{\mathbf{g}}$ normalized using the condition $\tilde{\mathbf{g}} \cdot \tilde{\mathbf{g}} = 1$. Behura and Tsvankin (2009c) prove that the group attenuation coefficient is practically independent of the inhomogeneity angle and coincides with the phase attenuation coefficient for $\xi = 0$, except for the vicinity of the forbidden directions. Similar results follow from the perturbation analysis presented by Červený and Pšenčik (2008, 2009).

4.3 Asymptotic Green's function in homogeneous attenuative anisotropic media

Here, we derive the asymptotic Green's function in the frequency domain for a homogeneous, attenuative, arbitrarily anisotropic medium. The analysis is valid for all three wave

modes (P, S_1, S_2), but breaks down in the vicinity of shear-wave singularities where the Christoffel equation has equal or close eigenvalues. According to the causality principle, the stiffnesses in attenuative media should be, in general, frequency-dependent (Aki and Richards, 1980). Although we do not explicitly account for velocity dispersion, the following analysis is valid for a frequency-dependent stiffness tensor.

The exact Green's function can be found as the solution of the elastodynamic equation (Appendix A, equation A.9):

$$G_{kn}(\mathbf{x}, \mathbf{x}^0, \omega) = \frac{i\omega}{(2\pi)^2} \int_{-\infty}^{\infty} \int_{-\infty}^{\infty} \Big[\frac{\tilde{S}_{kn}}{\partial[\det(\tilde{\mathbf{\Gamma}} - \mathbf{I})]/\partial p_3} \Big]_{p_3 = \tilde{p}_3^r} e^{\omega R \, \tilde{\phi}} \, \mathrm{d}p_1 \, \mathrm{d}p_2 \,, \tag{4.7}$$

where the x_3-axis points in the source-receiver direction and

$$\tilde{\phi} = i \, \tilde{p}_3^r \,. \tag{4.8}$$

Here, R is the source-receiver distance, p_j are the slowness components, $\tilde{\Gamma}_{ik} = \tilde{a}_{ijkl} \, p_j \, p_l$, $\mathbf{I}$ is the identity matrix, $\tilde{S}_{kn}$ are the cofactors of the matrix $\tilde{\mathbf{\Gamma}} - \mathbf{I}$, and $\tilde{p}_3^r = \tilde{p}_3(p_1, \, p_2)$ is one of the solutions of the complex-valued equation $\det \left[\tilde{a}_{ijkl} \, p_j \, p_l - \delta_{ik} \right] = 0$.

If we assume that $\omega R / v \gg 1$ (v is the average of the group velocity over all angles), G_{kn} (equation 4.7) can be evaluated by iterated application of the steepest-descent method (Bleistein, 2012). The saddle-point condition satisfied at $[\tilde{p}_1^s, \, \tilde{p}_2^s]$ is

$$\frac{\partial \tilde{\phi}}{\partial p_1} = \frac{\partial \tilde{\phi}}{\partial p_2} = 0 \,. \tag{4.9}$$

Equation 4.7 can now be evaluated by iteratively applying the steepest-descent method (Bleistein, 2012), which yields:

$$G_{kn}(\mathbf{x}, \mathbf{x}^0, \omega) = \frac{1}{2\pi R} \, \frac{1}{\sqrt{|\det \tilde{\mathbf{\Phi}}''|}} \, \frac{\tilde{S}_{kn}}{\partial[\det(\tilde{\mathbf{\Gamma}} - \mathbf{I})]/\partial p_3} \, \exp \Big(i \, \omega \, R \, \tilde{p}_3^r - \frac{i}{2} \arg \left[\det \tilde{\mathbf{\Phi}}'' \right] \Big) \,, \tag{4.10}$$

where $\tilde{\mathbf{\Phi}}''$ is the Hessian matrix of the second-order partial derivatives of $\tilde{\phi}$ with respect to p_1 and p_2; all quantities are obtained at the saddle point.

We now discuss the identification of the saddle point $[\tilde{p}_1^s, \, \tilde{p}_2^s]$. Equation 4.9 implies:

$$\Big[\frac{\partial \tilde{p}_3(p_1, p_2)}{\partial p_1} \Big]_{\tilde{p}_1^s, \tilde{p}_2^s} = 0 \,, \tag{4.11}$$

$$\Big[\frac{\partial \tilde{p}_3(p_1,p_2)}{\partial p_2}\Big]_{\tilde{p}_1^s,\tilde{p}_2^s} = 0\,. \tag{4.12}$$

Each eigenvalue of the Christoffel matrix $\tilde{\lambda}^{(m)}$ is a function of the slowness vector (with $\tilde{p}_3 = \tilde{p}_3^r$) (see Appendix B, equation B.9):

$$\tilde{\lambda}^{(m)} = \lambda(\tilde{a}_{ijkl}, \tilde{p}_j) = \tilde{a}_{ijkl}\,\tilde{p}_j\,\tilde{p}_l\,\tilde{g}_i^{(m)}\,\tilde{g}_k^{(m)}, \tag{4.13}$$

where m takes values from 1 to 3 and $\tilde{\mathbf{g}}^{(m)}$ denotes the corresponding unit polarization vector introduced in Appendix B. The eigenvalue $\tilde{\lambda}^{(1)} = 1$, if the slowness vector corresponds to the fastest mode (P-wave). The partial derivatives in equations 4.11 and 4.12 can be calculated from the function $\lambda(\tilde{a}_{ijkl}, \tilde{p}_j)$ (equation 4.13) using the analytic implicit function theorem (Krantz and Parks, 2002):

$$\Big[\frac{\partial \tilde{p}_3(p_1,p_2)}{\partial p_1}\Big]_{\tilde{p}_1^s,\tilde{p}_2^s} = \Big[\frac{\partial\lambda/\partial p_1}{\partial\lambda/\partial p_3}\Big]_{\tilde{p}_1^s,\tilde{p}_2^s}, \tag{4.14}$$

$$\Big[\frac{\partial \tilde{p}_3(p_1,p_2)}{\partial p_2}\Big]_{\tilde{p}_1^s,\tilde{p}_2^s} = \Big[\frac{\partial\lambda/\partial p_2}{\partial\lambda/\partial p_3}\Big]_{\tilde{p}_1^s,\tilde{p}_2^s}, \tag{4.15}$$

where $\partial\lambda/\partial p_j$ is given by equation B.10 and $\partial\lambda/\partial p_3 \neq 0$ because the x_3-axis points in the source-receiver direction. Next, we introduce the "energy velocity" vector $\tilde{\mathcal{U}}$ (Vavryčuk, 2007) as

$$\tilde{\mathcal{U}}_j = \frac{1}{2}\,\frac{\partial\lambda}{\partial p_j}. \tag{4.16}$$

Equations 4.14 and 4.15 imply that at the saddle point,

$$\tilde{\mathcal{U}}_1 = \tilde{\mathcal{U}}_2 = 0. \tag{4.17}$$

Hence, the real and imaginary parts of $\tilde{\mathcal{U}}$ are parallel to the vector connecting the source and receiver (i.e., to the x_3-axis). Note that Červený et al. (2008) arrived at the same conclusion using perturbation analysis. Equations 4.16 and 4.17 can be used to constrain the slowness vector $\tilde{\mathbf{p}}$ that corresponds to the plane wave that makes the most significant contribution to

the wavefield at the receiver location. It is convenient to parametrize $\tilde{\mathbf{p}}$ in the following way (Červený and Pšenčik, 2005):

$$\tilde{\mathbf{p}} = \tilde{\sigma}\,\mathbf{n} + i\,D\,\mathbf{m}, \tag{4.18}$$

where $\tilde{\sigma}$ is a complex-valued quantity whose magnitude is close to the slowness vector with a zero inhomogeneity angle, the vector $\mathbf{n}$ specifies the phase direction, $\mathbf{m}$ is chosen to be perpendicular to $\mathbf{n}$ (i.e., $\mathbf{n} \cdot \mathbf{m} = 0$), and D is called the inhomogeneity parameter (Červený and Pšenčik, 2005). It should be emphasized that for plane waves, the parameters $\tilde{\sigma}$ and D can vary within a certain range for fixed vectors $\mathbf{n}$ and $\mathbf{m}$. Equivalently, plane waves can satisfy the wave equation with arbitrary values of the inhomogeneity angle, except for those corresponding to certain "forbidden directions." To find the parameters $\tilde{\sigma}$ and D corresponding to the saddle point, we solve the following constrained optimization problem:

$$\text{Minimize } \tilde{\mathcal{U}}_1^2 + \tilde{\mathcal{U}}_2^2, \quad \text{subject to } \tilde{\lambda}^{(1)} = 1. \tag{4.19}$$

This problem is nonlinear, and the values of $\tilde{\sigma}$ and D at the global minimum yield the slowness vector at the saddle point.

Equation 4.10 can be simplified once the saddle point has been identified. From equations 4.17 and B.12, we have:

$$\tilde{p}_3\,\tilde{\mathcal{U}}_3 = \tilde{\lambda}^{(1)} = 1. \tag{4.20}$$

The phase function at the saddle point (equation 4.8) can therefore be written as

$$\tilde{\phi} = i\tilde{p}_3^r = i\frac{1}{\tilde{\mathcal{U}}_3}. \tag{4.21}$$

In elastic media, equation 4.16 defines the components of the group-velocity vector. In attenuative media, the real and imaginary parts of $\tilde{\mathcal{U}}$ determine the traveltime and energy dissipation, respectively. Using equations B.16 and 4.16, we have:

$$\frac{\tilde{S}_{kn}}{\partial[\det(\tilde{\mathbf{\Gamma}} - \mathbf{I})]/\partial p_3} = \frac{\tilde{S}_{kn}}{\tilde{S}_{ij}\,\partial\tilde{\Gamma}_{ij}/\partial p_3} = \frac{\tilde{g}_k^{(1)}\,\tilde{g}_n^{(1)}}{2\tilde{\mathcal{U}}_3}, \tag{4.22}$$

Equation 4.10 can then be rewritten as:

$$G_{kn}(\mathbf{x},\mathbf{x}^0,\omega) = \frac{\tilde{g}_k^{(1)}\,\tilde{g}_n^{(1)}}{4\pi\,R\tilde{\mathcal{U}}_3\sqrt{|\det\tilde{\mathbf{\Phi}}''|}}\,\exp\left(i\,\frac{\omega\,R}{\tilde{\mathcal{U}}_3}-\frac{i}{2}\arg\left[\det\tilde{\mathbf{\Phi}}''\right]\right), \tag{4.23}$$

where the components of the matrix $\tilde{\mathbf{\Phi}}''$ are computed at the saddle point using the implicit function theorem:

$$\tilde{\Phi}''_{MN} = -\Big[\frac{\partial^2\lambda/\partial p_M\partial p_N}{\partial\lambda/\partial p_3}\Big]_{\tilde{p}_1^s,\tilde{p}_2^s}; \tag{4.24}$$

the indices M and N take values from 1 to 2. The second-order partial derivatives of $\lambda(\tilde{a}_{ijkl},\tilde{p}_j)$ can be evaluated using equation B.11.

Equation 4.23 was derived for a rotated coordinate frame with the x_3-axis pointing in the source-receiver direction. The Green's function in a general (global) Cartesian coordinate frame takes the following form:

$$G_{kn}(\mathbf{x},\mathbf{x}^0,\omega) = \frac{\tilde{g}_k^{(1)}\,\tilde{g}_n^{(1)}}{4\pi\,R\,|\tilde{\mathcal{U}}|\sqrt{|\det\tilde{\mathbf{\Phi}}''|}}\,\exp\left(i\,\frac{\omega\,R}{\tilde{\mathcal{U}}}-\frac{i}{2}\arg\left[\det\tilde{\mathbf{\Phi}}''\right]-i\arg\left[\tilde{\mathcal{U}}\right]\right), \tag{4.25}$$

where $\tilde{\mathcal{U}}$ denotes the group-velocity vector in the source-receiver direction.

For TI media, equation 4.25 reduces to the expression for the Green's function derived by Zhu (2006). Although the asymptotic analysis carried out above is similar to that presented by Vavryčuk (2007), we proved (rather than assumed) that at the saddle point the real and imaginary parts of the "energy-velocity" vector are parallel to each other.

4.4 Ray perturbation analysis for anisotropic attenuative media

Here, we briefly review the ray-tracing methodology of Červený and Pšenčik (2009), which is applicable in attenuative, anisotropic, heterogeneous media with smooth spatial variations of the stiffness tensor. We provide expressions for the ray-theoretical Green's function and analyze the orientation of the slowness vector in homogeneous attenuative models. These results will be compared to those obtained in the previous section.

Following Klimeš (2002), Červený and Pšenčik (2009) treat the traveltime as a complex-valued quantity, with the real part contributing to the phase and the imaginary part to

the dissipation along the ray. The traveltime and its spatial gradients are computed as perturbations of the corresponding real-valued quantities obtained along the ray traced in the reference elastic medium. In the density-normalized stiffness tensor given by equation 4.1, here we treat the real part a^R_{ijkl} as corresponding to the reference elastic medium, and the imaginary part a^I_{ijkl} is the attenuation-related perturbation.

We consider the linear perturbation Hamiltonian $\mathcal{H}(\alpha)$ defined in Červený and Pšenčik (2009):

$$\mathcal{H}(\alpha) = \mathcal{H}^0 + \alpha \triangle\mathcal{H}, \tag{4.26}$$

with

$$\triangle\mathcal{H} = \tilde{\mathcal{H}} - \mathcal{H}^0, \tag{4.27}$$

where $\mathcal{H}^0$ and $\tilde{\mathcal{H}}$ are the Hamiltonians corresponding to the (elastic) reference and (viscoelastic) perturbed medium, respectively. The perturbation parameter is denoted by α; $\alpha = 0$ corresponds to reference elastic medium and $\alpha = 1$ to the perturbed attenuative medium. The reference Hamiltonian $\mathcal{H}^0$ can be expressed through the real-valued slowness ($\mathbf{p}^0$) and polarization ($\mathbf{g}^0$) vectors computed for the reference elastic medium:

$$\mathcal{H}^0 = \frac{1}{N}\left[a^R_{ijkl}\, p^0_j\, p^0_l\, g^0_i\, g^0_k\right]^{N/2}, \tag{4.28}$$

where N is an integer. The perturbed Hamiltonian $\tilde{\mathcal{H}}$ is given by

$$\tilde{\mathcal{H}} = \frac{1}{N}\left[\tilde{a}_{ijkl}\, p^0_j\, p^0_l\, \tilde{g}_i\, \tilde{g}_k\right]^{N/2}, \tag{4.29}$$

where the complex polarization vector $\tilde{\mathbf{g}}$ is computed from the complex Christoffel matrix $\tilde{\Gamma}_{ik} = \tilde{a}_{ijkl}\, p^0_j\, p^0_l$ using equation B.8.

The traveltime and its spatial gradients can be expanded into a perturbation series in terms of the parameter α:

$$\tau(\alpha) \approx \tau^0 + \alpha\, \frac{\partial\tau}{\partial\alpha} + \cdots, \tag{4.30}$$

$$\frac{\partial\tau}{\partial x_i} \approx \frac{\partial\tau^0}{\partial x_i} + \alpha \left[\frac{\partial^2\tau}{\partial x_i\, \partial\alpha}\right]_{\alpha=0} + \cdots, \tag{4.31}$$

where all terms correspond to the reference medium. The second-order partial derivatives in equation 4.31 can be computed using dynamic ray tracing (Červený and Pšenčik, 2009). The first-order approximation for the traveltime and the traveltime gradients in attenuative media can be obtained by substituting $\alpha = 1$ and retaining the first two terms of the expansion in equations 4.30 and 4.31. The real part of the traveltime contributes to the phase (i.e., it is the traveltime correction) and the imaginary part is responsible for the amplitude decay along the ray. The real part of the traveltime gradient corresponds to $\mathbf{p}^R$ and the imaginary part to $\mathbf{p}^I$:

$$p_i^R = \mathrm{Re}\left[\frac{\partial \tau}{\partial x_i}\right] \approx p_i^0 + \mathrm{Re}\left[\frac{\partial^2 \tau}{\partial x_i \, \partial \alpha}\right]_{\alpha=0}, \tag{4.32}$$

$$p_i^I = \mathrm{Im}\left[\frac{\partial \tau}{\partial x_i}\right] \approx \mathrm{Im}\left[\frac{\partial^2 \tau}{\partial x_i \, \partial \alpha}\right]_{\alpha=0}. \tag{4.33}$$

The inhomogeneity angle can be computed from

$$\cos \xi = \frac{\mathbf{p}^I \cdot \mathbf{p}^R}{|\mathbf{p}^I| \, |\mathbf{p}^R|}. \tag{4.34}$$

An approximate ray-theoretical Green's function in homogeneous weakly attenuative media can be found by substituting the complex-valued traveltime into the expression for the reference elastic model (see Pšenčik and Teles, 1996, equation 7):

$$G_{kn}(\mathbf{x}, \mathbf{x}^0, \omega) = \frac{g_k \, g_n}{4\pi R \, |\mathcal{U}| \, \sqrt{|K|}} \, \exp(i \, \omega \, \mathrm{Re}\,[\tilde{\tau}] + i \, \frac{\pi}{2} k_s) \, \exp(-\omega \, \mathrm{Im}\,[\tilde{\tau}]), \tag{4.35}$$

where $\mathbf{g}$ is the polarization vector, R is the source-receiver distance, $|\mathcal{U}|$ is the magnitude of group velocity, K is the Gaussian curvature of the slowness surface, and k_s quantifies the phase shift due to K. Except for the complex traveltime $\tilde{\tau}$, all quantities are computed for the reference elastic medium.

The group attenuation coefficient is given by:

$$\mathcal{A}_P = -\mathrm{Im}\, \tilde{\mathcal{H}}, \tag{4.36}$$

where $\tilde{\mathcal{H}}$ is defined in equation 4.29. Červený and Pšenčik (2009) also provide an approximation for the group-velocity components $\tilde{\mathcal{U}}_i$ in attenuative media:

$$\tilde{\mathcal{U}}_i = (1 - i\,\mathcal{A}_P)\,\mathcal{U}_i, \tag{4.37}$$

where $\mathcal{U}_i$ is computed in the reference elastic medium. Hence, in homogeneous, weakly attenuative media, $\tilde{\tau} \approx R/|\tilde{\mathcal{U}}|$, and equation 4.35 can be rewritten as

$$G_{kn}(\mathbf{x}, \mathbf{x}^0, \omega) = \frac{g_k\, g_n}{4\pi\, R\mathcal{U}\,\sqrt{|K|}}\, \exp\Big(i\,\omega\,\frac{R}{\tilde{\mathcal{U}}} + i\,\frac{\pi}{2} k_s\Big). \tag{4.38}$$

Note that the complex-valued group velocity obtained from the perturbation analysis appears only in the exponential function, whereas the polarization vector and the Gaussian curvature K of the slowness surface, which control the magnitude of the Green's function, are computed for the reference medium.

4.5 Numerical Examples

In this section, the analytic results presented above are used to study the Green's function and the behavior of the slowness vector in homogeneous, attenuative VTI media. Table 1 shows the parameters of the velocity and attenuation functions for four VTI models similar to those employed by Zhu (2006).

First, we compare the P-wave group attenuation coefficients obtained from the asymptotic analysis discussed above and perturbation theory. The "asymptotic" coefficient is computed from equation 4.5 with the slowness $\tilde{\mathbf{p}}$ and the corresponding Poynting vector $\mathbf{F}$ obtained from the asymptotic analysis. Equation 4.36 is used to find the attenuation coefficient from perturbation analysis with the Hamiltonians of degrees $N = -1$ and 2. The example in Figure 5.1 shows that the group quality factor Q (equation 4.4) obtained from the perturbation theory is close to the asymptotic value; also, the quality factors for the two choices of N coincide. Although the attenuation-anisotropy coefficients $\epsilon_{_Q}$ and $\delta_{_Q}$ for model 3 are equal to zero, there is a slight angular variation in Q caused by velocity anisotropy (Zhu and Tsvankin, 2006).

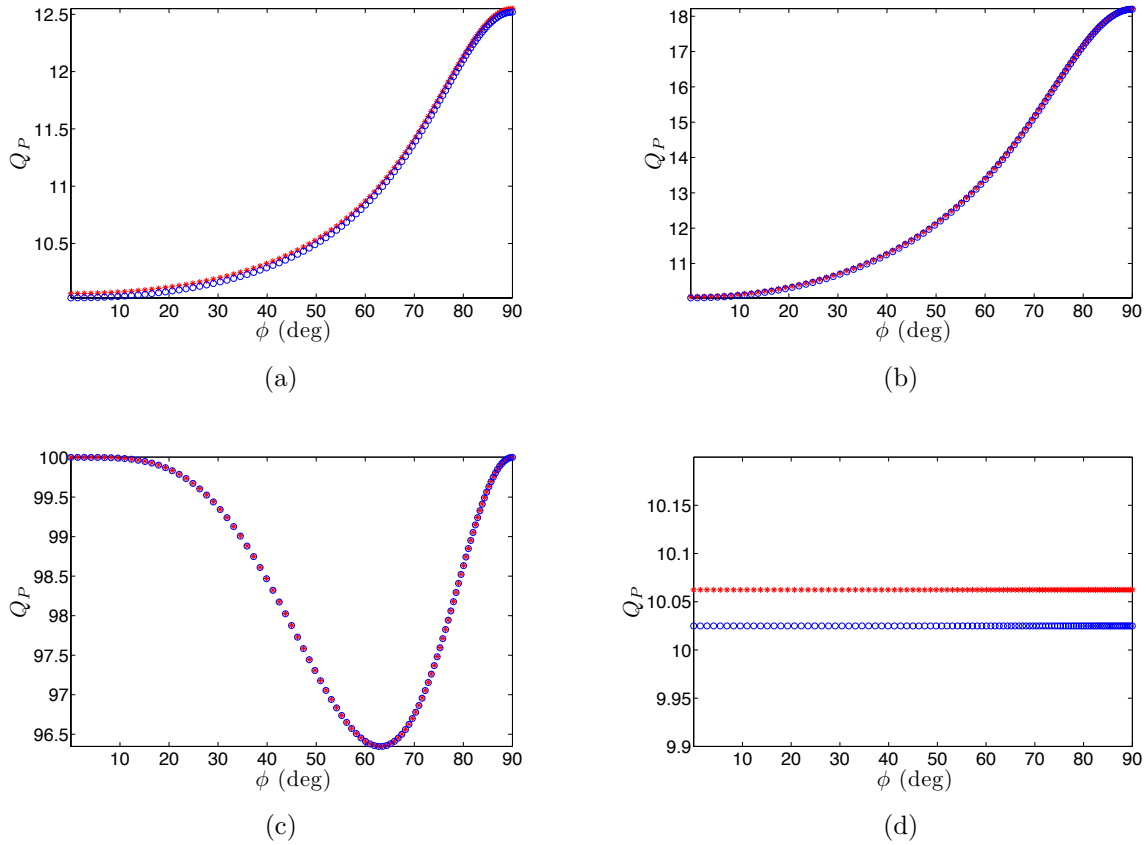

Figure 4.1. Comparison of the P-wave group quality factors as a function of the group angle ϕ with the vertical obtained from the asymptotic (blue circles) and perturbation (red stars) analysis for (a) model 1, (b) model 2, (c) model 3, and (d) model 4. The models are defined in Table 4.1.

Table 4.1. Homogeneous TI models with anisotropic velocity and attenuation functions. The parameters V_{P0} and V_{S0} are the P- and S-wave symmetry-direction velocities, Q_{P0} and Q_{S0} are the P-wave and S-wave symmetry-direction quality factors, and $\epsilon_{_Q}$ and $\delta_{_Q}$ are the attenuation-anisotropy parameters defined in Zhu and Tsvankin (2006) and Tsvankin and Grechka (2011).

Model	1	2	3	4
V_{P0} (km/s)	3.00	3.00	3.00	3.00
V_{S0} (km/s)	1.50	1.50	1.50	1.50
ϵ	0.10	0.40	0.40	0.40
δ	0.05	0.25	0.25	0.25
Q_{P0}	10	10	100	10
Q_{S0}	6	6	10	10
$\epsilon_{_Q}$	-0.20	-0.45	0	0
$\delta_{_Q}$	-0.10	-0.50	0	0

Substituting the slowness vector computed from the asymptotic analysis into the Christoffel matrix and using equation B.8 yields the plane-wave polarization vector that corresponds to the saddle-point condition. Similarly, substituting the slowness vector obtained by ray tracing in the reference medium into the Christoffel matrix yields the polarization vector in the perturbation analysis. We found that the asymptotic and perturbation approach produce the polarization vectors with close magnitudes. Figure 5.3 displays the phase of the vertical component of the polarization vector $\tilde{g}_3$ ($\arg \tilde{g}_3$) computed from asymptotic and perturbation methods for models 1 - 4. The function $\arg \tilde{g}_3$ monotonically increases with the group angle ϕ for models 1 - 3, while it is negligible for model 4 because the attenuation function is isotropic. Note that the magnitude of $\tilde{g}_3$ for angles approaching 90° (near the isotropy plane) is small, which distorts the phase of $\tilde{g}_3$. For all models, the asymptotic and perturbation methods yield similar values of $\arg \tilde{g}_3$, with some deviations only for large angles ϕ.

Next, we analyze the component G_{33} of the Green's function obtained from asymptotic analysis (equation 4.23):

$$G_{33}(\mathbf{x}, \mathbf{x}^0, \omega) = \frac{\tilde{g}_3^{(1)}\, \tilde{g}_3^{(1)}}{4\pi\, R\, |\tilde{\mathcal{U}}|\, \sqrt{|\det \tilde{\mathbf{\Phi}}''|}}\, \exp\left(i\, \frac{\omega\, R}{\tilde{\mathcal{U}}} - \frac{i}{2} \arg\left[\det \tilde{\mathbf{\Phi}}''\right] - i \arg\left[\tilde{\mathcal{U}}\right] \right). \qquad (4.39)$$

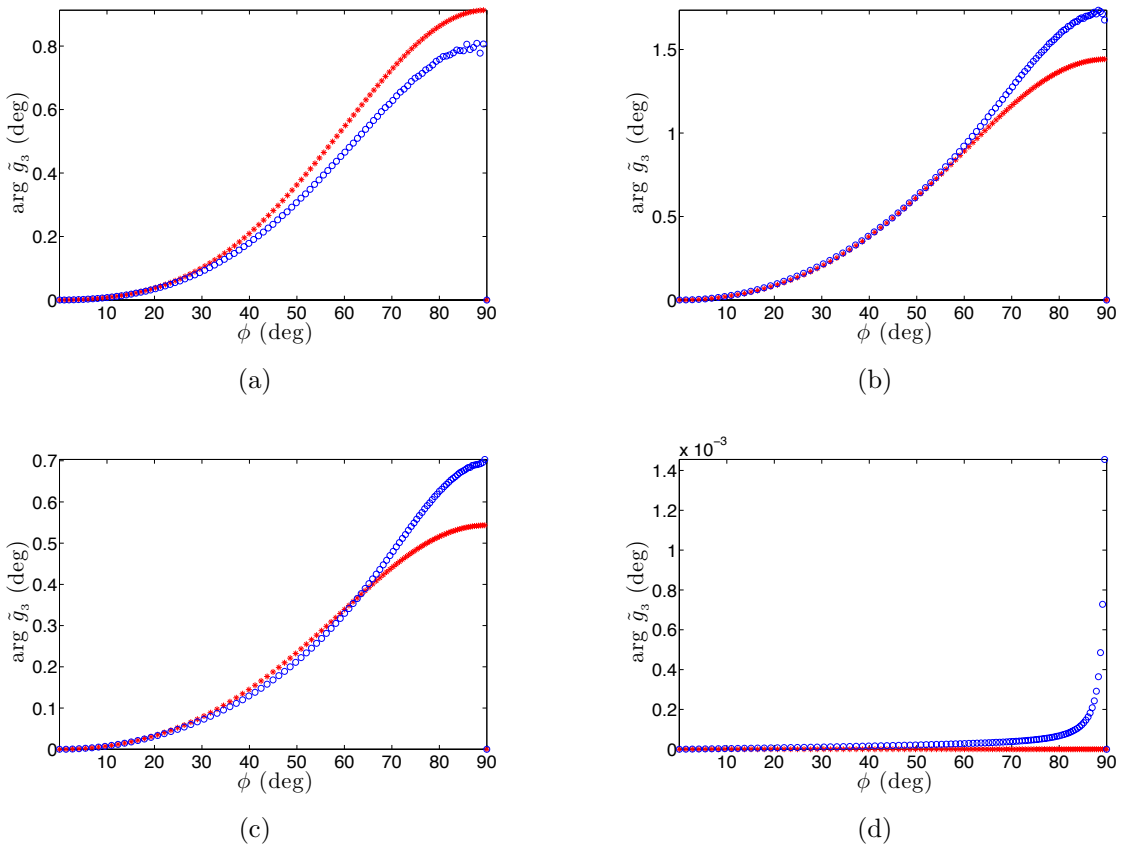

Figure 4.2. Phase of the vertical component $\tilde{g}_3$ of the polarization vector computed from the asymptotic (blue circles) and perturbation (red stars) analysis for (a) model 1, (b) model 2, (c) model 3, and (d) model 4.

The same component produced by the perturbation approach has the form (equation 4.38):

$$G_{33}(\mathbf{x}, \mathbf{x}^0, \omega) = \frac{g_3^{(1)}\, g_3^{(1)}}{4\pi\, R\mathcal{U}\, \sqrt{|K|}}\, \exp\Big(i\,\omega\,\frac{R}{\tilde{\mathcal{U}}} + i\,\frac{\pi}{2}k_s\Big). \tag{4.40}$$

The polarization vector, group velocity, and Hessian of the slowness surface in equation 4.39 are complex-valued. The only complex valued quantity in equation 4.40 is the perturbed group-velocity vector $\tilde{\mathcal{U}}$, which determines the attenuation. We found that the magnitude and argument of the energy-velocity vector $\tilde{\mathcal{U}}$ computed from the asymptotic analysis (equation 4.16) is close to that computed from perturbation analysis (equation 4.37). Also the difference between the magnitudes of the Hessian of the slowness surface ($\det \tilde{\mathbf{\Phi}}''$) in equation 4.39 and of the Gaussian curvature K in equation 4.40 is small.

Although the magnitudes of the complex-valued quantities (the polarization vector, group velocity, and the Hessian of the slowness surface) in equation 4.39 are close to their real-valued counterparts in equation 4.40, the phase of these quantities influence the phase of the Green's function.

The total phase ϕ_d of the component G_{33} in equation 4.39 can be expressed as:

$$\phi_d = 2\arg\,[\tilde{g}_3^{(1)}] - \frac{1}{2}\arg\,[\det \tilde{\mathbf{\Phi}}''] - \arg\,[\tilde{\mathcal{U}}]. \tag{4.41}$$

The values of ϕ_d for the models in Table 5.1 range between -5° to 5°, and hence do not significantly distort the phase of the Green's function (Figure 5.4). The other components of the Green's function exhibit properties similar to those of G_{33}.

Figure 4.4 compares the inhomogeneity angle ξ computed from perturbation approach (equation 4.34) and the asymptotic analysis. The values of ξ obtained by the two methods are close to one another for models 1 and 3. There is a discrepancy for model 2, which can be expected because P-wave attenuation for that model is strongly anisotropic. Although both methods employed here are approximate, asymptotic analysis is expected to be more accurate for models with strong attenuation and pronounced attenuation anisotropy. Although model 4 has substantial attenuation and an anisotropic velocity function, the inhomogeneity angle for that model vanishes because the components Q_{ij} of the phase quality factor are identical (see Appendix B).

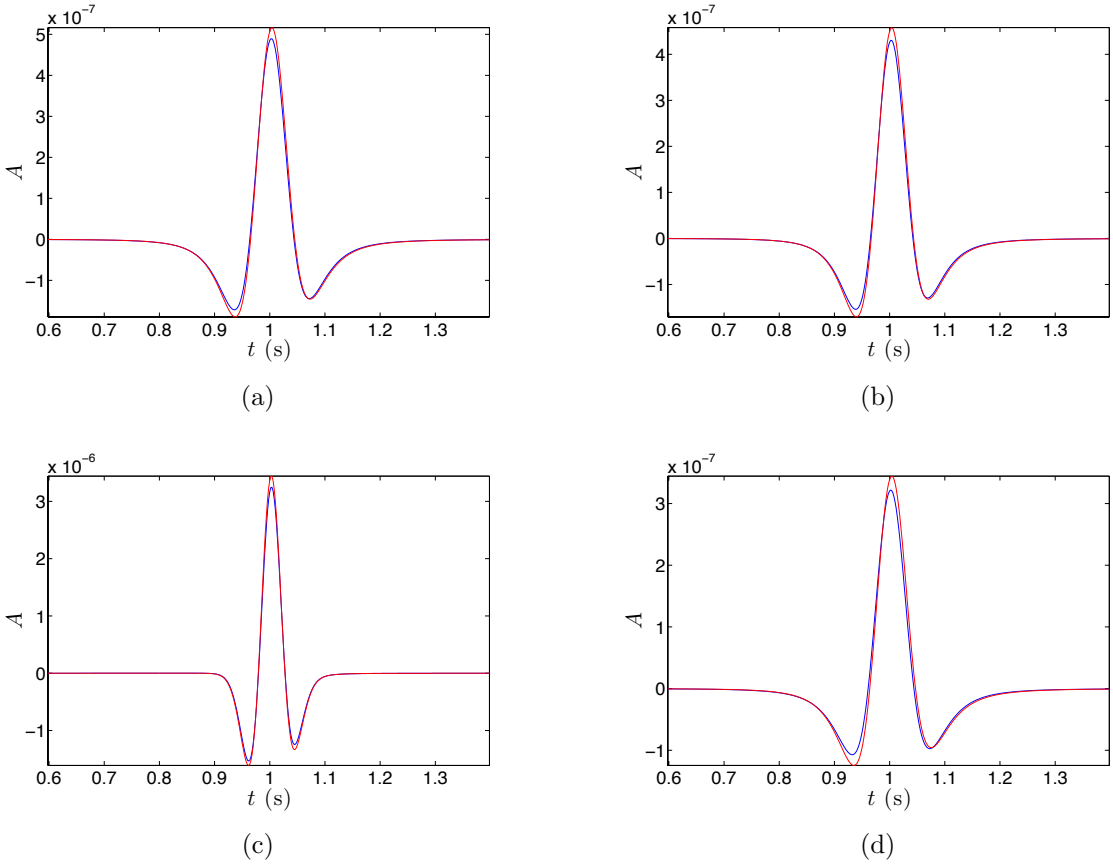

Figure 4.3. Asymptotic (blue) and perturbation (red) component G_{33} of the Green's function convolved with a Ricker wavelet of peak frequency 10 Hz for (a) model 1, (b) model 2, (c) model 3, and (d) model 4. The source-receiver line makes an angle of 45° with the symmetry axis, and the propagation time is 1 s.

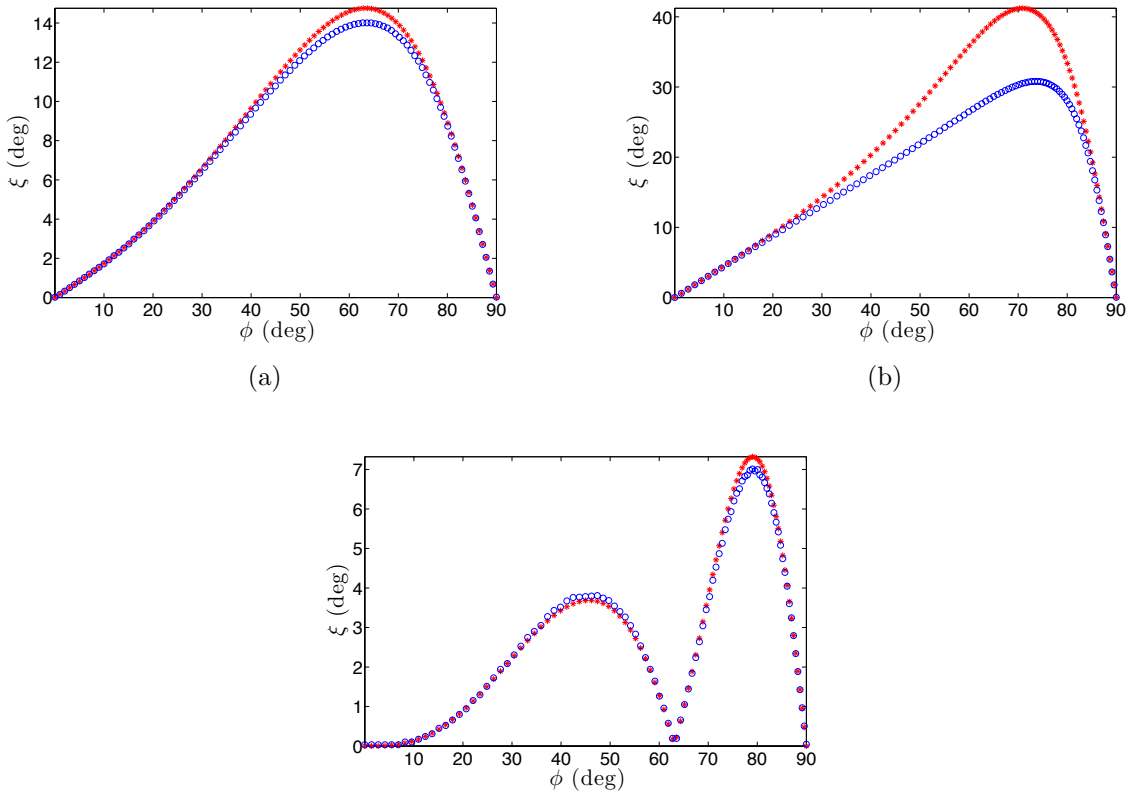

Figure 4.4. P-wave inhomogeneity angle computed from asymptotic (blue circles) and perturbation (red stars) analysis for (a) model 1, (b) model 2, and (c) model 3.

4.6 Conclusions

We presented a rigorous derivation of the asymptotic Green's function in homogeneous, attenuative, arbitrarily anisotropic media using the steepest-descent method. Application of the saddle-point condition helps identify the plane wave that makes the most significant contribution to the displacement field of each mode. Our results make it possible to evaluate the inhomogeneity angle and describe the complex-valued group-velocity vector in the high-frequency (far field) approximation.

P-wave signatures obtained from our asymptotic analysis for TI media were compared with the same quantities computed by ray-perturbation theory. The asymptotic energy-velocity vector that describes the traveltime and attenuation along the ray is close to the perturbed group-velocity vector. The inhomogeneity angles computed from the saddle-point condition and perturbation theory differ only for strongly attenuative models. Complex-valued quantities distort the phase of the Green's function in attenuative media; however, the magnitude of the phase distortion is small even for models with strong attenuation anisotropy.

Chapter 5

KIRCHHOFF MODELING FOR ATTENUATIVE ANISOTROPIC MEDIA USING GAUSSIAN BEAMS

Seismic wave propagation in attenuative media can be efficiently modeled with ray-based methods. Here, we present a methodology to generate reflection data from attenuative anisotropic media using the Kirchhoff scattering integral and summation of Gaussian beams. Green's functions are computed in the reference elastic model by Gaussian-beam summation, and the influence of attenuation is incorporated as a perturbation along the central ray. The reflected P-wave is obtained by substituting the approximate Green's functions into the Kirchhoff scattering integral. Numerical examples for a transversely isotropic (TI) medium above a horizontal reflector and a structurally complex acoustic model with a salt body illustrate the accuracy of the method.

5.1 Introduction

Attenuation analysis may provide seismic attributes sensitive to the physical properties of the subsurface. Reliable attenuation measurements have become feasible with acquisition of high-quality reflection and borehole data.

A prerequisite for estimating attenuation coefficients from seismic data is accurate and efficient modeling of wave propagation in heterogeneous attenuative media. Attenuation makes the stiffness tensor complex, which leads to velocity dispersion and amplitude decay along seismic rays and velocity dispersion. In the presence of attenuation, the stress tensor is obtained by convolving the time-domain stiffness tensor (called the relaxation tensor) with the strain tensor (Carcione, 1990), which complicates finite-difference modeling of wave propagation in the time domain. Further, simulation of a frequency-independent quality fac-

tor (constant-Q model, e.g., Kjartannson, 1979) requires superimposing various relaxation mechanisms (Xu and McMechan, 1998; Ruud and Hestholm, 2005) – a costly operation for finite-difference modeling. The approach based on the Fourier pseudospectral method proposed by Carcione (2011) avoids the computation of relaxation functions, but it is restricted to viscoacoustic media. Although the reflectivity method (Schmidt and Tango, 1986) can be used to calculate exact synthetic seismograms, the model has to be composed of horizontal, homogeneous layers.

A computationally efficient alternative is ray tracing, which can generate asymptotic Green's functions in both elastic and attenuative media (Červený, 2001). So-called "complex" ray theory developed for attenuative models treats ray trajectories and parameters computed along the ray as complex quantities (Thomson, 1997; Hanyga and Seredyňska, 2000). However, numerical implementation of complex ray theory in seismic modeling is difficult. Ray tracing in attenuative media can also be performed using perturbation methods, which involve computation of rays in a reference elastic medium with the influence of attenuation included as a perturbation along the ray (Gajewski and Pšenčik, 1992; Červený and Pšenčik, 2009; Shekar and Tsvankin, 2012).

Synthetic seismograms of reflected waves in heterogeneous media can be computed using the Kirchhoff scattering integral (Chapman, 2004). However, this method typically requires two-point ray tracing, which can produce inaccurate results for multivalued traveltimes (multipathing). Alternatively, the asymptotic Green's functions required in the Kirchhoff scattering integral can be found by summation of Gaussian beams (Bleistein, 2008; Červený, 2001). Gaussian-beam summation eliminates the need for two-point ray tracing and can accurately handle multipathing. It can also produce finite-frequency sensitivity kernels for amplitude inversion (Yomogida and Aki, 1987).

Here, we present an algorithm for computing 2.5D ray synthetic seismograms from attenuative anisotropic media. First, we describe the Kirchhoff scattering integral for purely elastic models and show how it should be modified in the presence of attenuation. Then we review the method of summation of Gaussian beams and its application to computation of the

asymptotic "two-point" Green's functions in attenuative media. Finally, this methodology is implemented for heterogeneous TI media and its accuracy is illustrated with numerical examples.

5.2 Methodology

Here we discuss the methodology to compute reflection seismic data for attenuative anisotropic media. We first describe the Kirchhoff scattering integral and the computation of Green's functions from Gaussian beam summation, and then discuss the numerical implementation of the same.

5.2.1 Kirchhoff scattering integral

Suppose the wavefield is excited by a point impulsive force located at $\mathbf{x}^s$ and aligned with the x_k-axis, and the receiver is located at $\mathbf{x}^r$. The nth ($n = 1, 2, 3$) component of the displacement field reflected from surface Σ is given in the frequency domain by (Červený, 2001):

$$G_{nk}(\mathbf{x}^r, \mathbf{x}^s, \omega) = -i\,\omega \int_\Sigma \mathcal{W}_{iq}(\mathbf{x}')\, G_{in}(\mathbf{x}', \mathbf{x}^s, \omega)\, G_{qk}(\mathbf{x}', \mathbf{x}^r, \omega)\, \mathrm{d}\Sigma\,, \tag{5.1}$$

where $\mathbf{x}'$ are points on surface Σ, and the source- and receiver-side Green's functions [$G_{in}(\mathbf{x}', \mathbf{x}^s, \omega)$ and $G_{qk}(\mathbf{x}', \mathbf{x}^r, \omega)$, respectively] are computed for a smoothed medium. The weighting function $\mathcal{W}_{iq}(\mathbf{x}')$ is represented as:

$$\mathcal{W}_{iq}(\mathbf{x}') = a^{(1)}_{ijql}\,(n_j\, p^r_l - n_l\, p^s_j)\,(1 + R)\,, \tag{5.2}$$

where $a^{(1)}_{ijql}$ is the local density-normalized stiffness tensor in the medium immediately above the reflector, $\mathbf{n}$ is the normal to the reflector, $\mathbf{p}^s$ and $\mathbf{p}^r$ are the source- and receiver-side slowness vectors at the scattering point, respectively, and R is the PP-wave reflection coefficient.

Equation 5.1 is valid for an arbitrary scattering surface, and all Green's functions have to be computed in 3D. However, if we assume that the medium properties do not vary in the

x_2-direction, and the [x_1, x_3]-plane is a plane of symmetry, equation 5.1 can be rewritten in a 2.5D form. Then the surface integral in equation 5.1 can be reduced to a line integral by the method of stationary phase (Bleistein, 1984). Following Bleistein (1986), we apply the stationary-phase method to obtain the 2.5D form of the integral in equation 5.1:

$$G_{nk}(\mathbf{x}^r, \mathbf{x}^s, \omega) = -i\sqrt{2\,\pi\,\omega}\int_{C,\,x_2=0} \frac{1}{\sqrt{\sigma}}\,\mathcal{W}_{iq}(\mathbf{x}')\,G_{in}(\mathbf{x}', \mathbf{x}^s, \omega)\,G_{qk}(\mathbf{x}', \mathbf{x}^r, \omega)\,\mathrm{d}s, \qquad (5.3)$$

where the Green's functions are defined in 2.5D, the scatterer is reduced to the curve C that lies in the [x_1, x_3]-plane, ds is an elementary arc-length along C, and function σ accounts for out-of-plane phenomena:

$$\sigma = \Big[\frac{1}{\partial^2 T(\mathbf{x}', \mathbf{x}^s)/\partial x_2^2} + \frac{1}{\partial^2 T(\mathbf{x}', \mathbf{x}^r)/\partial x_2^2}\Big]_{x_2=0}; \qquad (5.4)$$

$T(\mathbf{x}', \mathbf{x}^s)$ is the traveltime from the source to the scatterer and $T(\mathbf{x}', \mathbf{x}^r)$ is the traveltime from the receiver to scatterer. The second-order spatial derivatives of the traveltime functions may be calculated by dynamic ray tracing.

Equations 5.1-5.4 can be extended to attenuative media by making the stiffness tensor complex and replacing the elastic Green's functions with their viscoelastic counterparts. Although the reflection coefficient and slowness vector also become complex in attenuative media, we compute these quantities for the reference elastic medium. Unless attenuation is anomalously high, plane-wave reflection coefficients are not significantly distorted in attenuative media (Behura and Tsvankin, 2009b). While the complex-valued slowness vectors at the reflector can somewhat change the weighting function defined in equation 5.2, they do not significantly contribute to the displacement computed from equation 3 because attenuation is a propagation phenomenon.

5.2.2 Asymptotic Green's function as a sum of Gaussian beams

Although the Green's functions in equation 3 can be computed by two-point ray tracing (Bulant, 1996), that method cannot accurately handle multipathing and requires a search for the ray connecting the source and receiver. A more rigorous approach to modeling asymptotic Green's functions involves summation of Gaussian beams (Červený, 2001). Here,

we start with analysis of 2.5D elastic anisotropic Green's functions and then describe the modifications needed for extending the methodology to attenuative media.

The Green's function $\mathbf{G}(\mathbf{x}', \mathbf{x}^s, \omega)$ can be found as a sum of Gaussian beams (Červený, 2001):

$$G_{ik}(\mathbf{x}', \mathbf{x}^s, \omega) = \Phi(\theta_0) \int u_{ik}[R(\gamma + \theta_0)] \, \mathrm{d}\gamma \,, \tag{5.5}$$

where $u_{ik}[R(\gamma + \theta_0)]$ represents a single Gaussian beam concentrated around central ray $R(\gamma + \theta_0)$, and $\Phi(\theta_0)$ is the angle-dependent weighting function. Suppose that the ray $R(\theta_0)$ with the initial (at the source $\mathbf{x}_s$) take-off phase angle θ_0 with respect to the horizontal illuminates a point close to $\mathbf{x}'$. The range of integration in equation 5.5 is then chosen to be symmetric over θ_0, and the Green's function is obtained by summation over a fan of beams that correspond to a certain range of angles γ.

Červený (2001) derives the weighting function $\Phi(\theta_0)$ for heterogeneous media by evaluating the Gaussian integral. However, that result is valid only for "regular ray regions" that do not include caustics. Alternatively, the weighting function may be calculated in an asymptotic sense (Bleistein, 2008). Although the asymptotic function $\Phi(\theta_0)$ for heterogeneous media is approximate, it remains stable even in regions with caustics. The asymptotic angle-dependent weighting function for anisotropic media is derived in Appendix E (equation E.9).

To evaluate the contribution of the Gaussian beam centered around the ray R to $\mathbf{G}(\mathbf{x}', \mathbf{x}^s, \omega)$, we consider the point $\mathbf{x}''$ closest to $\mathbf{x}'$ on R. Then the contribution $u_{ik}[R(\gamma+\theta_0)]$ to $\mathbf{G}(\mathbf{x}', \mathbf{x}^s, \omega)$ is (Červený and Pšenčik, 2010):

$$u_{ik}(\mathbf{x}', \mathbf{x}^s, \omega) = g_i(\mathbf{x}'') \, g_k(\mathbf{x}'') \, \frac{1}{4\pi\sqrt{c(\mathbf{x}^s)c(\mathbf{x}'')}} \, \frac{1}{\sqrt{\det\tilde{\mathbf{W}}(\mathbf{x}'', \mathbf{x}^s)}} \, e^{-i\omega\tilde{T}(\mathbf{x}'', \mathbf{x}^s)}, \tag{5.6}$$

where the angle-dependent P-wave phase velocity corresponding to the ray $R(\gamma + \theta_0)$ at the source and receiver location is represented by $c(\mathbf{x}^s)$ and $c(\mathbf{x}'')$, respectively, $\mathbf{g}$ is the polarization vector, and $\tilde{T}(\mathbf{x}', \mathbf{x}^s)$ is the complex traveltime (Červený and Pšenčik, 2010):

$$\tilde{T}(\mathbf{x}', \mathbf{x}^s) = T(\mathbf{x}'', \mathbf{x}^s) + (\mathbf{x}' - \mathbf{x}'')^T \, \mathbf{p}[R(\gamma + \theta_0)] + \frac{1}{2}(\mathbf{x}' - \mathbf{x}'')^T \, \tilde{\mathbf{M}}^x \, (\mathbf{x}' - \mathbf{x}''), \tag{5.7}$$

where the superscript "T" denotes the transpose, $\mathbf{p}$ is the slowness vector corresponding to the ray $R(\gamma+\theta_0)$, and $\tilde{\mathbf{M}}^x$ is the complex-valued matrix of the second traveltime derivatives found by transforming the matrix $\tilde{\mathbf{M}}$ defined in Appendix D (equation D.15) to the Cartesian coordinates (Červený and Pšenčik, 2010). The matrix $\tilde{\mathbf{W}}(\mathbf{x}'', \mathbf{x}^s)$ depends on the initial value $\tilde{\mathbf{M}}^0$ of $\tilde{\mathbf{M}}$:

$$\tilde{\mathbf{W}}(\mathbf{x}'', \mathbf{x}^s) = \mathbf{Q}_1(\mathbf{x}'', \mathbf{x}^s) + \mathbf{Q}_1(\mathbf{x}'', \mathbf{x}^s)\, \tilde{\mathbf{M}}^0, \tag{5.8}$$

where $\mathbf{Q}_1$ and $\mathbf{Q}_2$ are computed by dynamic ray tracing in ray-centered coordinates (see Appendix D). The matrix $\tilde{\mathbf{M}}^0$ is given by equation D.16:

$$\tilde{\mathbf{M}}^0 = \frac{i}{l\omega^2}\, \mathbf{I}, \tag{5.9}$$

where $\mathbf{I}$ is the identity matrix and l represents the initial beam width. The choice of l and the sampling of the parameter γ are discussed in the next section.

If the medium is attenuative, equation 5.5 can be adapted to obtain the viscoelastic Green's function $\mathbf{G}^{\mathrm{att}}(\mathbf{x}', \mathbf{x}^s, \omega)$ (Červený, 1985):

$$G^{\mathrm{att}}_{ik}(\mathbf{x}', \mathbf{x}^s, \omega) = \Phi(\theta_0) \int \mathbf{u}^{\mathrm{att}}_{ik}[R(\gamma+\theta_0)]\, \mathrm{d}\gamma\,. \tag{5.10}$$

The weighting function $\Phi(\theta_0)$ remains unchanged from that in elastic media, whereas $\mathbf{u}^{\mathrm{att}}_{ik}(R)$ becomes

$$\mathbf{u}^{\mathrm{att}}_{ik}[R(\gamma+\theta_0)] = \mathbf{u}_{ik}[R(\gamma+\theta_0)]\, e^{-\omega\, t^*(\mathbf{x}', \mathbf{x}^s)}\,, \tag{5.11}$$

where $\mathbf{u}_{ik}[R_0(\gamma)]$ is computed for the reference elastic medium, and $t^*(\mathbf{x}', \mathbf{x}^s)$ is a real-valued quantity called the "dissipation factor" (Gajewski and Pšenčik, 1992), which accounts for the attenuation-induced amplitude decay along the central ray. The factor t^* can be calculated using perturbation methods (Červený and Pšenčik, 2009; Shekar and Tsvankin, 2012).

5.2.3 Implementation

The initial beam width for Gaussian beams in anisotropic media can be chosen as (Alkhalifah, 1995):

$$l = \frac{V_{\text{avg}}}{f_{\min}}, \tag{5.12}$$

where V_{avg} represents the average of the horizontal and vertical phase velocities over the entire model, and $f_{\min}$ is the lowest frequency of interest.

Next, we discuss the sampling of the parameter γ in the summation of Gaussian beams (equations 5.5 and 5.10). Following Hill (1990), Hale (1992) derives the following expression for the sampling in the horizontal slowness p_x:

$$\mathrm{d}p_x = \frac{1}{6\, l\, \sqrt{f_{\min}\, f_{\max}}}, \tag{5.13}$$

where $f_{\max}$ is the highest frequency of interest. In TI media, the velocity c is a function of angle, and the horizontal slowness can be expressed as:

$$p_x = \frac{\cos(\gamma + \theta_0)}{c(\gamma + \theta_0)}. \tag{5.14}$$

Using equations 5.13 and 5.14, the sampling $\mathrm{d}\gamma$ can be related to $\mathrm{d}p_x$ by:

$$\begin{aligned} |\mathrm{d}p_x| &= \Big| \frac{\sin(\gamma + \theta_0)}{c(\gamma + \theta_0)} + \frac{\cos(\gamma + \theta_0)}{c^2(\gamma + \theta_0)} \frac{\mathrm{d}c(\gamma + \theta_0)}{\mathrm{d}\gamma} \Big|_{\gamma=0} |\mathrm{d}\gamma| \\ &= \Big| \frac{\sin\theta_0}{c(\theta_0)} + \frac{\cos\theta_0}{c^2(\theta_0)} \frac{\mathrm{d}c(\gamma + \theta_0)}{\mathrm{d}\gamma} \Big| \, |\mathrm{d}\gamma|; \end{aligned} \tag{5.15}$$

the derivative $\mathrm{d}c(\gamma + \theta_0)/\mathrm{d}\gamma$ is evaluated at $\gamma = 0$.

We calculate the reflected wavefields in attenuative heterogeneous media using equation 5.3 with the source-to-scatterer and scatterer-to-receiver Green's functions obtained from equation 5.6. The Gaussian beams in attenuative media are computed from equation 5.11. The beams are constructed in the reference elastic medium and the dissipation factor t^* is found as a perturbation along the central ray (Červený and Pšenčik, 2009; Shekar and Tsvankin, 2012). The weighting function $\Phi(\theta_0)$ for the summation of Gaussian beams is also

calculated in the reference elastic medium. Likewise, the weighting functions σ and $\mathcal{W}_{iq}$ for the Kirchhoff integral (equation 5.3) are found from the quantities stored during the modeling of Gaussian beams in the reference elastic medium. For TI models, the reflection coefficient R in equation 2 is obtained from the weak-contrast, weak-anisotropy approximation presented by Rüger (1997).

The outlined method involves a number of approximations. The Kirchhoff scattering integral itself is an asymptotic solution that ignores multiple scattering (Chapman, 2004). The method of summation of Gaussian beams is limited to computing asymptotic Green's functions in smooth media. Finally, the influence of attenuation is modeled using perturbation theory, which is valid for weakly dissipative media. Numerical examples illustrating the accuracy of the perturbation approach can be found in Shekar and Tsvankin (2012).

5.3 Synthetic tests

First, we verify the accuracy of the Gaussian beam summation method in constructing the asymptotic Green's function in unbounded media. Table 5.1 lists the velocity and attenuation parameters for the two TI models used to test the Gaussian beam summation. Model 1 is homogeneous, while model 2 has a vertical gradient in the symmetry-direction (vertical) P-wave velocity V_{P0}:

$$V_{P0}(z) = V_{P0}(0)\left(1 + k_z\, z\right), \tag{5.16}$$

where k_z is the vertical gradient of V_{P0}. Figure 5.1 compares the Green's function computed from perturbation ray theory (Červený and Pšenčik, 2009; Shekar and Tsvankin, 2012) and Gaussian beam summation (equation 5.11) for the two TI models. Note that equation 5.11 also employs perturbation ray theory to incorporate the contribution of attenuation. The two functions are close to each other for model 1 (Figure 5.1a, c, and e), while there is a noticeable deviation in the amplitudes for model 2 (Figure 5.2d, e, and f), which has a vertical velocity gradient. This is due to the fact that the asymptotic weighting function $\Phi(\theta_0)$ (equation E.9) is derived for a homogeneous medium. The displacement computed from

Table 5.1. Parameters of two VTI models used to test the accuracy of Gaussian beam summation. Model 2 is vertically heterogeneous with a constant gradient (k_z) in V_{P0}. The attenuation-anisotropy parameters $\epsilon_{_Q}$ and $\delta_{_Q}$ are defined in Zhu and Tsvankin (2006) and Tsvankin and Grechka (2011; Chapter 8).

	Model 1	Model 2
V_{P0} (km/s)	3.00	3.00
V_{S0} (km/s)	1.50	1.50
k_z (1/km)	0.0	1.50
ϵ	0.40	0.40
δ	0.25	0.25
Q_{P0}	10	10
Q_{S0}	10	10
$\epsilon_{_Q}$	-0.40	-0.40
$\delta_{_Q}$	-0.25	-0.25

the beam summation exhibits a phase distortion because only a finite number of Gaussian beams is taken into account.

In Figure 5.2, we test the accuracy of the Kirchhoff scattering integral combined with Gaussian-beam summation in generating reflection data. Table 5.2 displays the velocity and attenuation parameters for a model that includes two homogeneous VTI layers separated by a horizontal reflector. The exact reflected wavefield (Figure 2a) was computed with the reflectivity method (Mallick and Frazer, 1990). The displacement obtained from the Kirchhoff scattering integral (Figure 2b) almost coincides with the exact solution, except for a small phase distortion (Figure 2c, d).

Next, the algorithm is applied to a structurally complicated but isotropic model. Figure 5.3a displays a P-wave velocity slice extracted from the SEG/EAGE acoustic salt model (Aminzadeh et al., 1996). The algorithm presented above was modified for acoustic media by using the scalar Green's and weighting functions in the Kirchhoff scattering integral (equation 5.3). The background Green's functions were constructed by Gaussian-beam summation in a smoothed version of the section suitable for ray tracing (Figure 5.3b). The model in Figure 5.3b was taken from Bulant (2002), whose smoothing algorithm preserves

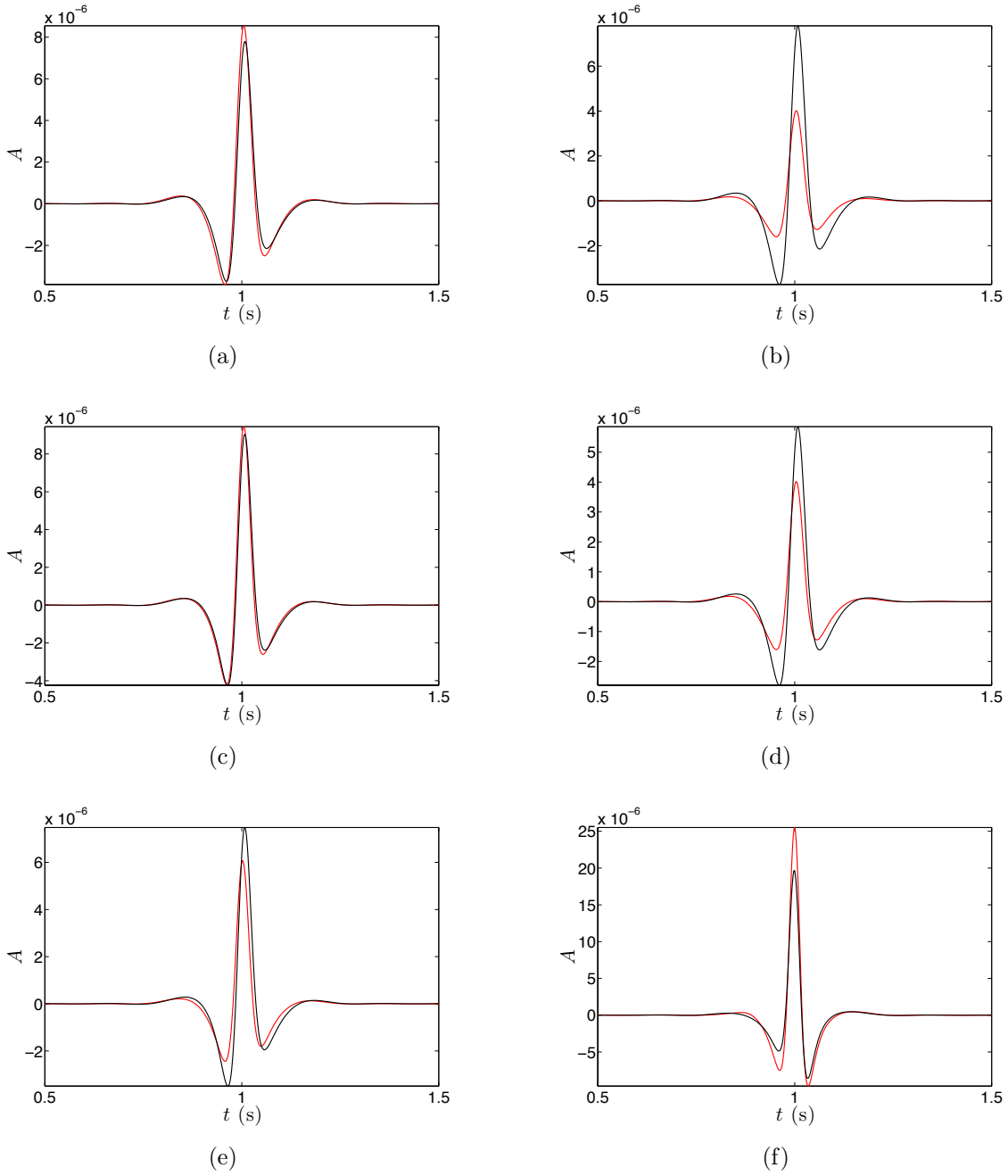

Figure 5.1. Comparison of the vertical displacement component computed using the Gaussian-beam summation method (red curves) and perturbation ray theory (black) for model 1 (a, c, e) and model 2 (b, d, f) from Table 5.1. The group angle with the vertical is (a, b) 0°, (c, d) 30°, and (e, f) 60°; the propagation time is 1 s. The wavefield is excited by a vertical point force; the source signal is a Ricker wavelet with a central frequency of 30 Hz.

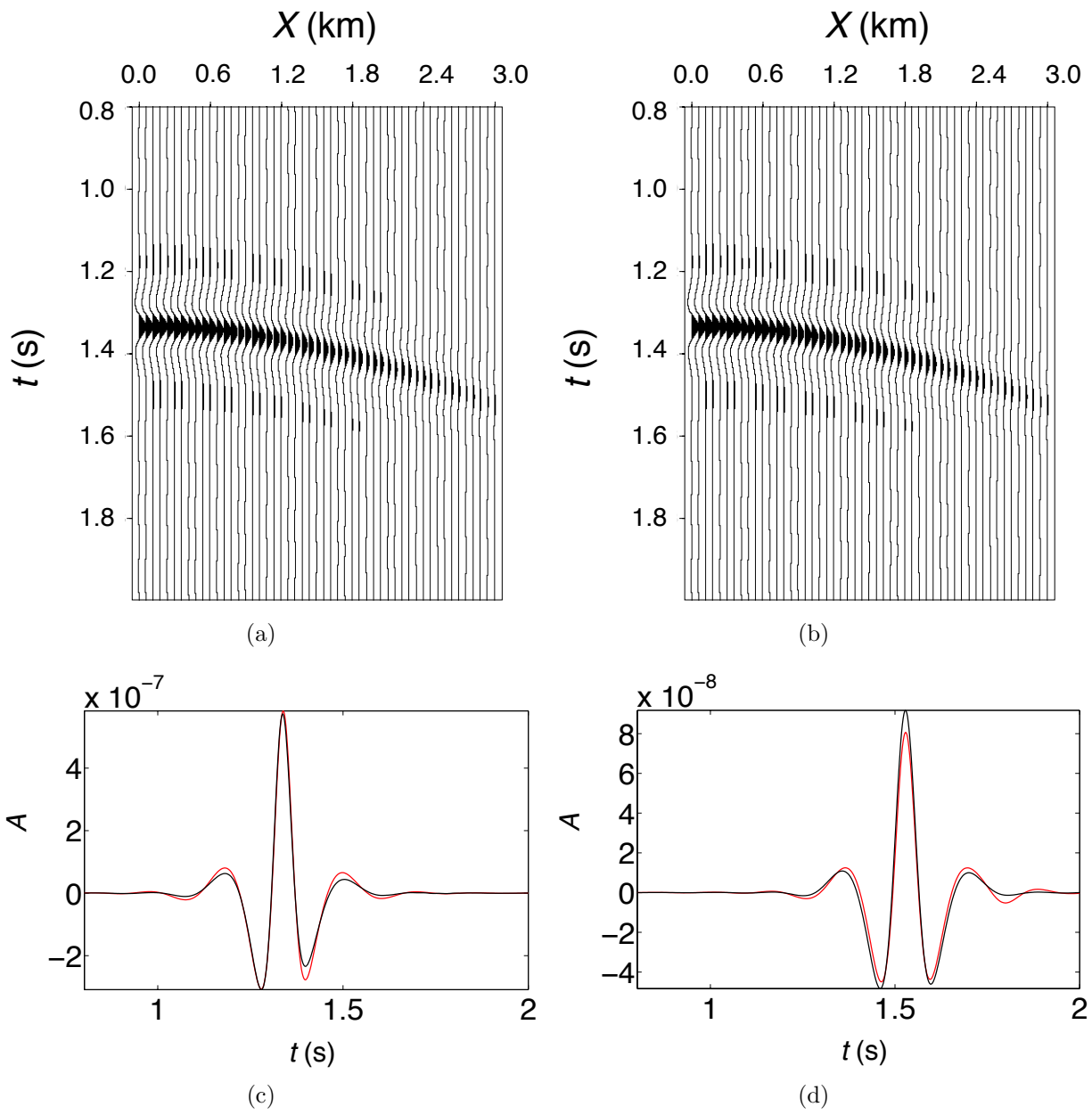

Figure 5.2. Vertical displacement for the model in Table 1 generated using (a) the reflectivity method and (b) the Kirchhoff scattering integral. The wavefield is excited and recorded on top of the model. The source is a vertical force at $X = 0$ km and the receivers are placed between $X = 0$ km and $X = 3.0$ km with a 25 m increment. The source signal is a Ricker wavelet with a central frequency of 10 Hz. The traces from the reflectivity method (black) and the Kirchhoff scattering integral (red) for (c) $X = 0$ km and (d) $X = 3$ km.

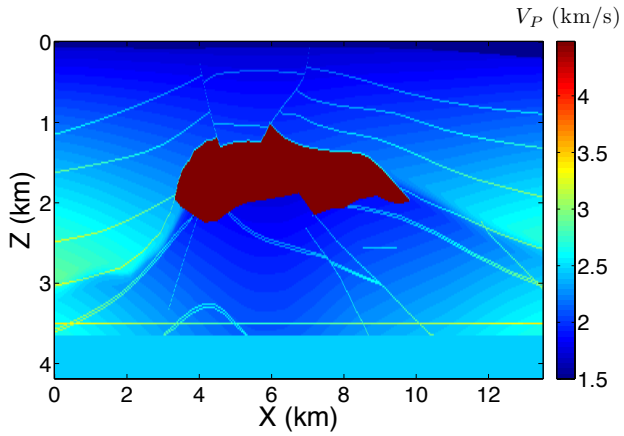

(a)

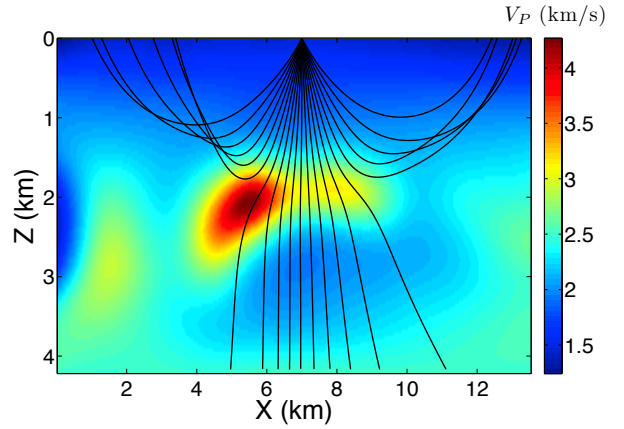

(b)

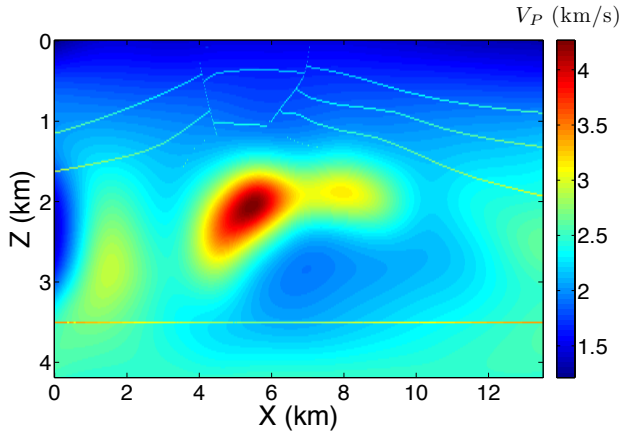

(c)

Figure 5.3. (a) 2D velocity slice from the SEG/EAGE salt model. (b) The smoothed version of the model from plot (a) used for ray tracing. A fan of rays originating from a shot at $X = 6.68$ km with a 4° increment in the take-off angle is plotted in black. (c) Model from plot (b) with shallow interfaces and the horizontal reflector from (a).

Table 5.2. Parameters of a two-layer VTI model used to test the Kirchhoff scattering integral.

	Layer 1	Halfspace
Thickness (km)	2.00	–
V_{P0} (km/s)	3.00	3.20
V_{S0} (km/s)	1.50	1.60
ϵ	0.20	0.10
δ	0.10	0.05
Q_{P0}	10	100
Q_{S0}	10	100
$\epsilon_{_Q}$	0.0	0.0
$\delta_{_Q}$	0.75	0.0

traveltimes and minimizes ray chaos (e.g., exponential divergence of rays with similar initial conditions) in initial-value ray tracing. We introduced isotropic attenuation in the model with the constant P-wave quality factor $Q_{_P} = 100$. The contribution of attenuation was incorporated by employing perturbation ray theory, as discussed above. Rays traced from a source at $X = 6.68$ km (Figure 5.3b) exhibit shadow zones and multipathing due to vertical and lateral velocity variations.

P-wave reflection data in Figure 5.4 were generated from the Kirchhoff scattering integral for the model in Figure 5.3c. To gain insight into the performance of the algorithm, we analyze the reflection from the horizontal interface below the salt body at a depth of 3.6 km (Figure 5.4b ,d, f). Figure 5.5 shows the background Green's functions produced by Gaussian-beam summation for corresponding to the scattering points on that horizontal reflector. The amplitudes of the Green's functions are smooth for a range of near offsets around the source, they decrease abruptly around $X = 6.5$ km, which corresponds to the high velocity zone in the model (Figure 5.3c). These amplitude anomalies are due to limited ray coverage for parts of the section (Figure 5.3b), which causes errors in the paraxial traveltime approximation.

The accuracy of the algorithm in accounting for attenuation can be verified by computing the attenuation coefficients from the modeled data. We apply the spectral-ratio method

(Johnston and Toksöz, 1981; Zhu et al., 2007a) which operates with isolated events, and the reflection from the interface at 3.6 km is well separated from the shallower reflections. Because the attenuation function for this model is spatially invariant, the slope of the logarithmic spectral ratio obtained by dividing the amplitude spectrum of an event and the source spectrum yields the product of the traveltime t along the raypath and the normalized P-wave attenuation coefficient $\mathcal{A}_P = 1/(2\,Q_P)$ (Behura and Tsvankin, 2009a). The estimated attenuation coefficient is close to the actual value ($\mathcal{A}_P = 0.005$) for a range of receiver positions, but there are deviations for the receiver coordinates in the range $4.5 - 7.0$ km (Figure 5.6). This is due to the uneven ray coverage at the horizontal reflector (Figure 5.3b). The paraxial traveltimes are less accurate in the high velocity zone in Figure 5.3c, which causes distortions in the amplitudes produced by beam summation.

5.4 Conclusions

We introduced a ray-based methodology for computing synthetic seismograms of reflected waves from attenuative anisotropic media. The wavefield is generated with the Kirchhoff scattering integral that includes 2.5D asymptotic Green's functions. Summation of Gaussian beams is employed to calculate the Green's functions in the reference purely elastic, anisotropic medium. The contribution of attenuation to Gaussian beams is accounted for by perturbation ray theory.

The accuracy of the Gaussian-beam summation method in producing Green's functions was verified for a highly attenuative TI layer. In addition, we compared the output of the Kirchhoff scattering integral with the exact seismograms in a horizontally layered medium computed using the reflectivity method. These examples confirm that the proposed technique adequately models P-wave reflections even in the presence of strong anisotropic attenuation. The displacements computed from beam summation, however, exhibit minor phase distortions due to a finite number of beams.

The performance of the algorithm was also analyzed for a structurally complex acoustic model containing a salt body. The attenuation coefficient estimated by the spectral-ratio

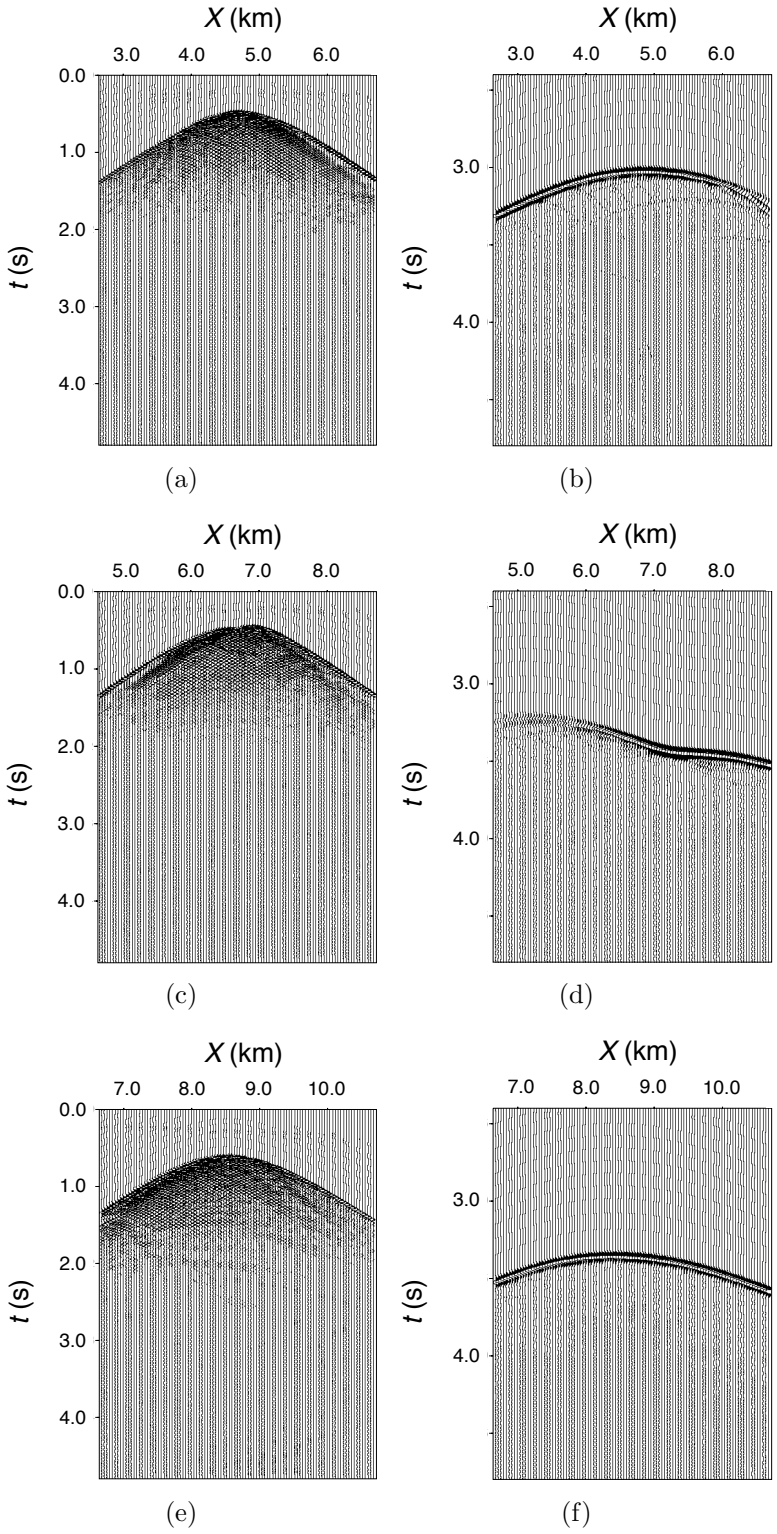

Figure 5.4. (a, c, e) P-wave reflection data (pressure) for the model in Figure 5.3c generated by the Kirchhoff scattering integral for different source locations. (b, d, e) Arrivals from the horizontal reflector at a depth of 3.6 km; these reflections are almost invisible on plots (a, c, e) because of their relatively low magnitude. The explosive source is placed at (a, b) $X = 4.68$ km, (c, d) $X = 6.68$ km, and (e, f) $X = 8.68$ km. The source signal is a Ricker wavelet with a central frequency of 30 Hz.

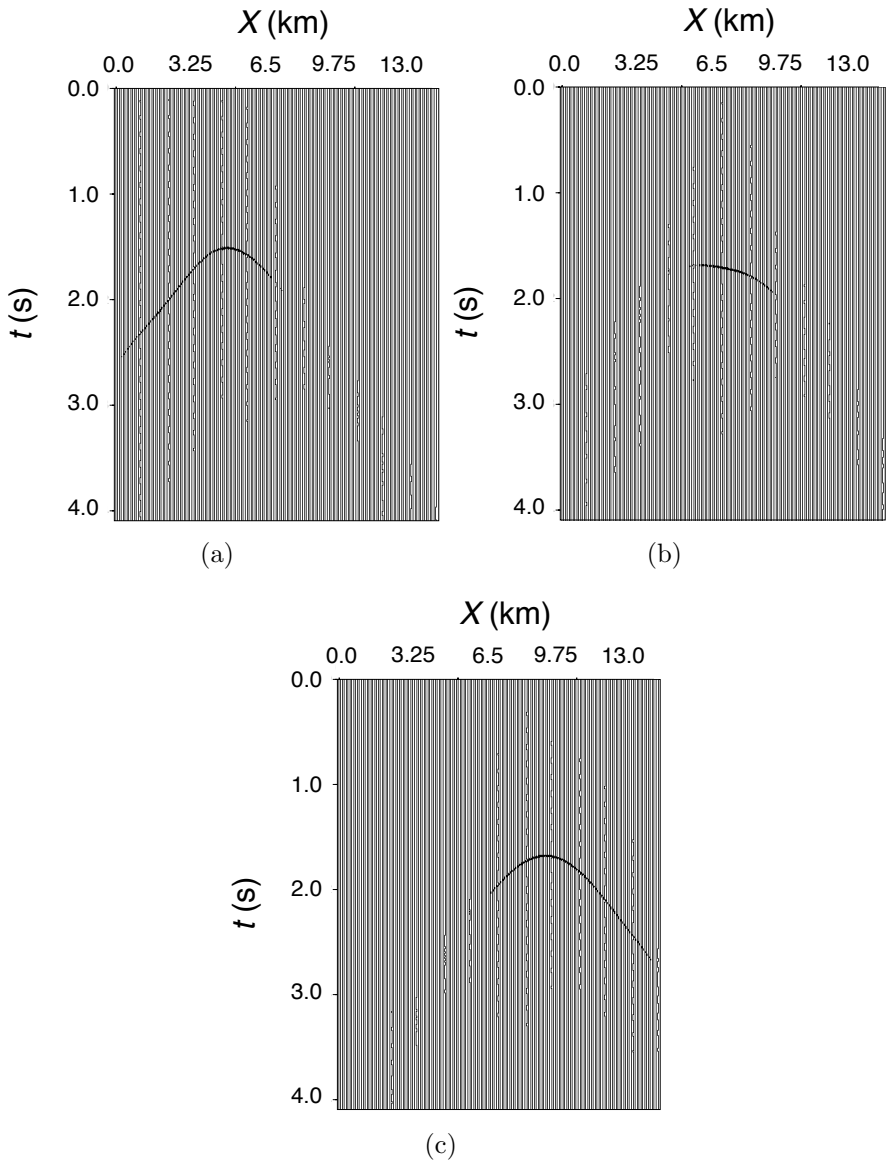

Figure 5.5. P-wave Green's functions for the model in Figure 5.3c produced by Gaussian-beam summation for a source at (a) $X = 4.68$ km, (b) $X = 6.68$ km, and (c) $X = 8.68$ km. The scattering points are located on the horizontal reflector at a depth of 3.6 km.

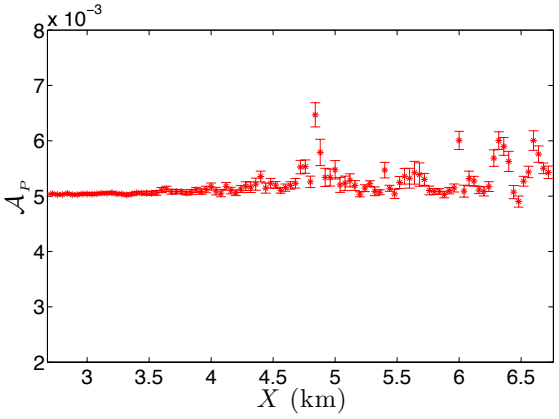

(a)

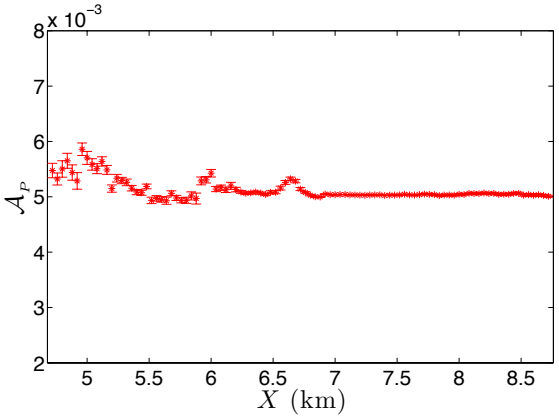

(b)

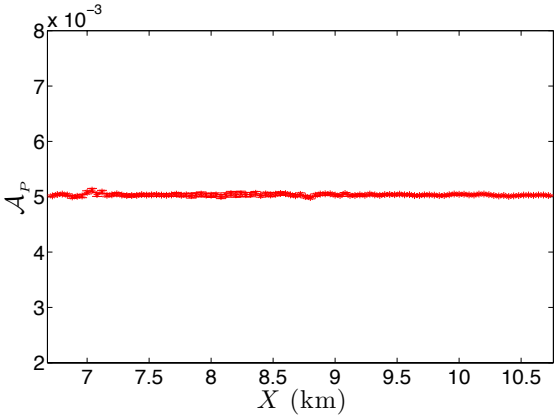

(c)

Figure 5.6. P-wave attenuation coefficient computed using the reflection from the horizontal interface (Figure 5.4b, d, e). The error bars mark two standard deviations in $\mathcal{A}_P$ (95% confidence intervals). The horizontal axis is the receiver coordinate; the source is placed at (a) $X = 4.68$ km, (b) $X = 6.68$ km, and (c) $X = 8.68$ km.

method from the data generated with our method is generally close to the actual value. Some distortions in the reconstructed attenuation coefficients are caused by insufficient ray coverage related to the heterogeneity of the velocity field.

Chapter 6

SUMMARY AND RECOMMENDATIONS

In this thesis I introduced new techniques for modeling and estimation of attenuation coefficients from surface and crosshole seismic surveys.

Chapter 2 extended the attenuation layer-stripping method of Behura and Tsvankin (2009a) to evaluation of interval shear-wave attenuation in layered anisotropic media. The algorithm operates with pure PP reflections and mode-converted PS data, and combines the PP+PS=SS method with velocity-independent layer stripping for both traveltimes and frequency-domain amplitudes. The vertical incidence plane is assumed to be a plane of mirror symmetry throughout the model, and the overburden should be horizontal and laterally homogeneous with a horizontal plane of symmetry. The shear-wave interval attenuation coefficient can be reconstructed without knowledge of the overburden velocity field. The method was tested on synthetic data from layered VTI media and symmetry planes of orthorhombic media. The SV-wave interval attenuation coefficient was constructed for the range of incidence phase angles limited by the critical reflection angle for the mode-converted PS waves. Consequently, the only well-constrained parameters were the SV-wave symmetry-direction coefficient $\mathcal{A}_{S0}$ for VTI media and the vertical attenuation coefficients of the split S-waves for orthorhombic media. The attenuation splitting parameter estimated by this method could be a valuable attribute in fracture detection.

A case study of cross hole data excited by perforation shots fired in a tight-gas reservoir to induce hydraulic fracturing was presented in Chapter 3. I developed a methodology to estimate the P-wave anisotropic attenuation coefficient from the data acquired for a narrow range of propagation directions. The spectral-ratio method applied to pairs of traces provided the input to the inversion for the attenuation coefficient, which was represented as a quadratic polynomial in the polar and azimuthal angles. The angles were measured around

a "central ray" corresponding to the average ray direction for each stage of the perforation shots. Taking anisotropy into account was found to be crucial to fit the attenuation measurements. The mean value of the attenuation coefficient decreased with successive stages of hydraulic fracturing and stimulation, which is likely related to the diffusion of fluids through the medium. Analysis of the attenuation signature was complicated by the fact that the reservoir formation consisted mostly of shale, which is expected to exhibit intrinsic attenuation anisotropy.

The asymptotic Green's function in homogeneous, attenuative, arbitrarily anisotropic media was derived in Chapter 4 using the steepest-descent method. The saddle-point condition yielded the plane wave that makes the most significant contribution to the displacement field of each mode. The asymptotic analysis helped evaluate the inhomogeneity angle and the complex-valued group-velocity vector. I compared the P-wave signatures obtained for TI media from the asymptotic analysis and ray-perturbation theory. The asymptotic complex-valued polarization vector and energy-velocity vector (the latter describes the traveltime and attenuation along the ray) were close to their counterparts computed from the perturbation approach. The values of the inhomogeneity angle from the two approaches differed only for strongly attenuative models. The phase distortion of the Green's function produced by the attenuation-related complex-valued quantities is relatively minor.

Chapter 5 presented a methodology for computing reflection data from 2.5D attenuative anisotropic media. The Kirchhoff scattering integral was employed to generate P-wave reflections, with the background Green's functions computed by summation of Gaussian beams. The contribution of attenuation to Gaussian beams was incorporated by perturbation ray theory. Numerical examples for a highly attenuative TI layer confirmed the accuracy of the Gaussian-beam summation method in producing the asymptotic Green's functions. Reflection data generated by the Kirchhoff scattering integral for a TI model with a horizontal interface was close to that from the exact reflectivity method. The algorithm is suitable to model P-wave reflections even in the presence of strong anisotropic attenuation, although the displacements produced by beam summation exhibit slight phase distortions.

The method was also tested on a structurally complex acoustic model containing a salt body. The spectral-ratio method was employed to reconstruct the attenuation coefficient from the modeled data. While the estimated coefficient was generally close to the actual constant value ($Q = 100$), there were some errors in Q due to amplitude distortions caused by insufficient ray coverage in parts of that structurally complex model.

6.1 Recommendations for future work

The algorithm to estimate the shear-wave interval attenuation coefficient introduced in this thesis is limited to layered media with a horizontal, laterally homogeneous overburden that has a horizontal symmetry plane. Similarly, it was assumed that the medium between the wells in the cross hole study was homogeneous. Indeed, it is most practical to perform attenuation analysis for structurally simple sub-surface models. Attenuation estimation in the presence of structural complexity requires accurate knowledge of velocity, even for isotropic media. Since velocity anisotropy causes a strong directional dependence of amplitude, and attenuation anisotropy is coupled to velocity anisotropy, prior knowledge of the anisotropic velocity field is essential for successful attenuation inversion.

One possibility is to divide the section into factorized VTI blocks, in which the ratios of the real-valued stiffness coefficients and, consequently, the velocity-anisotropy parameters are constant. Velocity analysis for this model was developed by Sarkar and Tsvankin (2004), who show that the medium parameters can be constrained with minimal a priori information. Piecewise-factorized VTI models may be extended to attenuative media, with constant Thomsen-style attenuation-anisotropy parameters and linearly varying P-wave vertical quality factor in each block. P-wave reflection data can be generated with the modeling algorithm introduced in this thesis, and the initial values of the attenuation coefficients may be obtained by the attenuation layer-stripping algorithm. Updating of the attenuation parameters can be carried out block-by-block using an appropriately designed inversion scheme.

A potentially important application of attenuation measurements may be in detection of "sweet spots" of increased production in gas reservoirs. The presence of gas usually leads to

areas of higher P-wave attenuation, which could be identified by inversion of surface or VSP data (Behura et al., 2012). Most "unconventional" hydrocarbon reservoirs are composed of Shale layers, which typically exhibit intrinsic attenuation anisotropy (Tsvankin and Grechka, 2011). Therefore, estimation of attenuation anisotropy may be a crucial component in the characterization of these reservoirs.

Existing algorithms for estimating attenuation, such as the spectral-ratio method and the centroid shift method, operate with isolated events. Multiple reflections and/or interfering events cause distortions in the attenuation coefficients estimated by these techniques. Also, existing methods are not sufficiently stable in the presence of noise. Development of robust techniques for attenuation analysis is critically important for obtaining realistic attenuation coefficients and resolving attenuation anisotropy.

It is well known that the presence of attenuation leads to velocity dispersion. While dispersion has been studied extensively in the laboratory and on seismic data, few studies are focused on anisotropic models (e.g., Jakobsen and Chapman, 2003). The influence of attenuation anisotropy on dispersion needs to be evaluated on both rock-physics and seismic data. Velocity dispersion is implicit in the "relaxation mechanisms" employed by most time-domain finite-difference modeling schemes. The currently employed relaxation mechanisms, however, are somewhat artificial, and could be improved with a better understanding of velocity dispersion in the seismic bandwidth.

REFERENCES

Adam, L., M. Batzle, K. Lewallen, and K. V. Wijk, 2009, Seismic Wave Attenuation in Carbonates: Journal of Geophysical Research, **114**.

Aki, K., and P. G. Richards, 1980, Quantitative Seismology: Theory and Methods, Volume I: W.H. Freeman and Company.

Alkhalifah, T., 1995, Gaussian beam depth migration for anisotropic media: Geophysics, **60**, 1474–1484.

Aminzadeh, F., N. Burkhard, J. Long, T. Kunz, and P. Duclos, 1996, Three dimensional SEG/EAGE models - an update: The Leading Edge, **15**, 131–134.

Aster, R. C., B. Borchers, and C. H. Thurber, 2005, Parameter Estimation and Inverse Problems: Elsevier.

Barnes, C., 2010, Anisotropic anelastic full waveform inversion: Application to North Sea offset VSP data: 80th Annual International Meeting, SEG, Expanded Abstracts.

Batzle, M., R. Hofmann, and M. Prasad, 2005, Seismic Attenuation: Observations and Mechanisms: 75th Annual International Meeting, SEG, Expanded Abstracts, 1565–1568.

Behura, J., M. Batzle, R. Hofmann, and J. Dorgan, 2007, Heavy oils: Their shear story: Geophysics, **72**, no. 5, E175–E183.

Behura, J., and I. Tsvankin, 2009a, Estimation of interval anisotropic attenuation from reflection data: Geophysics, **74**, no. 6, A69–A74.

——— 2009b, Reflection coefficients in attenuative anisotropic media: Geophysics, **74**, WB193–WB202.

——— 2009c, Role of the inhomogeneity angle in anisotropic attenuation analysis: Geophysics, **74**, no. 5, WB177–WB191.

Behura, J., I. Tsvankin, E. Jenner, and A. Calvert, 2012, Estimation of interval velocity and attenuation ansiotropy from reflection data at the Coronation Field: The Leading Edge, **31**.

Blanchard, T., M. van der Baan, R. Clark, and B. Kurmashov, 2010, P-wave attenuation as an additional tool for monitoring CO_2 injection sites: 80th Annual International Meeting, SEG, Expanded Abstracts, 4252–4256.

Bleistein, N., 1984, Mathematical Methods for Wave Phenomena: Academic Press.

——— 1986, Two-and-one-half dimensional in-plane wave propagation: Geophysical Prospecting, **34**, 686–703.

——— 2008, Seismic wavefields in layered isotropic media (course notes): CWP, Colorado School of Mines (http://www.cwp.mines.edu/norm/ShrtCrse).

——— 2012, Saddle point contribution for an n-fold complex-valued integral: CWP Research Report 741.

Borcherdt, R. D., 2009, Viscoelastic Waves in Layered Media: Cambridge University Press.

Bulant, P., 1996, Amplitude and phase data inversion for phase velocity anomalies in the Pacific Ocean basin: Pure and Applied Geophysics, **148**, 421–447.

——— 2002, Sobolev scalar products in the construction of velocity models - application to model Hess and to SEG/EAGE Salt Model: Pure and Applied Geophysics, **159**, 1487–1506.

Carcione, J., 1990, Wave propagation in anisotropic linear viscoelastic media: theory and simulated wavefields: Geophysical Journal International, **101**, 739–750.

——— 1992, Anisotropic Q and velocity dispersion of finely layered media: Geophysical Prospecting, **40**, 761–783.

——— 2007, Wave Fields in Real Media. Theory and numerical simulation of wave propagation in anisotropic, anelastic, porous and electromagnetic media.: Elsevier.

——— 2011, A generalization of the Fourier pseudospectral method: Geophysics, **76**.

Cavalca, M., R. Fletcher, and M. Riedel, 2013, Q-compensation in complex media-Ray-based and wavefield extrapolation approaches: 83rd Annual International Meeting, SEG, Expanded Abstracts, 3831–3835.

Červený, V., 1985, Gaussian beam synthetic seismograms: Journal of Geophysics, **58**, 44–72.

——— 2001, Seismic ray theory: Cambridge University Press.

Červený, V., L. Klimeš, and I. Pšenčik, 2008, Attenuation vector in heterogeneous, weakly dissipative, anisotropic media: Geophysical Journal International, **175**, 346–355.

Červený, V., and I. Pšenčik, 2005, Plane waves in viscoelastic anisotropic media – I. Theory: Geophysical Journal International, **161**, 197–212.

——— 2008, Quality factor Q in dissipative anisotropic media: Geophysics, **73**, T63–T75.

——— 2009, Perturbation Hamiltonians in heterogeneous anisotropic weakly dissipative media: Geophysical Journal International, **178**, 939–949.

——— 2010, Gaussian beams in inhomogeneous anisotropic layered structures: Geophysical Journal International, **180**, 798–812.

Chapman, C., 2004, Fundamentals of Seismic Wave Propagation: Cambridge University Press.

Chapman, M., 2003, Frequency-dependent anisotropy due to meso-scale fractures in the presence of equant porosity: Geophysical Prospecting, **51**, 369–379.

Chichinina, T., I. Obolentseva, L. Gilk, B. Bobrov, and G. Ronquillo-Jarillo, 2009, Attenuation anisotropy in the linear-slip model: Interpretation of physical modeling data: Geophysics, **74**, no.5, WB165–WB176.

Clark, R. A., P. M. Benson, A. J. Carter, and C. A. G. Moreno, 2009, Anisotropic P-wave attenuation measured from a multi-azimuth surface seismic reflection survey: Geophysical Prospecting, **57**, 835–845.

Das, A., and M. Batzle, 2010, Frequency dependent elastic properties and attenuation in heavyoil sands: comparison between measured and modeled data Frequency dependent elastic properties and attenuation in heavy-oil sands: comparision between measured and modeled data: 80th Annual International Meeting, SEG, Expanded Abstracts, 2547–2551.

Dasios, A., T. Astin, and C. McCann, 2001, Compressional wave Q estimation from full-waveform sonic data: Geophysical Prospecting, **49**, 353–373.

De, G. S., D. F. Winterstein, and M. A. Meadows, 1994, Comparision of P- and S-wave velocities and Q's from VSP and sonic log data: Geophysics, **59**, 1512–1529.

Dellinger, J., S. Brandsberg-Dahl, R. Clarke, and L. Thomsen, 2002, Alford rotation after tensor migration: 72nd Annual International Meeting, SEG, Expanded Abstracts, 982–985.

Dewangan, P., and I. Tsvankin, 2006, Velocity-independent layer stripping of PP and PS reflection traveltimes: Geophysics, **71**, no. 4, U59–U65.

Draper, N., and H. Smith, 1981, Applied Regression Analysis: John Wiley and Sons, Second edition.

Gaiser, J. E., 1997, 3-D converted shear wave rotation with layer stripping: U.S. Patent 5,610,875.

Gajewski, D., 1993, Radiation from point sources in general anisotropic media: Geophysical Journal International, **113**, 299–317.

Gajewski, D., and I. Pšenčik, 1992, Vector wavefield for weakly attenuating anisotropic media by the ray method: Geophysics, **57**, 27–38.

Grechka, V., and P. Dewangan, 2003, Generation and processing of pseudo-shear-wave data: Theory and case study: Geophysics, **68**, 1807–1816.

Grechka, V., and A. Duchkov, 2011, Narrow-angle representations of the phase and group velocities and their applications in anisotropic velocity-model building for microseismic monitoring: Geophysics, **76**, WC127–WC142.

Grechka, V., and I. Tsvankin, 2002, PP + PS = SS: Geophysics, **67**, 1961–1971.

Hale, D., 1992, Computational aspects of Gaussian beam migration: CWP Research Report 121.

Hanyga, A., and M. Seredyňska, 2000, Ray tracing in elastic and viscoelastic media: Pure and Applied Geophysics, **157**, 679–717.

Hearn, D. J., and E. S. Krebes, 1990, On computing ray-synthetic seismograms for anelastic media using complex rays: Geophysics, **55**, 422–432.

Hestholm, S., 2002, Composite memory variable velocity-stress viscoelastic modelling: Geophysical Journal International, **148**.

Hill, R. N., 1990, Gaussian beam migration: Geophysics, **55**, 1416–1428.

Hofmann, R., 2006, Frequency dependent elastic and anelastic properties of clastic rocks: PhD thesis, Colorado School of Mines.

Horn, R. A., and C. R. Johnson, 1990, Matrix analysis: Cambridge University Press.

Hustedt, B., and R. A. Clark, 1999, Source/receiver array directivity effects on marine seismic attenuation measurements: Geophysical Prospecting, **47**, 1105–1119.

Jakobsen, M., and M. Chapman, 2009, unified theory of global flow and squirt flow in cracked porous media: Geophysics, **74**, no. 2, WA65–WA76.

Johnston, D. H., and M. Toksöz, 1981, Seismic wave attenuation. Geophysics reprint series: Society of Exploration Geophysicists.

Kamei, R., and R. G. Pratt, 2013, Inversion strategies for visco-acoustic waveform inversion: Geophysical Journal International, **194**, 859–884.

Kjartannson, E., 1979, Constant Q-Wave Propagation and Attenuation: Journal of Geophysical Research, **84**, 4737–4748.

Klimentos, T., 1995, Attenuation of P- and S-waves as a method of distinguishing gas and condensate from oil and water: Geophysics, **60**, 447–458.

Klimeš, L., 2002, Second-order and higher-order perturbations of travel time in isotropic and anisotropic media: Studia Geophysica et Geodaetica, **46**, 213–248.

Krantz, S. G., and H. R. Parks, 2002, The implicit function theorem: Springer.

Krebes, E. S., and L. H. T. Le, 1994, Inhomogeneous plane waves and cylindrical waves in anisotropic anelastic media: Journal of Geophysical Research, **99**, 899–919.

Liu, E., M. Chapman, I. Varela, X. Li, J. H. Queen, and H. Lynn, 2007, Velocity and attenuation anisotropy: Implication of seismic fracture charecterizations: The Leading Edge, **26**, 1170–1174.

Lynn, H. B., 2004, The winds of change: Anisotropic rocks-their preferred direction of fluid flow and their associated seismic signatures-Part 1: The Leading Edge, 1156–1162.

Mallick, S., and N. L. Frazer, 1990, Computation of Synthetic Seismograms for Stratified Azimuthally Anisotropic Media: Journal of Geophysical Research, **95**, 8513–8526.

Matheney, M. P., and R. L. Nowack, 1995, Seismic attenuation values obtained from instantaneous-frequency matching and spectral ratios: Geophysical Journal International, **123**, 1–15.

Maultzsch, S., M. Chapman, E. Liu, and X.-Y. Li, 2007, Modelling and analysis of attenuation anisotropy in multi-azimuth VSP data from Clair field: Geophysical Prospecting, **55**, 627–642.

Prasad, M., and A. Nur, 2003, Velocity and Attenuation Anisotropy in Reservoir Rocks: 73rd Annual International Meeting, SEG, Expanded Abstracts, 1652–1655.

Pratt, R. G., F. Hou, K. Bauer, and M. Weber, 2004, Waveform tomography images of velocity and inelastic attenuation from the Mallik 2002 Crosshole Seismic Surveys, Scientific results from the Malik 2002 Gas Hydrate Production Research Well Program, Mackenzie Delta, North Territories, Canada: Geological Survey of Canada, Bulletin, **585**.

Pšenčik, I., and T. N. Teles, 1996, Point Source Radiation in Inhomogeneous Anisotropic Structures: Pure and Applied Geophysics, **148**, 591–623.

Quan, Y., and J. M. Harris, 1997a, Seismic attenuation tomography using the frequency shift method: Geophysics, **62**, 895–905.

——— 1997b, Seismic attenuation tomography using the frequency shift method: Geophysics, **62**, 895–905.

Reine, C. A., R. A. Clark, and M. van der Baan, 2009a, Interval-Q Measurements from Surface Seismic Data Using a Robust Prestack Inversion Algorithm: 71st EAGE Conference & Exhibition.

Reine, C. A., M. van der Baan, and R. Clark, 2009b, The robustness of seismic attenuation measurements using fixed- and variable-window time-frequency transforms: Geophysics, **74**, WA123–WA135.

Rüger, A., 1997, P-wave reflection coefficients for transversely isotropic models with vertical and horizontal axis of symmetry: Geophysics, **62**, 713–722.

Ruud, B. O., and S. Hestholm, 2005, Modeling seismic waves in orthorhombic, viscoelastic media by finite-differences: 75th Annual International Meeting, SEG, Expanded Abstracts.

Sarkar, D., and I. Tsvankin, 2004, Migration velocity analysis in factorized VTI media: Geophysics, **69**, 708–713.

Scales, J. A., and A. Gersztenkorn, 1988, Robust methods in inverse theory: Inverse Problems, **4**, 1071–1091.

Schmidt, H., and G. Tango, 1986, Efficient global matrix approach to the computation of synthetic seismograms: Geophysical Journal of the Royal Astronomical Society, **84**, 331–359.

Shekar, B., and I. Tsvankin, 2011, Estimation of shear-wave interval attenuation from mode-converted data: Geophysics, **76**, no. 6, D11–D19.

——— 2012, Attenuation analysis for heterogeneous transversely isotropic media: 82nd Annual International Meeting, SEG, Expanded Abstracts.

Simmons, J. L., 2009, Converted-wave splitting estimation and compensation: Geophysics, **74**, D37–D48.

Thomson, C. J., 1997, Complex rays and wave packets for decaying signals in inhomogeneous, anisotropic and anelastic media: Studia Geophysica et Geodaetica, **41**, 345–381.

Tsvankin, I., 1995, Seismic wavefields in layered isotropic media (course notes): Samizdat Press (http://samizdat.mines.edu/).

——— 1997, Anisotropic parameters and P-wave velocity for orthorhombic media: Geophysics, **62**, 1292–1309.

——— 2005, Seismic Signatures and Analysis of Reflection Data in Anisotropic Media: Elsevier.

——— 2012, Seismic signatures and analysis of reflection data in anisotropic media: Society of Exploration Geophysicists, third edition.

Tsvankin, I., and E. M. Chesnokov, 1990, Synthesis of body wave seismograms from point sources in anisotropic media: Journal of Geophysical Research, **95**, 11317–11331.

Tsvankin, I., and V. Grechka, 2011, Seismology of azimuthally anisotropic media and seismic fracture characterization: SEG.

Vasconcelos, I., and E. Jenner, 2005, Estimation of azimuthally varying attenuation from wide-azimuth P-wave data: 75th Annual International Meeting, SEG, Expanded Abstracts, 123–126.

Vasconcelos, I., and I. Tsvankin, 2006, Nonhyperbolic moveout inversion of wide-azimuth P-wave data for orthorhombic media: Geophysical Prospecting, **54**, 535–552.

Vavryčuk, V., 2007, Asymptotic Green's function in homogeneous anisotropic viscoelastic media: Proceedings of The Royal Society A, **463**, 2689–2707.

Wang, C. Y., and J. D. Achenbach, 1994, Elastodynamic fundamental solutions for anisotropic solids: Geophysical Journal International, **118**, 384–392.

Wang, X., and I. Tsvankin, 2009, Estimation of interval anisotropy parameters using velocity-independent layer stripping: Geophysics, **74, no. 5**, WB117–WB127.

Xin, K., B. Hung, S. Birdus, and J. Sun, 2008, 3-D tomographic amplitude inversion for compensating amplitude attenuation in the overburden: 78th Annual International Meeting, SEG, Expanded Abstracts, 3239–3243.

Xu, T., and G. A. McMechan, 1998, Efficient 3-D viscoelastic modeling with application to near-surface land seismic data: Geophysics, **63**, 601–612.

Xu, X., and I. Tsvankin, 2008, Moveout-based geometrical-spreading correction for PS-waves in layered anisotropic media: Journal of Geophysics and Engineering, **5**, 195–202.

Yomogida, K., and K. Aki, 1987, Amplitude and phase data inversion for phase velocity anomalies in the Pacific Ocean basin: Geophysical Journal of the Royal Astronomical Society, **88**, 161–204.

Zhu, Y., 2006, Seismic wave propagation in attenuative anisotropic media: PhD thesis, Colorado School of Mines.

Zhu, Y., and I. Tsvankin, 2006, Plane-wave propagation in attenuative transversely isotropic media: Geophysics, **71**, no. 2, T17–T30.

——— 2007, Plane-wave attenuation anisotropy in orthorhombic media: Geophysics, **72**, no.1, D9–D19.

Zhu, Y., I. Tsvankin, P. Dewangan, and K. V. Wijk, 2007a, Physical modeling and analysis of P-wave attenuation anisotropy in transversely isotropic media: Geophysics, **72**, no. 1, D1–D7.

Zhu, Y., I. Tsvankin, and I. Vasconcelos, 2007b, Effective attenuation anisotropy of thin-layered media: Geophysics, **72**, no.5, D93–D106.

APPENDIX A

EXACT GREEN'S FUNCTION FOR ATTENUATIVE ANISOTROPIC MEDIA

The elastodynamic equation in the frequency-wavenumber domain for a homogeneous, attenuative, anisotropic medium can be written as (Carcione, 2007; Zhu, 2006):

$$(\tilde{a}_{ijkl}(\omega)k_j k_l - \omega^2\delta_{ik})\,\tilde{U}_k(\mathbf{k},\omega) = \tilde{f}_i(\mathbf{k},\omega), \tag{A.1}$$

where ω is the frequency, $\tilde{a}_{ijkl}$ are the components of the density-normalized stiffness tensor, k_j are the wavenumbers, $\tilde{\mathbf{U}}$ is the displacement vector, and $\tilde{f}(\mathbf{k},\omega)$ is the body force per unit volume (source). Summation over repeated indices (changing from 1 to 3) is implied.

The frequency-domain displacement can be found as the triple Fourier integral:

$$\tilde{u}_k(\mathbf{x},\omega) = \frac{1}{(2\pi)^3}\int_{-\infty}^{\infty} \tilde{U}_k(k,\omega)\, e^{ik_j x_j}\mathrm{d}\mathbf{k}, \tag{A.2}$$

where $\mathrm{d}\mathbf{k} = \mathrm{d}k_1\,\mathrm{d}k_2\,\mathrm{d}k_3$, and

$$\tilde{U}_k(k,\omega) = \frac{\tilde{B}_{ki}\,\tilde{f}_i(k_j,\omega)}{\det\tilde{\mathbf{D}}}. \tag{A.3}$$

The matrix $\tilde{\mathbf{D}}$ ($\tilde{D}_{ki} = \tilde{a}_{ijkl}k_j k_l - \omega^2\delta_{ik}$) with cofactors $\tilde{B}_{ki}$ is closely related to the Christoffel matrix. The source in equation A.1 can be defined as a point impulsive force applied at location $\mathbf{x}_0$ parallel to the x_n-axis:

$$\tilde{f}_i(\omega,k_j) = \delta_{in}\, e^{-i\,k_j\,x_j^0}\,. \tag{A.4}$$

The particle displacement from this source is the Green's function G_{kn}:

$$G_{kn}(\mathbf{x},\mathbf{x}^0,\omega) = \frac{1}{(2\pi)^3}\int_{-\infty}^{\infty} \frac{\tilde{B}_{ki}\,\delta_{in}}{\det\tilde{\mathbf{D}}}\, e^{ik_j(x_j-x_j^0)}\,\mathrm{d}\mathbf{k}. \tag{A.5}$$

Following Červený (2001), we rotate the coordinate frame to align the x_3-axis with the source-receiver direction. Equation A.5 in the rotated coordinate frame now reads:

$$G_{kn}(\mathbf{x},\mathbf{x}^0,\omega) = \frac{1}{(2\pi)^3}\,,\int_{-\infty}^{\infty} \frac{\tilde{B}_{ki}\,\delta_{in}}{\det\tilde{\mathbf{D}}}\, e^{ik_3 R}\,\mathrm{d}\mathbf{k}, \tag{A.6}$$

where $R = \sqrt{[(x_1 - x_1^0)^2 + (x_2 - x_2^0)^2 + (x_3 - x_3^0)^2]}$ is the source-receiver distance. The Bond transformation has to be applied to the stiffness tensor to account for the coordinate rotation. Note that the components of the wave vector k_j also correspond to the rotated coordinate frame. For convenience, here we retain the symbols introduced in the previous equations, which were defined in the unrotated coordinate frame.

Since $R > 0$, the integral over k_3 in equation A.6 can be extended into the complex plane by representing the vertical wavenumber as $\tilde{k}_3 = \mathrm{Re}\, k_3 + i\, \mathrm{Im}\, k_3$. The closed contour includes the real axis and a semicircle with an infinitely large radius in the upper half-plane. The integral can then be evaluated by the residue theorem (i.e., by computing the residues at the poles), as described in Aki and Richards (1980), Tsvankin (1995), and Tsvankin and Chesnokov (1990). The poles correspond to the roots of the Christoffel equation for k_3:

$$\det \tilde{\mathbf{D}} = \det[\tilde{a}_{ijkl} k_j k_l - \omega^2 \delta_{ik}] = 0. \tag{A.7}$$

Equation A.7 is a sixth-order polynomial in k_3 with complex coefficients that can have at most six distinct roots corresponding to the up- and downgoing P-, S_1- and S_2-waves.

For homogeneous (non-decaying) waves in unbounded nonattenuative media, the roots of k_3 lie on the real k_3-axis. Then the integral in equation A.6 can be evaluated by introducing small attenuation, moving the roots to the complex plane, and applying the residue theorem (Tsvankin, 1995). Alternatively, the integral over k_3 can be evaluated using Cauchy's principal value (Bleistein, 1984).

In the presence of attenuation, the roots of equation A.7 lie away from the real axis. The pole $\tilde{k}_3^s = \tilde{k}_3(k_1, k_2)$, which corresponds to a certain mode (e.g., P-waves) and is located inside the integration contour yields the residue for that mode. Hence, the integral over k_3 in equation A.6 can be evaluated using the residue at the pole, and the Green's function is expressed as the following double integral:

$$G_{kn}(\mathbf{x}, \mathbf{x}^0, \omega) = \frac{i}{(2\pi)^2} \int_{-\infty}^{\infty} \int_{-\infty}^{\infty} \Big[\frac{\tilde{B}_{kn}}{\partial(\det \tilde{\mathbf{D}})/\partial k_3} \Big]_{k_3 = \tilde{k}_3^r} e^{i \tilde{k}_3^r R \hat{x}_3} \, \mathrm{d}k_1 \, \mathrm{d}k_2. \tag{A.8}$$

Substituting $k_j = \omega\, p_j$, where p_j denotes the components of the slowness vector, yields $\det \tilde{\mathbf{D}} = \omega^6 \det(\tilde{\Gamma}_{ik} - \delta_{ik})$, where $\tilde{\Gamma}_{ik} = \tilde{a_{ijkl}} p_j p_l$. The cofactors of $\tilde{\mathbf{\Gamma}} - \mathbf{I}$ ($\mathbf{I}$ is the identity matrix) are denoted by $\tilde{S}_{kn}$, and $\tilde{B}_{kn} = \omega^4 \tilde{S}_{kn}$. Equation A.8 can then be written as

$$G_{kn}(\mathbf{x}, \mathbf{x}^0, \omega) = \frac{i\omega}{(2\pi)^2} \int_{-\infty}^{\infty} \int_{-\infty}^{\infty} \Big[\frac{\tilde{S}_{kn}}{\partial[\det(\tilde{\mathbf{\Gamma}} - \mathbf{I})]/\partial p_3} \Big]_{p_3 = \tilde{p}_3^r} e^{i\tilde{p}_3^r}\, \mathrm{d}p_1\, \mathrm{d}p_2. \tag{A.9}$$

APPENDIX B

PROPERTIES OF THE CHRISTOFFEL MATRIX IN ATTENUATIVE ANISOTROPIC MEDIA

Here, we summarize the properties of the eigenvalues and eigenvectors of the Christoffel matrix in attenuative anisotropic media. These properties are used in the asymptotic and perturbation analysis presented in the main text. The results presented in this appendix are based on section 4.4 of Horn and Johnson (1990), which contains a discussion on complex symmetric matrices.

The components of the Christoffel matrix $\tilde{\mathbf{\Gamma}}$ in attenuative media are given by (see the main text):

$$\tilde{\Gamma}_{ik} = \tilde{a}_{ijkl}\, \tilde{p}_j\, \tilde{p}_l, \tag{B.1}$$

where $\tilde{a}_{ijkl}$ is the density-normalized complex stiffness tensor and $\tilde{\mathbf{p}}$ is the complex-valued slowness vector.

The eigenvector-eigenvalue problem for matrix $\tilde{\mathbf{\Gamma}}$ can be written as:

$$\tilde{\mathbf{\Gamma}}\, \tilde{\mathbf{V}} = \tilde{\mathbf{V}}\, \tilde{\mathbf{\Lambda}}, \tag{B.2}$$

where $\tilde{\mathbf{\Lambda}}$ is the diagonal matrix of the eigenvalues and the columns of $\tilde{\mathbf{V}}$ contain the corresponding eigenvectors. The matrix $\tilde{\mathbf{V}}$ is nonsingular (Horn and Johnson, 1990), so

$$\tilde{\mathbf{\Gamma}} = \tilde{\mathbf{V}}\, \tilde{\mathbf{\Lambda}}\, \tilde{\mathbf{V}}^{-1}, \tag{B.3}$$

$$\tilde{\mathbf{\Lambda}} = \tilde{\mathbf{V}}^{-1}\, \tilde{\mathbf{\Gamma}}\, \tilde{\mathbf{V}}. \tag{B.4}$$

If the eigenvalues of the Christoffel matrix are distinct, the matrix $\tilde{\mathbf{V}}$ satisfies

$$\tilde{\mathbf{V}}^{\mathrm{T}}\, \tilde{\mathbf{V}} = \tilde{\mathbf{D}}, \tag{B.5}$$

where $\tilde{\mathbf{D}}$ is a diagonal matrix. The Christoffel matrix can be diagonalized in the following way:

$$\tilde{\mathbf{\Gamma}} = \tilde{\mathbf{G}}\,\tilde{\mathbf{\Lambda}}\,\tilde{\mathbf{G}}^{\mathrm{T}} \tag{B.6}$$

$$\tilde{\mathbf{\Lambda}} = \tilde{\mathbf{G}}^{\mathrm{T}}\,\tilde{\mathbf{\Gamma}}\,\tilde{\mathbf{G}} \tag{B.7}$$

with

$$\tilde{\mathbf{G}} = \tilde{\mathbf{V}}\,\tilde{\mathbf{D}}^{-\,1/2}. \tag{B.8}$$

The matrix $\tilde{\mathbf{G}}$ is complex orthonormal, i.e., $\tilde{\mathbf{G}}^{\mathrm{T}}\,\tilde{\mathbf{G}} = \tilde{\mathbf{G}}\,\tilde{\mathbf{G}}^{\mathrm{T}} = \mathbf{I}$.

In purely elastic media $\tilde{\mathbf{D}} = \mathbf{I}$, and consequently $\tilde{\mathbf{V}}^{\mathrm{T}} = \tilde{\mathbf{V}}^{-1}$ and $\tilde{\mathbf{V}} = \tilde{\mathbf{G}}$. The eigenvector matrix $\tilde{\mathbf{V}}$ then includes the polarization vectors of the three wave modes. Choosing the columns of $\tilde{\mathbf{G}}$ as the polarization vectors helps extend expressions derived for elastic media to attenuative models.

Next, we provide expressions for quantities related to the complex Christoffel matrix used throughout this paper. The results below are based on sections 3.6.2 and 4.14.1 of Červený (2001), with the real-valued stiffness coefficients and slowness vector replaced by the corresponding complex-valued quantities. We denote the eigenvalues (elements of $\tilde{\mathbf{\Lambda}}$) by $\tilde{\lambda}^{(1)}$, $\tilde{\lambda}^{(2)}$, and $\tilde{\lambda}^{(3)}$, and the corresponding polarization vectors (columns of $\tilde{\mathbf{G}}$) by $\tilde{\mathbf{g}}^{(1)}$, $\tilde{\mathbf{g}}^{(2)}$, and $\tilde{\mathbf{g}}^{(3)}$. Using equation B.7, the eigenvalue $\tilde{\lambda}^{(1)}$ can be found as

$$\lambda^{(1)} = \tilde{g}_i^{(1)}\,\tilde{a}_{ijkl}\,\tilde{p}_j\,\tilde{p}_l\,\tilde{g}_k^{(1)}. \tag{B.9}$$

Then the derivatives $\partial\tilde{\lambda}^{(1)}/\partial\tilde{p}_n$ and $\partial^2\tilde{\lambda}^{(1)}/\partial\tilde{p}_n\partial\tilde{p}_q$ take the form:

$$\frac{\partial\tilde{\lambda}^{(1)}}{\partial\tilde{p}_n} = \frac{\partial\tilde{\Gamma}_{ik}}{\partial\tilde{p}_n}\,\tilde{g}_j^{(1)}\,\tilde{g}_k^{(1)}, \tag{B.10}$$

$$\frac{\partial^2\tilde{\lambda}^{(1)}}{\partial\tilde{p}_n\partial\tilde{p}_q} = \frac{\partial^2\tilde{\Gamma}_{ik}}{\partial\tilde{p}_n\partial\tilde{p}_q}\,\tilde{g}_i^{(1)}\,\tilde{g}_k^{(1)} + 2\,\frac{\partial\tilde{\Gamma}_{ik}}{\partial\tilde{p}_n}\,\tilde{g}_i^{(1)}\,\frac{\partial\tilde{g}_k^{(1)}}{\partial\tilde{p}_q}, \tag{B.11}$$

$$\frac{\partial\tilde{\Gamma}_{ik}}{\partial\tilde{p}_n} = (\tilde{a}_{inqk} + \tilde{a}_{iqkn})\,\tilde{p}_q, \tag{B.12}$$

$$\frac{\partial^2 \tilde{\Gamma}_{ik}}{\partial \tilde{p}_n \partial \tilde{p}_q} = \tilde{a}_{inqk} + \tilde{a}_{iqkn}, \tag{B.13}$$

and

$$\frac{\partial \tilde{g}_k^{(1)}}{\partial \tilde{p}_q} = \Big[\frac{1}{\tilde{\lambda}^{(1)} - \tilde{\lambda}^{(2)}} \frac{\partial \Gamma_{in}}{\partial \tilde{p}_q} \tilde{g}_i^{(2)} \tilde{g}_n^{(1)}\Big] \tilde{g}_k^{(2)} + \Big[\frac{1}{\tilde{\lambda}^{(1)} - \tilde{\lambda}^{(3)}} \frac{\partial \tilde{\Gamma}_{in}}{\partial \tilde{p}_q} \tilde{g}_i^{(3)} \tilde{g}_n^{(1)}\Big] \tilde{g}_k^{(3)}. \tag{B.14}$$

From equations B.9 and B.10 it follows that

$$\tilde{p}_n \frac{\partial \lambda^{(1)}}{\partial \tilde{p}_n} = 2\,\lambda^{(1)}. \tag{B.15}$$

Finally, the product $\tilde{g}_j^{(1)}\,\tilde{g}_k^{(1)}$ can be expressed as:

$$\tilde{g}_j^{(1)}\,\tilde{g}_k^{(1)} = \frac{\tilde{S}_{jk}}{\mathrm{Tr}\,[\tilde{\mathbf{S}}]}, \tag{B.16}$$

where $\tilde{S}_{jk}$ represent the components of the cofactor matrix of $[\tilde{\mathbf{\Gamma}} - \tilde{\lambda}^{(1)}\,\mathbf{I}]$, and $\mathrm{Tr}\,[\tilde{\mathbf{S}}]$ is the trace of the cofactor matrix.

APPENDIX C

PERTURBATION ANALYSIS OF THE INHOMOGENEITY ANGLE

In this section, we present expressions for the propagation and attenuation vectors (and, hence, the inhomogeneity angle) in homogeneous, attenuative, anisotropic media using the method of perturbation Hamiltonians introduced by Červený and Pšenčik (2009). We also derive the conditions under which the inhomogeneity angle vanishes.

The second-order partial derivative in equation 4.31 can be evaluated using quadratures along the reference rays, as shown by Klimeš (2002) and Červený and Pšenčik (2009):

$$\frac{\partial^2 \tau}{\partial x_i \, \partial \alpha} = \tilde{T}_k(\alpha) \, [Q_{ki}^{\mathrm{ray}}]^{-1}, \tag{C.1}$$

with the vector $\mathbf{T}(\alpha)$ given by

$$\tilde{T}_K(\alpha) = \tilde{T}_K^0(\alpha) + \tau \, \tilde{\mathcal{W}}_i \, P_{iK}^{\mathrm{ray}}, \quad K = 1, 2, \tag{C.2}$$

$$\tilde{\mathcal{W}}_i = \Big(\frac{\partial \tilde{\mathcal{H}}}{\partial p_i} - \frac{\partial \mathcal{H}^0}{\partial p_i} \Big), \tag{C.3}$$

$$\tilde{T}_3(\alpha) = \mathcal{H}^0 - \tilde{\mathcal{H}}. \tag{C.4}$$

The index K changes from 1 to 2, and the lower-case index k from 1 to 3. The real-valued matrices Q_{ik}^{ray} (not to be confused with the quality-factor matrix) and P_{ik}^{ray} are computed using dynamic ray tracing in the reference elastic medium:

$$\begin{aligned} Q_{ik}^{\mathrm{ray}} &= \frac{\partial x_i}{\partial \gamma_k}, \\ P_{ik}^{\mathrm{ray}} &= \frac{\partial p_i^0}{\partial \gamma_k}; \end{aligned} \tag{C.5}$$

γ_k denotes a certain "ray parameter" (e.g., the initial phase angle or the traveltime along the ray). In equation C.2 the initial conditions $\tilde{T}^0_K(\alpha)$, are set to zero for a point source; for plane-wave propagation $\tilde{T}^0_K(\alpha)$ may be chosen arbitrarily (Klimeš, 2002).

We now derive the conditions under which the inhomogeneity angle in homogeneous media vanishes. Substituting equations 4.28 and 4.29 into equation C.3 yields:

$$\tilde{\mathcal{W}}_i = \tilde{a}_{ijkl}\, p_k\, \tilde{g}_j\, \tilde{g}_l - a^R_{ijkl}\, p_k\, g_j\, g_l. \tag{C.6}$$

For weakly dissipative media, we can use the approximation $\tilde{\mathbf{g}} \approx \mathbf{g}$ and reduce equation C.6 to

$$\tilde{\mathcal{W}}_i = -\,i\, a^I_{ijkl}\, p_k\, g_j\, g_l. \tag{C.7}$$

For the special case of identical Q_{ij} components (i.e., $a^I_{ijkl} = a^R_{ijkl}/Q$), we have

$$\tilde{\mathcal{W}}_i = -\,i\, \frac{a^R_{ijkl}}{Q}\, p_k\, g_j\, g_l = -\,i\, \frac{\mathcal{U}_i}{Q}, \tag{C.8}$$

where $\mathcal{U}_i$ are the components of the group-velocity vector in the reference elastic medium. Substituting equation C.8 into equation C.2, we obtain

$$\tilde{T}_{K\alpha}(\gamma_3) = -\,i\,(\gamma_3 - \gamma^0_3)\, \frac{\mathcal{U}_i}{Q}\, P^{\text{ray}}_{iK} = 0, \quad K = 1, 2, \tag{C.9}$$

because the group-velocity vector is orthogonal to the first two columns of the matrix $\mathbf{P}^{\text{ray}}$ and $\mathcal{U}_i\, P_{iK} = 0$ (Červený, 2001). Equations 4.32 and 4.33 for $\mathbf{p}^R$ and $\mathbf{p}^I$ then take the form:

$$p^R_i = p^0_i + \text{Re}\,[\tilde{T}_{3\alpha}]\, p^0_i, \tag{C.10}$$

and

$$p^I_i = \text{Im}\,[\tilde{T}_{3\alpha}]\, p^0_i, \tag{C.11}$$

where $p^0_i = [Q^{\text{ray}}_{3i}]^{-1}$ (Červený, 2001). From equations C.10 and C.11, it follows that both $\mathbf{p}^R$ and $\mathbf{p}^I$ are parallel to $\mathbf{p}^0$. Hence, the inhomogeneity angle vanishes in the case of identical Q components, i.e., when the attenuation coefficients of all three modes are equal and isotropic. Note that the velocity function may still be angle-dependent (anisotropic). Further, the inhomogeneity angle also vanishes for isotropic velocity and attenuation functions with different values of the quality factor for P- and S-waves. This can be proved by considering the expression for the Hamiltonian in isotropic media.

APPENDIX D

DYNAMIC RAY TRACING AND GAUSSIAN BEAMS IN ANISOTROPIC MEDIA

In this appendix, we breifly review dynamic ray tracing in anisotropic media and introduce the quantities necessary for the construction of Gaussian beams.

The eikonal equation in elastic, anisotropic, heterogenous media can be written as (Červený, 2001):

$$G(x_i, p_i) = 1, \tag{D.1}$$

where x_i are the spatial coordinates and p_i are the components of the slowness vector. The solutions of equation D.1 represent the eigenvalues of the Christoffel equation:

$$\det\left[\Gamma_{ik} - G\,\delta_{ik}\right] = 0, \tag{D.2}$$

where $\Gamma_{ik} = a_{ijkl}\,p_j\,p_l$ are the components of the Christoffel matrix and a_{ijkl} form the density-normalized stiffness tensor.

The kinematic ray-tracing equations are given by (Červený, 2001):

$$\frac{\mathrm{d}x_i}{\mathrm{d}\tau} = \frac{1}{2}\frac{\partial G}{\partial p_i}, \tag{D.3}$$

$$\frac{\mathrm{d}p_i}{\mathrm{d}\tau} = \frac{1}{2}\frac{\partial G}{\partial x_i}, \tag{D.4}$$

where τ represents the traveltime (eikonal) along the ray.

The dynamic ray-tracing system in ray-centered coordinates can be represented as (Červený, 2001):

$$\frac{\mathrm{d}P_{NI}}{\mathrm{d}\tau} = -C_{NM}\,Q_{MI} - D_{NM}\,P_{MI}, \tag{D.5}$$

$$\frac{\mathrm{d}Q_{NI}}{\mathrm{d}\tau} = A_{NM}\,Q_{MI} + B_{NM}\,P_{MI}, \tag{D.6}$$

where the indices N, M, and I vary from 1 to 2. Explicit expressions for the matrices $\mathbf{A}$, $\mathbf{B}$, $\mathbf{C}$, and $\mathbf{D}$ can be found in Červený (2001). The matrices P_{MI} and Q_{NI} are defined as

$$P_{NI} = \frac{\partial p_N}{\partial \gamma_I} \tag{D.7}$$

$$Q_{NI} = \frac{\partial q_N}{\partial \gamma_I}, \tag{D.8}$$

where γ_I is a certain "ray parameter" (e.g., the phase angle of the ray), q_N are the coordinates tangent to the wavefront, and p_N denotes the slowness vector in the ray-centered coordinate system:

$$p_N = \frac{\partial \tau}{\partial q_N}. \tag{D.9}$$

The columns of $\mathbf{P}$ are unit vectors tangent to the wavefront, and the columns of $\mathbf{Q}$ are unit vectors tangent to the slowness surface. The 3×3 matrices $\mathbf{P}^x$ and $\mathbf{Q}^x$ correspond to $\mathbf{P}$ and $\mathbf{Q}$ in Cartesian coordinates (Červený, 2001):

$$P^x_{ik} = \frac{\partial p_i}{\partial \gamma_k}. \tag{D.10}$$

$$Q^x_{ik} = \frac{\partial x_i}{\partial \gamma_k}, \tag{D.11}$$

The first two columns of $\mathbf{P}^x$ and $\mathbf{Q}^x$ have the same meaning as the two columns of $\mathbf{P}$ and $\mathbf{Q}$, respectively, whereas $P^x_{i3} = \mathrm{d}p_i/\mathrm{d}\tau$ and $Q^x_{i3} = \mathrm{d}x_i/\mathrm{d}\tau$.

The solution of equations D.5 and D.6 for the plane-wave initial conditions ($\mathbf{Q} = \mathbf{I}$, $\mathbf{P} = 0$; $\mathbf{I}$ is the identity matrix) is denoted by $\mathbf{Q}_1$ and $\mathbf{P}_1$, and for point-source initial conditions ($\mathbf{Q} = 0$, $\mathbf{P} = \mathbf{I}$) by $\mathbf{Q}_2$ and $\mathbf{P}_2$.

It is convenient to introduce the real-valued matrix $\mathbf{M}$ of the second-order traveltime derivatives:

$$\mathbf{M} = \mathbf{P}\,\mathbf{Q}^{-1}. \tag{D.12}$$

As discussed in the main text (equation 5.7), the matrix $\mathbf{M}$ is used for computing the paraxial traveltime. For the point-source initial conditions,

$$\mathbf{M} = \mathbf{P}_2\,\mathbf{Q}_2^{-1}. \tag{D.13}$$

A Gaussian beam can be constructed using the solution of equations D.5 and D.6 with complex-valued initial conditions (Bleistein, 2008):

$$\mathbf{Q} = \frac{l\,\omega^2}{c_0}\,\mathbf{I}, \quad \tilde{\mathbf{P}} = \frac{i}{c_0}\,\mathbf{I}, \tag{D.14}$$

where l is the initial value of the beam width, ω is the angular frequency, and c_0 is the phase velocity at the source location corresponding to the take-off phase angle. The matrix $\mathbf{M}$ becomes complex-valued:

$$\tilde{\mathbf{M}} = [\mathbf{P}_1 + \tilde{\mathbf{M}}_0\,\mathbf{P}_2]\,[\mathbf{Q}_1 + \tilde{\mathbf{M}}_0\,\mathbf{Q}_2]^{-1}. \tag{D.15}$$

The initial value of $\tilde{\mathbf{M}}$ is

$$\tilde{\mathbf{M}}^0 = \frac{i}{l\,\omega^2}\,\mathbf{I}. \tag{D.16}$$

The matrix $\tilde{\mathbf{M}}$ is used to construct the paraxial traveltime (equation 5.7). Because $\tilde{\mathbf{M}}$ is complex-valued, the traveltime is complex-valued as well, which leads to amplitude decay away from the central ray.

APPENDIX E

ASYMPTOTIC WEIGHTING FUNCTION Φ FOR 2.5D ANISOTROPIC MEDIA

In this section, we derive the weighting function $\Phi(\theta_0)$ for the summation of Gaussian beams. We assume that that the medium properties do not vary in the x_2-direction, and the $[x_1,\, x_3]$-plane is a plane of symmetry, i.e., we treat the wave propagation in 2.5D. The analysis presented here is similar to that for isotropic media in Bleistein (2008).

Following Bleistein (2008), we consider equation 5.5 for a homogeneous anisotropic medium characterized by the medium properties at the source location $\mathbf{x}^s$. Substituting equation 5.6 into equation 5.5 (see the main text) for the summation of Gaussian beams yields:

$$G_{ik}(\mathbf{x}', \mathbf{x}^s, \omega) = \Phi(\theta_0) \int g_i(\mathbf{x}'')\, g_k(\mathbf{x}'')\, \frac{1}{4\pi c(\mathbf{x}^s)}\, \frac{1}{\sqrt{\det \tilde{\mathbf{W}}(\mathbf{x}'', \mathbf{x}^s)}}\, e^{-i\,\omega\, \tilde{T}(\mathbf{x}'', \mathbf{x}^s)}\, \mathrm{d}\gamma\,. \quad \text{(E.1)}$$

The parameter γ represents the take-off phase angle measured with respect to the central ray $R(\theta_0)$, and the range of integration is chosen to be symmetric over θ_0 (Figure 5.3). The ray corresponding to the phase angle $\gamma + \theta_0$ includes $\mathbf{x}''$, the point closest to $\mathbf{x}'$. The traveltime $\tilde{T}(\mathbf{x}'',\, \mathbf{x}^s)$ is given by:

$$\tilde{T}(\mathbf{x}'',\, \mathbf{x}^s) = (\mathbf{x}' - \mathbf{x}^s)^T\, \mathbf{p}[R(\theta_0 + \gamma)] + \frac{1}{2}(\mathbf{x}' - \mathbf{x}'')^T\, \tilde{\mathbf{M}}^x\, (\mathbf{x}' - \mathbf{x}''). \quad \text{(E.2)}$$

In the high-frequency approximation, the integral in equation E.1 can be evaluated using the method of steepest descent. Applying the saddle-point condition to the phase function $\psi = \tilde{T}(\mathbf{x}'',\, \mathbf{x}^s)$ leads to:

$$\frac{\partial \psi}{\partial \gamma} = \frac{\partial \tilde{T}(\mathbf{x}'',\, \mathbf{x}^s)}{\partial \gamma} = 0. \quad \text{(E.3)}$$

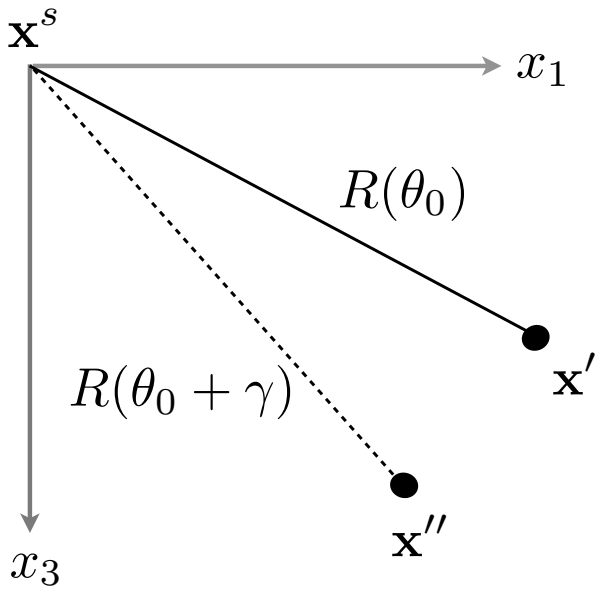

Figure E.1. Diagram illustrating the computation of the asymptotic weighting function $\Phi(\theta_0)$. The source exciting the Green's function is at point $\mathbf{x}^s$ and the receiver location is $\mathbf{x}'$. The ray $R(\theta_0)$ defined by the take-off phase angle θ_0 (generally different from the ray angle) with respect to the horizontal axis illuminates $\mathbf{x}'$. The closest point to $\mathbf{x}'$ on the ray $R(\gamma + \theta_0)$ is denoted by $\mathbf{x}''$.

Substituting equation E.2 into E.3, we find

$$\frac{\partial \tilde{T}(\mathbf{x}'', \mathbf{x}^s)}{\partial \gamma} = (\mathbf{x}' - \mathbf{x}^s)^T \left[\frac{\partial \mathbf{p}[R(\theta_0 + \gamma)]}{\partial \gamma}\right] + \frac{1}{2}(\mathbf{x}' - \mathbf{x}'')^T \left[\frac{\partial \tilde{\mathbf{M}}^x}{\partial \gamma}\right] (\mathbf{x}' - \mathbf{x}'')^T - \left[\frac{\partial \mathbf{x}''}{\partial \gamma}\right]^T \tilde{\mathbf{M}}^x (\mathbf{x}' - \mathbf{x}''). \tag{E.4}$$

Using equations D.10 and D.11, equation E.4 can be rewritten as

$$\begin{aligned}\frac{\partial \tilde{T}(\mathbf{x}'', \mathbf{x}^s)}{\partial \gamma} = &(x_i' - x_i^s)\, P_{i1}^x[R(\theta_0 + \gamma)]\, |\mathbf{p}[R(\theta_0 + \gamma)]| \\ &+ \frac{1}{2}(x_i' - x_i'')^T \left[\frac{\partial \tilde{M}_{ij}^x}{\partial \gamma}\right] (x_j' - x_j'')^T \\ &- |\mathbf{x}' - \mathbf{x}''|\, Q_{i1}^x[R(\theta_0 + \gamma)]\, \tilde{M}_{ij}^x\, (x_j' - x_j''),\end{aligned} \tag{E.5}$$

Since the vectors formed by the first columns of $\mathbf{P}^x$ and $\mathbf{Q}^x$ are perpendicular to the slowness surface and the wavefront, respectively, the saddle-point condition is satisfied for $\mathbf{x}'' = \mathbf{x}''$, i.e., for $\gamma = 0$.

Next, it is necessary to evaluate the second derivative of the phase function ψ at the saddle point:

$$\begin{aligned}\frac{\partial^2 \psi}{\partial \gamma^2}\Big|_{\gamma=0} = \frac{\partial^2 \tilde{T}(\mathbf{x}'', \mathbf{x}^s)}{\partial \gamma^2}\Big|_{\gamma=0} = &(x_i' - x_i^s) \left[\frac{\partial P_{i1}^x[R(\theta_0 + \gamma)]}{\partial \gamma}\right]_{\gamma=0} |\mathbf{p}[R(\theta_0)]| \\ &+ |\mathbf{x}' - \mathbf{x}''|^2\, Q_{i1}^x[R(\theta_0)] \left[\frac{\partial \tilde{M}_{ij}^x}{\partial \gamma}\right]_{\gamma=0} Q_{j1}^x[R(\theta_0)].\end{aligned} \tag{E.6}$$

Note that the matrices $\mathbf{P}^x$ and $\mathbf{Q}^x$ in equation E.6 are computed for the point-source initial conditions. The steepest-descent direction with respect to the real axis is defined by $1/2 \arg\left(\partial^2 \psi / \partial \gamma^2\right)|_{\gamma=0}$.

Equation E.1 reduces to:

$$G_{ik}(\mathbf{x}', \mathbf{x}^s, \omega) = \sqrt{\frac{2\pi}{\omega}}\, \Phi(\theta_0)\, g_i(\mathbf{x}')\, g_k(\mathbf{x}')\, \frac{1}{4\pi c(\mathbf{x}^s)}\, \frac{1}{\sqrt{\det \tilde{\mathbf{W}}(\mathbf{x}', \mathbf{x}^s)}} \times \frac{1}{\sqrt{\partial^2\psi/\partial\gamma^2|_{\gamma=0}}}\, \exp\Big(-i\omega \tilde{T}(\mathbf{x}',\, \mathbf{x}^s)\Big). \tag{E.7}$$

The weighting function $\Phi(\theta_0)$ can be found by substituting the ray-theoretical expression for $\mathbf{G}(\mathbf{x}', \mathbf{x}^s, \omega)$ into equation E.7. The ray-theoretical Green's function in homogeneous anisotropic media is given by (Červený, 2001):

$$\mathbf{G}(\mathbf{x}', \mathbf{x}^s, \omega) = g_i(\mathbf{x}')\, g_k(\mathbf{x}')\, \frac{1}{4\pi c(\mathbf{x}^s)\, \sqrt{\det\left[\mathbf{Q}_2(\mathbf{x}', \mathbf{x}^s)\right]}}\, \exp\Big(-i\,\omega\, \tilde{T}(\mathbf{x}',\, \mathbf{x}^s)\Big). \tag{E.8}$$

Combining equations E.7 and E.8 allows us to obtain the weighting function:

$$\Phi(\theta_0) = \sqrt{\frac{\omega}{2\pi}}\, \sqrt{\frac{\det[\tilde{\mathbf{W}}(\mathbf{x}', \mathbf{x}^s)]}{\det\left[\mathbf{Q}_2(\mathbf{x}', \mathbf{x}^s)\right]}\, \frac{\partial^2\psi}{\partial\gamma^2}\Big|_{\gamma=0}}. \tag{E.9}$$